Energie & Umwelt
Energy & Environment

320

Atmospheric Mixing in a Lagrangian Framework

Mengchu Tao

Member of the Helmholtz Association

Atmospheric Mixing in a Lagrangian Framework

Mengchu Tao

water vapor anormaly and diabatic heating rate anormaly at 400 K (10°S – 10°N)

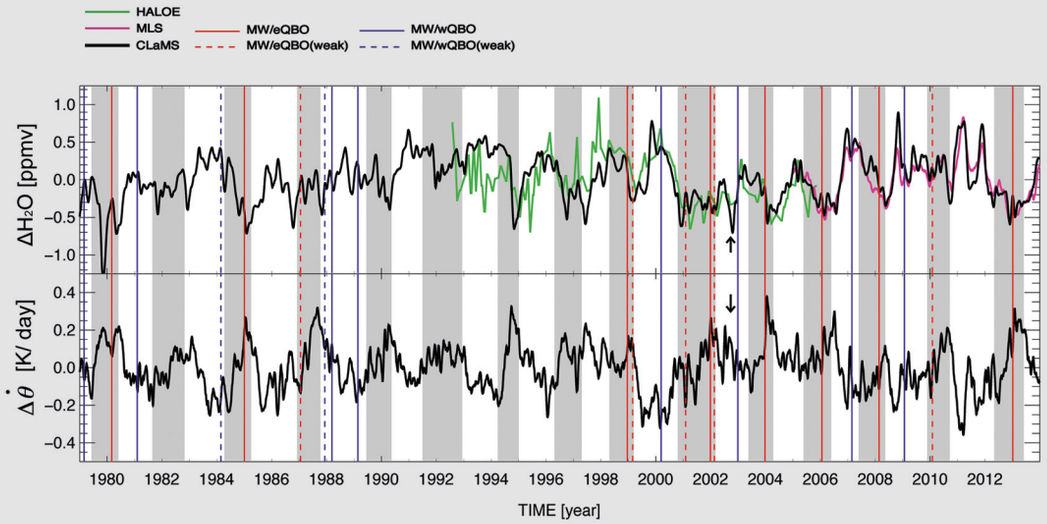

Energie & Umwelt /
Energy & Environment
Band / Volume 320
ISBN 978-3-95806-142-2

JÜLICH
FORSCHUNGSZENTRUM

Energie & Umwelt /
Energy & Environment
Band / Volume 320
ISBN 978-3-95806-142-2

JÜLICH
FORSCHUNGSZENTRUM

Schriften des Forschungszentrums Jülich
Reihe Energie & Umwelt / Energy & Environment Band / Volume 320

Die Dissertation kann wie folgt zitiert werden:

urn:nbn:de:hbz:468-20160711-114938-3
[http://nbn-resolving.de/urn/resolver.pl?urn=urn%3Anbn%3Ade%3Ahbz%3A468-20160711-114938-3]

Forschungszentrum Jülich GmbH
Institute of Energy and Climate Research
Stratosphere (IEK-7)

Atmospheric Mixing in a Lagrangian Framework

Mengchu Tao

Schriften des Forschungszentrums Jülich
Reihe Energie & Umwelt / Energy & Environment Band / Volume 320

ISSN 1866-1793 ISBN 978-3-95806-142-2

Bibliographic information published by the Deutsche Nationalbibliothek.
The Deutsche Nationalbibliothek lists this publication in the Deutsche
Nationalbibliografie; detailed bibliographic data are available in the
Internet at http://dnb.d-nb.de.

Publisher and Distributor: Forschungszentrum Jülich GmbH
Zentralbibliothek
52425 Jülich
Tel: +49 2461 61-5368
Fax: +49 2461 61-6103
Email: zb-publikation@fz-juelich.de
www.fz-juelich.de/zb

Cover Design: Grafische Medien, Forschungszentrum Jülich GmbH

Printer: Grafische Medien, Forschungszentrum Jülich GmbH

Schriften des Forschungszentrums Jülich
Reihe Energie & Umwelt / Energy & Environment, Band / Volume 320

D 468 (Diss., Wuppertal, Univ., 2016)

ISSN 1866-1793
ISBN 978-3-95806-142-2

The complete volume is freely available on the Internet on the Jülicher Open Access Server (JuSER)
at www.fz-juelich.de/zb/openaccess.

ABSTRACT

Inaccurate representation of mixing in chemistry transport models strongly influence the time evolution of all relevant trace gases and, in particular, the qualitative determination of the stratosphere-troposphere exchange (STE). For this reason, a physics-based numerical representation of mixing is required but remains an uncertain piece for the atmospheric transport models. However, the Lagrangian view of transport offers an alternative to exploit the numerical diffusion for parametrization of the physical mixing rather than to find ways of avoiding this effect.

Using the standard version of the Chemical Lagrangian Model of the Stratosphere (CLaMS) with mixing parametrization triggered by strong flow deformations, a remarkable Sudden Stratospheric Warming (SSW) case is investigated to reexamine transport, especially mixing, through analyzing the variation of stratospheric composition and of the tracer-tracer correlations. The case study of SSW demonstrates the intensified sub-seasonal variability of polar descent and tropical upwelling, which further motivates the study of the long-term impact of SSWs on the variability of the water vapor in the tropical lower stratosphere based on a CLaMS 35-year run. A sub-seasonal SSW-associated dehydration effect in the tropical lower stratosphere modulated by the two quasi-biennial oscillation (QBO) phases is found. The cooling and drying at the tropical tropopause, as a result of enhanced breaking of planetary waves in the subtropics during SSWs, is more intensive in the easterly QBO phase than in the westerly QBO phase. The extra-dehydration due to SSWs as well as the decadal variations of SSW frequency has potentially contributed to the long-term variability of water vapor

in the lower stratosphere.

Although the current transport scheme in CLaMS shows good ability of representing transport of tracers in the stably stratified stratosphere, it shows insufficient representation of fast convective uplift and mixing due to weak vertical stability in the troposphere. The CLaMS transport scheme was improved by including the effects of vertical instability and the related convection using the moist Brunt-Väisälä Frequency parametrizing the new tropospheric mixing. The revised CLaMS one-year simulation show a reasonable representation of convective patterns in the middle and upper troposphere. The extension of the mixing scheme increases the tropospheric influence in the middle and upper troposphere and at the same time enhances the STE in the UTLS region.

Contents

1 Introduction **1**
- 1.1 Atmospheric mixing 1
- 1.2 Scales of atmospheric mixing 4
- 1.3 Lagrangian realization of transport 8
- 1.4 Numerical diffusion and CLaMS 12
- 1.5 Objectives of the study 19

2 Simulation of transport and mixing during SSWs **21**
- 2.1 Stratospheric dynamics 21
- 2.2 Tracer- tracer correlation 24
- 2.3 A case study: 2009 major sudden stratospheric warming 29
- 2.4 Remarks 51

3 Response of water vapor in the tropical lower stratosphere to SSWs **53**
- 3.1 Water vapor in the lower stratosphere 53
- 3.2 CLaMS tropical water vapor in the lower stratosphere 56
- 3.3 SSW effect 63
- 3.4 Potential contribution of SSWs to water vapor trend 70
- 3.5 Discussion and remarks 72

4 Improvement of mixing parameterization **75**
- 4.1 Motivation 75
- 4.2 Parameter for vertical stability – moist Brunt-Väisälä frequency 82
- 4.3 Extension of transport scheme 92
- 4.4 Results 101
- 4.5 Summary and remarks 110

5 Summary and outlook **113**
5.1 Summary 113
5.2 Future work 115

A Appendix **117**
A.1 MLS averaging kernels 117
A.2 Monte Carlo difference test in composite analysis 118
A.3 CLAUS dataset 122
A.4 In-situ measurements 125
A.5 Equivalent potential temperature 126

Chapter 1

Introduction

1.1 Atmospheric mixing

What is mixing? It is difficult to give a straightforward definition. However, we experience mixing everyday. When spraying perfume in a corner, the fragrance can be smelt everywhere in the room a few minutes later. When dropping milk and a sugar cube into coffee and stirring with a spoon, a cup of sweet milk-coffee is prepared. We find: mixing begins with inhomogeneity and leads to homogenization and secondly; mixing is irreversible. These features associate mixing with diffusion, a net movement from a region of high concentration to a region of low concentration. Diffusion is accomplished through a series of unpredicted random motion. The random nature determines the irreversibility of diffusion.

Diffusion is usually expressed as an amount of diffusing substance through unit area within unit time, e.g. mass flux (in kg/ ($m^2 \cdot$ s)) or particle number density flux (in 1/($m^2 \cdot$ s)). A simple one-dimensional description of diffusion flux density was proposed by *Fick* (1855) and is known as the first Fick's law:

$$j_{\text{diff}} = -D\frac{\partial c}{\partial x}, \tag{1.1}$$

where c denotes the concentration, of which the dimension is amount of substance per unit volume. Note that when the amount of substance is quantified in molecule number, mass or mol, the concentration c is expressed in the unit of $1/m^3$, kg/m^3 or mol/m^3, respectively. This law relates the diffusion flux density

(j_{diff}) to the concentration gradient ($\partial_x c$) and diffusion coefficient or diffusivity D (in m^2/s). Equation 1.1 states that diffusion flux density j_{diff} is proportional to the concentration gradient $\partial_x c$. And we can easily generalize Eq. 1.1 to three-dimensions:

$$\mathbf{j_{diff}} = -\mathbf{D} \cdot \nabla c. \tag{1.2}$$

Note that both the diffusion flux density and concentration gradient are three-dimensional vectors. And consequently, the diffusion coefficient **D** is a tensor that is given as a 3×3 symmetric matrix **D** (*Onsager*, 1931).

In absence of advection and turbulence, mixing due to molecular diffusion is very slow. For example, the molecular diffusion coefficient D is of the order of 1×10^{-9} m^2 /s (sugar diffusing into water). Using the relation of diffusion coefficient D, time t and diffusion distance l as $t \approx (l^2/D)$, we can estimate the time for sugar being completely mixed with a cup of coffee (the depth of the cup $\approx$5 cm) through ideally passive molecular diffusion is more than 20 days. However, mixing in reality is mostly accompanied by flow motion itself, like the stirring of a spoon, largely accelerating the mixing.

The Earth's atmosphere has high Reynolds number ($Re = UL/\nu$, where U and L are typical velocity and spatial scales of the flow, respectively, and ν is the viscosity). Thus, the atmosphere is a fluid full of multi-scale eddies. This indicates that diffusion in the atmosphere is always related to and interacting with complex flow motions. Both the motion of the flow itself and diffusion contribute to the transport. Commonly, transport due to the motion of the flow is called advective transport, which represents the reversible part of transport. In contrast, mixing (diffusive transport) stands for the irreversible part of the transport [1]. The advective and diffusive part of transport can be related to each other through the continuity equation.

We consider a chemical passive tracer in an air parcel with number density n (in $1/m^3$) and molar mixing ratios μ (dimensionless). Noting that $n = N\mu$, where N denotes the total number density of all molecules. The continuity equation for the tracer can be written as:

$$\partial_t n + \nabla \cdot (\mathbf{j}) = 0 \tag{1.3}$$

where **j** denotes the flux density of the tracer.

[1] We will give a more precise definition of irreversibility in section 1.3

By using the Reynolds averaging procedure (see e.g. *Batchelor* (1953)):

$$\mathbf{u} = \bar{\mathbf{u}} + \mathbf{u}' \tag{1.4}$$

with $\mathbf{u} = (u, v, w)$ denoting the flow velocity, $\bar{\mathbf{u}}$ describing the mean (or resolved) wind velocity vector and with $\mathbf{u}'$ representing fluctuations (or unresolved), the flux density $\mathbf{j}$ of the tracer is given as:

$$\mathbf{j} = n\mathbf{u} = \mathbf{j_{adv}} + \mathbf{j_{diff}} = n\bar{\mathbf{u}} + n\mathbf{u}'. \tag{1.5}$$

Here, $\mathbf{j_{adv}}$(or $n\bar{\mathbf{u}}$) and $\mathbf{j_{diff}}$ (or $n\mathbf{u}'$) express the advective flux and mixing (diffusive) flux density, respectively. Recalling the one-dimensional Fick's law (*Fick*, 1855; *Hall and Plumb*, 1994) (eq. 1.2) and expressing the concentration c by number density n (in 1/m^3), $\mathbf{j_{diff}}$ can be substituted as:

$$n\mathbf{u}' = \mathbf{D} \cdot \nabla n = N\mathbf{D} \cdot \nabla \mu \tag{1.6}$$

Consequently, the continuity equation (1.3) can be transformed to:

$$\partial_t n + \nabla \cdot (n\bar{\mathbf{u}}) + \nabla \cdot (N\mathbf{D} \cdot \nabla \mu) = 0. \tag{1.7}$$

Hereby, the three parts, the internal change $\partial_t n$, advective transport $\nabla \cdot (n\bar{\mathbf{u}})$ and diffusive transport $\nabla \cdot (N\mathbf{D} \cdot \nabla \mu)$, balance each other in the continuity equation. In particular, when replacing n with N and knowing the total mixing ratios of all components must be one, the transport of all molecules is described by:

$$\partial_t N + \nabla \cdot (N\bar{\mathbf{u}}) = 0. \tag{1.8}$$

This indicates that the transport of total mass is determined only by advection while the transport of a specific tracer is driven by advection as well as diffusion. In other words, the advective transport changes the tracer distribution through importing or exporting the total mass, which can be understood as the reversible part of transport. In contrast, the diffusive transport (mixing) influences the tracer distribution through the internal exchange driven by unresolved fluctuations. Hereby, this part of transport occurs irreversibly.

Name	Spatial distance	Life span	Example
Planetary scale	>20000km	weeks to seasons	Planetary waves
Synoptic scale	>2000km	days to weeks	Cyclones
Mesoscale	2km-2000km	minutes to hours	Thunderstorm
Microscale	2mm-2km	seconds to minutes	Eddies and turbulences
Molecular scale	air molecules	less than a second	molecular diffusion

Table 1.1: Scales of atmospheric motion

1.2 Scales of atmospheric mixing

As we described in the last section: mixing begins with inhomogeneity and leads to homogenization. The criterion of homogeneity (or inhomogeneity) is based upon the finest structure that is concerned, resolvable or observable. Atmospheric mixing is driven by the turbulent part of the flow. The turbulent part of the flow can also be represented by the unresolved advective contributions (e.g. stirring in a non-linear flow). Therefore, what is considered as mixing, to a great extent, depends on the definition of the resolved and unresolved scales.

Atmospheric science spans a wide range of spatial scales (listed in Table 1.1) from planetary scale down to molecular scale. The finest structure that we are able to measure, perhaps not accurately, in the atmosphere is the molecular scale. Real physical atmospheric mixing happens on the molecular scale via molecular diffusion. On the other hand, mixing at the molecular scale is driven by micro-scale turbulence and eddies. Similarly, these micro-scale turbulences and eddies are controlled by processes on even larger scales. The interaction among eddies on different scales was nicely described in a poem by Richardson[2]. This eddy-eddy interactions are bonded through turbulence kinetic energy (TKE) that transfers from larger eddies to smaller eddies and finally dissipates, which is called turbulent energy cascade. Figure 1.1 shows a TKE spectrum as a function of wave-number. Following the turbulent energy cascade theory, we can further understand the irreversibility of mixing: the flow of energy is in one direction and dissipates through viscosity on the finest scale that is not reversible.

In the atmosphere, large-scale dynamical and thermal processes supply the energy for small-scale turbulences, which are expected to drive non-linear beha-

[2] 'Big whirls have little whirls / Which feed on their velocity, / And little whirls have lesser whirls / And so on to viscosity.'

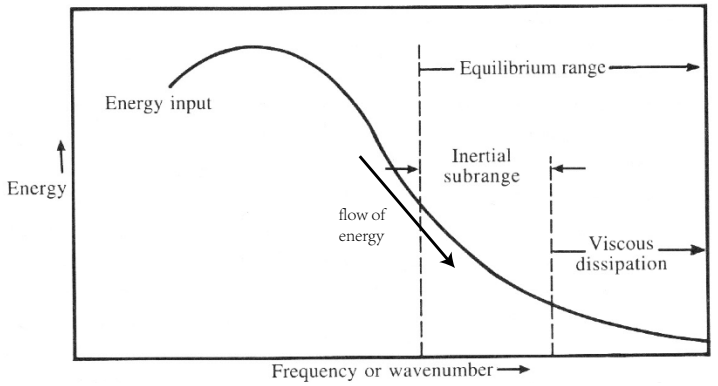

Figure 1.1: A Turbulence Kinetic Energy (TKE) spectrum illustrates the turbulent energy cascade: the energy from external forces excites the large eddies and is gradually passed to ever smaller eddies, all the way to a minimum scale where the energy is ultimately dissipated by molecular viscosity. The figure was adapted from *Stull* (1988).

vior on smaller scales. That means, some phenomenons in the atmosphere triggering turbulences play the role of 'mixer', or recalling the example of stirring milk into coffee, as a spoon. In the following, we discuss three phenomenona which are mainly associated with atmospheric mixing: interaction between the atmosphere and the Earth's surface, wind shear and convection caused by heating on the surface.

- Interaction between the atmosphere and the Earth's surface:
  The planetary boundary layer (PBL) is characterized by the complex interaction between the Earth's surface and the atmosphere. The depth of PBL is determined by heating of the surface and ranges from 1 km to 4 km. Within the PBL, the atmosphere directly responds to the Earth's surface through mechanical processes such as friction drag as well as thermal processes e.g. solar radiation and long-wave radiation from the surface. Both mechanical and thermal processes produce turbulence and various-sized eddies. As a result, the mixing driven by small-scale turbulence and eddies within the PBL is strong, efficient and fast. And the intensity and rapid turbulent mixing significantly influences the dispersion and dilution of pollution originating at the ground. The mixing within the PBL

is a complicated processes connecting a multitude of temporal and spatial scales. Here, we will not study the mixing in the PBL to avoid the difficulty of tracer sources and sinks in the PBL. To avoid this problem, all relevant tracers in this study are prescribed in the PBL by using climatologies based on observations.

- Wind shear:
  In general, wind shear includes the change of both wind speed and direction and exists both at horizontal and at vertical dimensions. In order to simplify the question how mixing is driven by a sheared flow, we consider a spherical Gaussian plume in a 2-D linear sheared flow with a shear rate s (*Konopka*, 1995). We refer to mixing when the plume becomes indistinguishable from the background atmosphere, which also can be understood as irreversibly losing its identity. The criterion of the dispersion significance is expressed as the ratio between major and minor axes of the plume and once this ratio exceeds a critical number, the plume dissipates. Here we interpret this ratio between major and minor axes of the plume as the aspect ratio $\alpha = \sigma_M/\sigma_m$: the major axis indicates the horizontal scale and the minor axis indicates the vertical scale of the atmospheric variabilities. As shown in Figure 1.2, in a sheared flow, the spherical Gaussian plume becomes elongated as well as rotated. The major and minor axes of the plume at first are identical and then the aspect ration grows with time like $\alpha = (st)^2$ (*Konopka*, 1995). Before the dissipation happens, we can see the plume still keeps its identity and is distinguishable from the background. Thus, this part of deformation is reversible, that is, as we introduced earlier, the advective transport. In contrast, once the dissipation happens, the plume loses its identity and merges into the background, an obviously irreversible process. This is what we defined as mixing or the diffusive part of transport.

  Although the mixing driven by 2-D sheared flow is a simplified picture, the atmospheric mixing is mainly driven by horizontal deformation when the flow is characterized by strong stratification. This is determined by the vertical thermal structure. In general, the troposphere is weakly stratified where convection frequently occurs whereas the stratospheric flow is highly statically stable. Consequently, the vertical mixing driven by convection is of importance in the troposphere while the mixing in the stratosphere is almost horizontal within a certain layer.

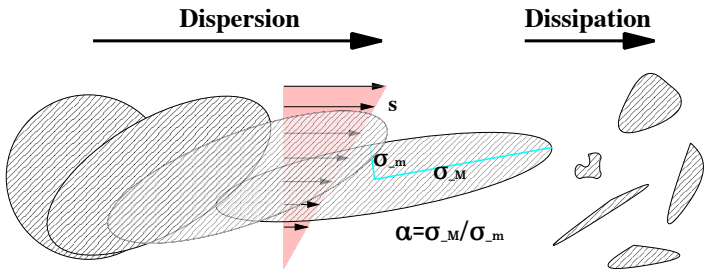

Figure 1.2: A simple example of mixing in 2-D sheared flow: dispersion and dissipation of a spherical Gaussian plume.

- Convection:
  Convection in the atmosphere is generated by density differences due to temperature gradients, e.g. when the lower parts of the atmosphere heat up, the atmosphere can become convectively unstable. Generally, convection occurs on a large range of scales. The convection we refer to is the moist convection mainly driven by the latent heat release. Moist convection contains intensive mass exchanges more vertically than horizontally, which embraces but is not limited to updraft, downdraft, chaotic advection and small-scale turbulence. Deep convection is an efficient process for fast transport of boundary layer air to the upper troposphere (e.g., *Gidel*, 1983; *Dickerson et al.*, 1987; *Pickering et al.*, 1988; *Danielsen*, 1993; *Houze et al.*, 2007). The vertical velocity in the convective updraft can reach 10 m/s that can lift up air parcels from the boundary layer up to the upper troposphere within several hours. Causing intensive vertical transport, convection also induces strong mixing that tries to homogenize or re-distribute tracers within certain convective regions. As a result, the vertical gradient of species can be strongly influenced by convective transport, mixing and chemistry of short-lived tracers.

Many studies have suggested that convection is an important process for tropospheric chemistry and stratosphere-troposphere exchange (STE) (e.g., *Gidel*, 1983; *Dickerson et al.*, 1987; *Gray*, 2003; *Hegglin et al.*, 2004). However, convection is a sub-grid process (typical horizontal scale range from several kilometers to tens of kilometers), which is currently one of the most uncertain part of all global atmosphere models. Its spatial and temporal scales are too small and too short so that these scales can not be explicitly resolved and can only be represented by different cumulus parametrizations (see *Arakawa* (2004) for a review). Different convection parametrizations introduce significant differences of vertical velocities, convective mass fluxes and result in uncertainties in climate predictions (e.g., *Rybka and Tost*, 2014) Besides the obvious disagreement among the datasets (e.g. NCEP reanalysis, ERA-interim reanalysis, TRMM satellite observations), serious inconsistencies exist between subgrid convection and the large-scale grid state in current reanalysis data set (e.g., *Newman et al.*, 2000; *Chan and Nigam*, 2009; *Wright and Fueglistaler*, 2013). Thus, it is extremely difficult to quantify in the models the mass exchange and mixing induced by convection. Chapter 4 will show a modification of the trajectory module and a new vertical mixing scheme, which aim to mimic the tracer transport induced by convection, implemented in CLaMS.

1.3 Lagrangian realization of transport

Many efforts have been made to find the best numerical solution of the continuity equation (1.7) that describes the atmospheric transport. As shown in Figure 1.3, Eulerian and Lagrangian perspectives are two different views to describe atmospheric transport. The Eulerian frame describes the changes of fluid from a perspective of fixed location (a grid). The Lagrangian perspective follows an individual fluid parcel (air parcel in the atmosphere) and records its composition. From the Lagrangian perspective, if every fluid parcel can be tracked and recorded, the whole state of the fluid can be perfectly described.

Differently from fixed grids defining the Eulerian framework, the Lagrangian view consists of grids moving with flow. In the following, we describe the moving and irregular Lagrangian grid as 'air parcels'. A Lagrangian air parcel refers to such an air mass small enough that its volume is negligible but at the same

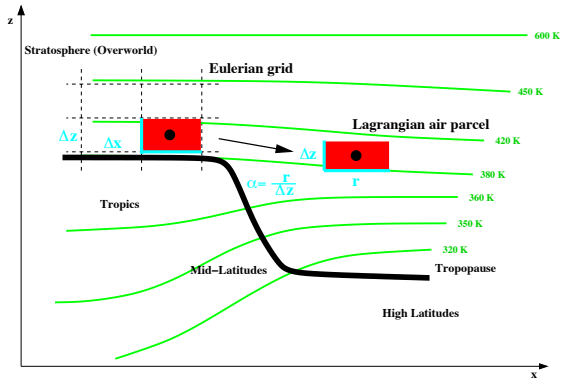

Figure 1.3: Eulerian grid fixed in space versus Lagrangian grid moving with the flow. The bold black points denote the air parcels which can be understood as small, pivotal points fixed either in space (Euler) or in the fluid (Lagrange). In both frames of reference, the horizontal and vertical resolutions Δx (or $r = \Delta r$ describing the 2D horizontal distance between the air parcels) and Δz should be consistently chosen. The plot is provided by Dr. P. Konopka.

time containing enough molecules to represent the properties of the atmosphere, such as temperature, density etc. In both frameworks, the properties of a certain grid point represent the mean properties of the atmosphere within the volume of the grid cell.

From a Lagrangian point of view, the air parcel follows the flow and thus $\bar{\mathbf{u}} = 0$ can be assumed. Consequently, the advection transport flux in the continuity equation (1.7) is zero. Then for a tracer in a Lagrangian air parcel, Eq.1.7 can be simplified as :

$$\partial_t n + \nabla \cdot (N\mathbf{D} \cdot \nabla \mu) = 0, \tag{1.9}$$

whereas the path of each air parcel, $\mathbf{r}(t)$, is the solution of the trajectory equation, i.e.

$$\frac{d\mathbf{r}(t)}{dt} = \mathbf{u}(\mathbf{r}(t),t), \quad \mathbf{r}(0) = \mathbf{r}_0 \tag{1.10}$$

with $\mathbf{u} = \bar{\mathbf{u}}$ being the prescribed (advective) velocity field. Eq. 1.9 describes the changes of composition within the air parcel which are only determined by the diffusive part of transport. When assuming no diffusion ($\mathbf{D} = \mathbf{0}$), the mixing

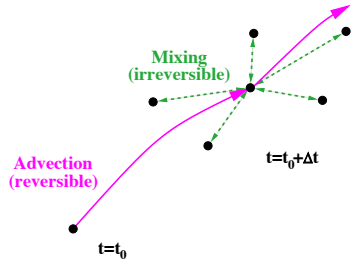

Figure 1.4: Lagrangian transport can be understood as a consecutive sequence of advection (trajectories driven by the wind) and mixing (mass exchange between adjacent air parcels). Whereas advection is reversible (i.e. a backward trajectory driven by the reversed velocity field exactly reproduces the starting point), mixing defines the irreversible part of transport (i.e. after mixing the original mixing ratios of the air parcel cannot be reproduced). Figure is provided by Dr. P. Konopka.

ratios are constant along the trajectory. Hereby, atmospheric transport can be directly divided into advection (Eq. 1.10) and mixing (Eq. 1.9) from the Lagrangian perspective. The advection and mixing is schematically shown in Figure 1.4. Advection, the reversible part of transport, can be described by the 3-D trajectory driven by the wind. Mixing, the irreversible part of transport, can be parameterized in terms of **D**. Therefore the Lagrangian view provides possibility of explicitly describing the physical mixing through parametrization.

In fact, the mixing in the atmosphere is extremely inhomogeneous both in time and space. Accordingly, **D** is a function of spatial variables x, y, z, and time variable t :

$$\mathbf{D} = D(x, y, z, t). \tag{1.11}$$

Recalling the assumption we make when deriving Eq. 1.6, the diffusion coefficient **D** is caused by fluctuations $\mathbf{u}'$. The orders of horizontal and vertical wind variabilities in the atmosphere are usually very different. Therefore, at a given time, the 3×3 diffusivity tensor **D** reduces to two horizontal and vertical diffusivities D_h and D_v by assuming that the atmosphere is invariant to horizontal rotations and by neglecting the still remaining two off-diagonal elements D_{xy}

(*Lyubarski*, 1960), i.e.

$$\mathbf{D} = \begin{pmatrix} D_h & D_{xy} & 0 \\ D_{xy} & D_h & 0 \\ 0 & 0 & D_v \end{pmatrix} \approx \begin{pmatrix} D_h & 0 & 0 \\ 0 & D_h & 0 \\ 0 & 0 & D_v \end{pmatrix} . \tag{1.12}$$

For simplicity, assuming that the horizontal space is isotropic (i.e. no direction is preferred), we replace the full 3d description (x, y, z) with a 2d space (x, z). Therefore, at a given time, the 3×3 diffusivity tensor $\mathbf{D}$ reduces to the horizontal and vertical diffusivities D_h and D_v given by:

$$\mathbf{D} \approx \begin{pmatrix} D_h & 0 \\ 0 & D_v \end{pmatrix} . \tag{1.13}$$

The aspect ratio refers to the ratio between the horizontal and vertical scales on which the atmospheric variabilities typically happen. *Haynes and Anglade* (1997) suggested the connection between the aspect ratio and the ratio between physical horizontal and vertical diffusion coefficient D_h and D_v as

$$\alpha^2 = D_h/D_v. \tag{1.14}$$

It was further pointed out by *Haynes and Anglade* (1997) that the aspect ratio in the lower stratosphere is about 250. Moreover, it was suggested by *Haynes and Anglade* (1997) that D_h is not an independent atmospheric parameter but a mean diffusive property that parametrizes transport occurring on unresolved scales, which can be derived from D_v and α. D_v is expected to be mostly independent on the vertical scales within the range $1 \sim 100$ m and is expected to be in the range 10^{-4} to 1 m^2/s (*Woodman and Rastogi*, 1984; *Balluch and Haynes*, 1997; *Waugh et al.*, 1997). The stratospheric value of D_v varies between 0.01 inside the polar vortex, 0.1 in the surf zone and around 0.5 m^2/s in the subtropics (*Legras et al.*, 2005; *Pisso and Legras*, 2008; *James and Legras*, 2009). Therefore, the horizontal diffusion coefficients D_h in the lower stratosphere are expected of the order of 10^3 m^2/s.

There are still many uncertainties related to atmospheric mixing. The accuracy of estimation of nonlinear chemical reactions depends on the degree (spatial and temporal resolution) that the ratios among atmospheric components can be resolved. In order to reconstruct high-resolved tracer distributions and variabilities, explicitly (or realistically) representing the fine structures (e.g. filaments)

and their dissipation (mixing) is crucial.

Many studies based on chemical transport models show that unrealistical representation of the dissipation will lead to either overestimating or underestimating the chemical reaction rates (*Edouard et al.*, 1996; *Searle et al.*, 1998a,b; *Tan et al.*, 1998). Besides the impact on the processes on the small scale, the mixing, as the irreversible part of transport, is found important to stratosphere-troposphere exchange (STE) (*Holton et al.*, 1995; *Konopka et al.*, 2007). As discussed in *Riese et al.* (2012), the uncertainties in the atmospheric mixing strength significantly influence the global distributions of the greenhouse gases H_2O, O_3, CH_4 and N_2O in the upper troposphere and lower stratosphere (UTLS) and the associated radiative effects. It is also shown that simulated radiative effects of H_2O and O_3, both characterized by steep gradients in the UTLS, are particularly sensitive to the atmospheric mixing strength.

In the following section, we will discuss how to realize a numerical representation of mixing in a physical way.

1.4 Numerical diffusion and CLaMS

Numerical diffusion can be understood as the the numerical error introduced by the re-gridding and associated interpolation. From both the Eulerian and Lagrangian point of view, numerical diffusion can be scaled by the grid width (Δx for horizontal grid width) and the integration time step (Δt) as:

$$D^{num} \approx \Delta x^2 / \Delta t. \tag{1.15}$$

Using this equation, the ratio between horizontal and vertical numerical diffusion coefficients can be estimated as:

$$D_h^{num} / D_v^{num} \sim \Delta x^2 / \Delta z^2 = \alpha^2. \tag{1.16}$$

According to the relation between aspect ratio and and physical horizontal and vertical diffusion coefficients suggested by *Haynes and Anglade* (1997) (Eq. 1.17), the ratio between horizontal and vertical numerical diffusion (D_h^{num}/D_v^{num}) is related to the ratio between horizontal and vertical physical diffusion ((D_h/D_v)) through the aspect ratio as

$$D_h^{num} / D_v^{num} \sim \alpha^2 = D_h / D_v. \tag{1.17}$$

In order to achieve a stable numerical solution, the maximum time step of integration Δt is limited by the Eulerian grid size Δx and the maximum flow velocity u_c through $\Delta t < \Delta x/u_c$, which is known as the Courant-Friedrichs-Lewy (CFL) condition (*Courant et al.*, 1928). This is a strong limitation of the available time step Δt. For a typical, maximum wind velocity of the order of $u_c \approx$ 100 m/s and a typical Eulerian grid size $\Delta x \approx 100$ km, a high frequency of the interpolations on the Eulerian background grid is required ($\Delta t < 16$ min). Consequently, the horizontal numerical diffusion is of the order of 10^6 m^2/s according to Eq. 1.15. Therefore, the physical horizontal diffusion is largely overestimated especially in a stably stratified flow like in the stratosphere where D_h is on the order of 10^3 m^2/s as discussed in the previous section.

In contrast to the overestimation of diffusion from the Eulerian point of view, the semi-Lagrangian approach offers an alternative numerical realization of transport. *Lin and Rood* (1996) argued that the maximum spatial gradient of the wind velocity $\partial_x u \approx \Delta u/\Delta x$ (in 1/s) rather than the maximum wind velocity itself u_c determines the time step of integration Δt through the condition $\Delta t < (\partial_x u)^{-1} \approx \Delta x/\Delta u$. The gradient of the wind velocity Δu are much smaller than the values of u_c (by a factor of 100 to 1000). Thus, the critical time step of integration becomes significantly larger than the corresponding Eulerian time step. Consequently, the numerical diffusion becomes comparable with the effective horizontal diffusivity.

However, full Lagrangian (or pure trajectory) methods usually cause increasingly inhomogeneous distributions of air parcels. Accordingly, some re-mapping (or re-gridding) procedures must be applied to solve the inhomogeneous distribution of air parcels in a pure trajectory model. The re-mapping procedures, at the same time, inevitably cause some numerical diffusion.

Although some numerical diffusion introduced by the re-mapping procedure in Lagrangian method is inevitable, it is possible to formulate a parametrization that is able to estimate physical mixing. To achieve this, two problems have to be solved. Firstly, an appropriate Lagrangian grid has to be defined. That means typical horizontal and vertical scales have to be chosen to mimic the physical diffusivities D_h and D_v according to Eq. 1.17. *Konopka et al.* (2012) describe an idea of defining a grid based on the spatial distribution of entropy and the static stability as shown in Figure 1.5. The theoretical reason behind this definition is that the vertical diffusivity in the atmosphere is largely associated with the static stability. The Brunt-Väisälä frequency N describes the frequency at which an

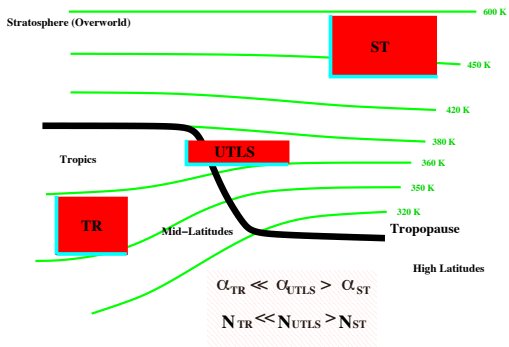

Figure 1.5: Static stability-based scales which uniformly cover the whole atmosphere. N and $\alpha = r/\Delta z$ denote the static stability and aspect ratio of three representative air parcels in the troposphere (TR), stratosphere (ST) and in the vicinity of the tropopause (UTLS), respectively. Figure is provided by Dr. P. Konopka.

air parcel oscillates when displaced vertically in a statically stable environment: large N indicates strong stability and small N means weak stability. It is shown in Fig. 1.5 that the air parcels in the UTLS with large N are characterized by large α. Thus, the small vertical grid scale confines the vertical motions and minimizes the vertical diffusivity. In contrast, the air parcels in the troposphere and upper stratosphere with small static stability N small are defined by small α. The larger scales of vertical resolution enhance the vertical diffusivity.

Secondly, an appropriate re-mapping (or re-gridding) procedure has to be found. The re-mapping procedure should be triggered by some flow parameters which describes the physical mixing. As we mentioned in section 1.3, a Lagrangian perspective of transport differs from the Eulerian one in that numerical diffusion can be completely avoided or be designed in a physical way. In other words, we can consider re-gridding procedure not only as a passive numerical solution to sustain the spatial homogeneity of air parcels but also as an active scheme to mimic the true physical atmospheric mixing. In the following, we will introduce the mixing scheme in CLaMS that mimics the true atmospheric

mixing through a re-gridding procedure.

1.4.1 Mixing scheme in CLaMS

Lagrangian transport offers a two-step procedure how to implement physical mixing into a transport scheme so that numerical diffusion mimics rather than disturbs the physical mixing. After defining an appropriate grid (discussed in the last section), the question arises which physical processes trigger mixing in the atmosphere and how such processes can be numerically implemented into the transport scheme using grid interpolations or, in other words, by using an appropriate re-gridding scheme.

Our heuristic idea for defining a mechanism triggering mixing events is to identify regions in the atmosphere which are "unstable" and which may undergo "strong deformations". The flow is called unstable if a small perturbation at initial time will grow significantly during the course of the evolution of the flow. From the Lagrangian perspective, this means that the distance between the adjacent air parcels increases "sufficiently fast". Thus, by monitoring this property in the Lagrangian grid it is possible to detect such regions in the flow and, subsequently, by re-gridding these parts of the grid, to trigger numerical diffusion through the related interpolations.

A further motivation is based on the gradient Richardson number, i.e. on a dimensionless critical ratio Ri_c describing the onset of instabilities driven by wind shear and/or buoyancy (*Turner*, 1973). Ri is defined as

$$Ri = \frac{N^2}{\left(\frac{\partial u}{\partial z}\right)^2 + \left(\frac{\partial v}{\partial z}\right)^2} \tag{1.18}$$

with u, v denoting the horizontal wind components and N the Brunt-Väisälä Frequency. Ri_c, is about 0.25 (although reported values have ranged from roughly 0.2 to 1.0) with the flow becoming dynamically unstable or even turbulent when $Ri < Ri_c$ (*Turner*, 1973). Such turbulence occurs either when the wind shear is large enough to outweigh any stabilizing buoyant forces (denominator is large), or when the dry or, more generally, moist environment is statically unstable (numerator is small or even negative).

In the Lagrangian realization of this concept, the local shear rates in the flow have to be replaced by the integral deformation which can be derived from the

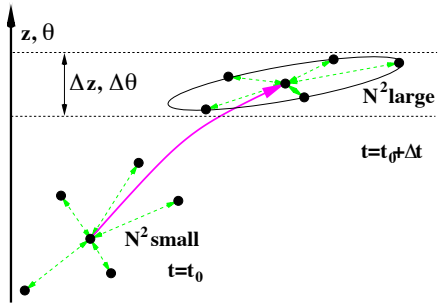

Figure 1.6: Mixing driven by the (wet) static stability. If $N^2 = (g/\theta_e)d\theta/dz$ (θ_e - equivalent potential temperature) is small or even negative - a state that may occur mainly in the troposphere - effective (vertical) mixing is expected. In the Lagrangian parametrization, the mixing ratios of the affected air parcel and its next neighbors are set to their average value. Such regions can be diagnosed from a sufficiently large change of the vertical separation between the next neighbors during the advection step and should correlate with vertically unstable or weakly stable regions (small values of N^2). The figure is provided by Dr. P. Konopka.

relative motion of the next neighbors occurring during the Lagrangian time step Δt (see below). In addition, in the troposphere, where the (wet) static stability N^2 can be small, the weakly stable or the unstable regions of the atmosphere can effectively drive vertical mixing (see Figure 1.6). In contrast, in the stratosphere, where the flow is characterized by high static stability, only sufficiently strong, almost horizontal deformations are expected to drive mixing within the considered stratospheric layer.

In the following, we show how the mixing scheme of the Chemical Lagrangian Model of the Stratosphere (CLaMS) implements the concept of deformation-induced mixing in a Lagrangian grid (*McKenna et al.*, 2002a; *Konopka et al.*, 2004, 2007) (see Figure 1.7).

Here, the critical deformation γ_c is defined as $\gamma_c = \Delta t \lambda_c$. λ_c denotes the 2D finite-time critical Lyapunov exponent describing a deformation of a sufficiently small circle with a radius r_0 into an ellipse with major and minor axes given by $r_\pm = \exp \pm \lambda_c \Delta t$ (more details in *McKenna et al.* (2002a)). At first, both the time step Δt and λ_c are free parameters.

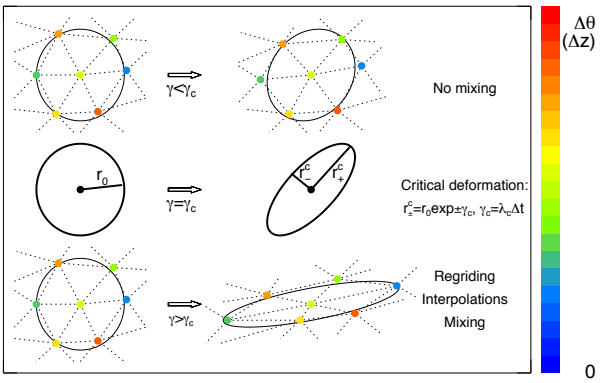

Figure 1.7: Mixing parameters in CLaMS (*Konopka et al.*, 2005). The CLaMS mixing algorithm is triggered if during the advection step Δt the relative positions between the next neighbors within a layer with thickness Δz (or $\Delta\theta$) change with a sufficiently high rate $\gamma > \gamma_c$. For $\gamma < \gamma_c$ mixing-free transport occurs along the trajectories.

In order to decide whether a deformation occurring in the real atmospheric flow surrounding a given air parcel exceeds γ_c, its next neighbors within a layer of thickness Δz (or $\Delta\theta$ as shown in Fig. 1.7) are calculated by means of the 2D Delaunay triangulation described in *McKenna et al.* (2002a). This is done before the advection step. Furthermore, let us assume that the mean distance of the considered air parcel to the next neighbor is given by the mean separation between the air parcels in the considered layer, i.e. by $r = r_0$. Then, during the advection step, both horizontal deformations (mainly strain) and vertical deformation within the almost horizontal layer (mainly shear) change the relative positions of the next neighbors.

After the advection step, the distances r to the next neighbors are compared with those before the advection step. If r is larger than r_- and smaller than r_+ (i.e. $\lambda < \lambda_c$), no re-gridding procedure is triggered (i.e. $\mathbf{D} = \mathbf{0}$). If r exceeds r_+, a new air parcel is introduced in between with the mixing ratio of the transported species linearly interpolated from the air parcels for which $r > r_+$ was diagnosed. In order to keep the mean separation between the air parcels per layer within certain bounds (here around r_0), renewed triangulation allows the distances to the

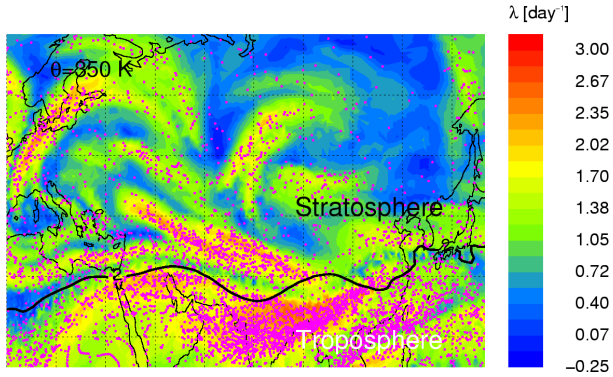

Figure 1.8: Realization of mixing in CLaMS (*Pan et al.*, 2006). The finite-time Lyapunov exponent λ describes the integral deformation at $\theta = 350$ K. Highest values of λ can be diagnosed in the vicinity of the jet separating the troposphere from the stratosphere (black line, PV=2). Mixing algorithm in CLaMS yields the highest mixing rates due to the largest number of interpolations carried out in the region with the highest values of λ (pink dots denote the new air parcels inserted into the scheme).

current next neighbors to be checked and the redundant air parcels are removed by means of the same linear interpolations (i.e. two air parcels are replaced by one in the middle). In CLaMS, the criterion $r < r_-$ is used for the redundant air parcels but variations of this condition are possible (*Wohltmann and Rex*, 2009). Note that the linear interpolations used for calculating the mixing ratios of new air parcels are essential, because, assuming similar volumes of the interacting air parcels, such interpolations mimic fully mixed states of the air parcels involved.

An example of this procedure is shown in Figure 1.8 where new air parcels inserted into the grid around $\theta = 350$ K are highlighted (pink dots). The finite-time Lyapunov exponent λ is color-coded, which is calculated from the deformation of 3D circles (i.e. distributed around each air parcel within the layer). Around PV=2 (black line) a strong jet over the Himalayas can be diagnosed forming a sharp isentropic transport barrier between the stratosphere and the troposphere. A clear correlation between λ and the number of new air parcels shows how deformation-induced mixing works in CLaMS (i.e. for a given advective time step Δt deformations with $\lambda > \lambda_c$ trigger the re-gridding procedure

parametrizing mixing between the air parcels). A strong inhomogeneity of Lagrangian mixing, both in time and space (in CLaMS less than 15% of air parcels per day are affected by mixing), is the most pronounced difference to the Eulerian approach where numerical diffusion is ubiquitous.

1.5 Objectives of the study

The general objective of the thesis is to reexamine the atmospheric mixing as implemented in CLaMS and to provide a possible extension of the current mixing scheme of CLaMS.

The general objective is achieved through the following three steps:

1) we start with an example of pronounced stratospheric mixing that commonly happens after sudden stratospheric warmings (SSWs). Especially, we investigate the mixing intensity in the CLaMS simulation in relation with wave propagation and breaking; how well mixing can be resolved in satellite observations; the impact of SSWs on the Brewer-Dobson circulation (BD circulation).

2) Motivated by the result of the previous section, we analyze the impact of SSWs on the variability of water vapor in the lower stratosphere. We further discuss the potential contribution of SSW-associated water vapor subseasonal variability to the trend of water vapor in the lower stratosphere.

3) Finally, we reexamine the mixing parametrization of CLaMS in the troposphere. Here, we propose an idea to extend the current mixing scheme in order to parametrize the mixing due to the weak stability mainly in the troposphere and to parameterize the strong vertical uplift from the boundary layer to the upper troposphere by deep convection. We compare one-year simulation result implemented the extended scheme with the referee CLaMS run.

Chapter 2

Simulation of transport and mixing during sudden stratospheric warmings

Sudden stratospheric warmings (SSWs) are among the most impressive dynamical event in the climate system (e.g., *Scherhag*, 1952; *Quiroz*, 1975; *Labitzke*, 1977). In the following, a case study for the SSW in 2008-2009 will be presented combining not only detailed CLaMS simulations but also satellite-based observations. This chapter is based on the results published by *Tao et al.* (2015a).

2.1 Stratospheric dynamics

The troposphere is characterized by rapid and significant vertical motion and mixing, associated with the vertical temperature structure. In contrast to the troposphere, the stratospheric temperature rises with altitude due to the ozone-layer absorption of ultraviolet radiation. As a result of the reversed temperature profile, the stratosphere is highly statically stable and thus the vertical mixing is inhibited (e.g., *Woodman and Rastogi*, 1984). The weak vertical mixing and strong horizontal flow give rise to the chaotic advection of chemical species (*Lorenz*, 1963). Consequently, mixing in the stratosphere is mainly driven by horizontal deformation and is reasonably confined within the considered layer. It is worth to remark that the vertical exchange and associated mixing cannot be neglected

in the troposphere, which is not adequately considered in the mixing algorithm in CLaMS so far. Possible extension of the transport and mixing scheme will be discussed in chapter 4.

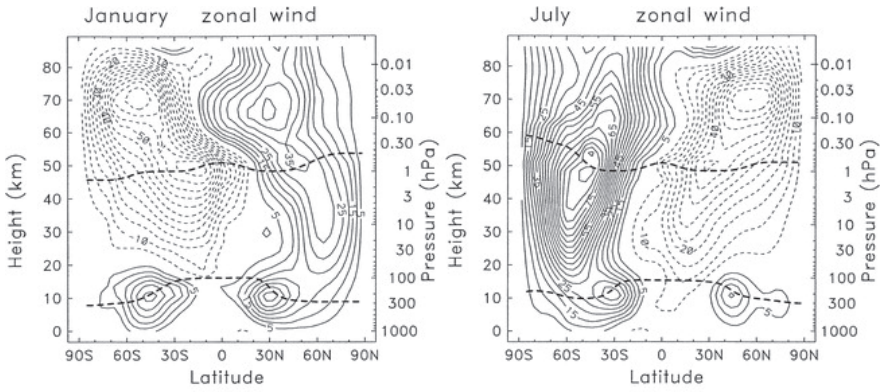

Figure 2.1: Climatological zonal mean zonal winds for (left) Jan and (right) Jul. Zonal winds are from the Unified Radio and Plasma Wave Experiment (URAP) dataset (contour interval 5 m s^{-}1, with zero contours omitted). The heavy dashed lines denote the tropopause taken from National Centers for Environmental Prediction (NCEP) and stratopause (defined by the local temperature maximum near 50 km) (*Randel et al.*, 2004a).

The January (left) and July (right) climatological zonal mean wind (based on the URAP dataset) fields are shown in Figure 2.1 (*Randel et al.*, 2004a). We can easily observe that the mean extratropical zonal flow in the stratosphere is easterly in the summer hemisphere and westerly in the winter hemisphere. However, a clear asymmetry of stratospheric zonal wind can be noticed comparing SH and NH during the same season. The asymmetry is especially significant during winter: extratropical westerlies are much stronger in the southern hemisphere (SH) than in the northern hemisphere (NH). It is because that the weaker westerlies in the boreal winter are a result of more planetary wave forcing generated in the orography-dominated NH (e.g., *Eliassen*, 1951; *Plumb and Bell*, 1982; *Rosenlof*, 1995). Meanwhile, weak westerlies in the boreal winter with the zonal wind velocity u being less than critical wind speed u_c, favors the upward propagation of planetary waves to stratosphere. However, the too strong westerlies ($u > u_c$) in the SH limit the propagation of planetary waves during the

boreal summer (e.g., *Charney and Drazin*, 1961; *Dickinson*, 1969) .

Planetary wave forcing can be diagnosed by the Eliassen-Palm (EP) flux and its divergence (e.g., *Eliassen*, 1951; *Plumb and Bell*, 1982). Figure 2.2 shows a general feature of EP flux divergence (colored) and upwelling due to diabatic heating (red contours) during summer (right) and winter (left). EP flux convergence (negative values in Fig. 2.2) indicates the breaking of waves and deceleration of westerly zonal mean flow (*Konopka et al.*, 2015). It is shown that the seasonality of wave forcing in the stratosphere is consistent with the zonal mean flow shown in Fig. 2.1: the maximum of EP flux convergence is found at extratropics of NH during boreal winter. The planetary wave breaking produces westward forcing of mean meridional flow. The westward forcing in the extratropical stratosphere drives the poleward heat flux, which cause the warming of high latitudes and cooling in the tropics. In consequence, the warming of high latitudes is followed by radiative cooling, which is accompanied by downwelling. And the cooling in the tropics is followed by radiative warming, which is accompanied by upwelling. Thus, the tropical upwelling, polar downwelling and the poleward transport complete a picture of the wave-driven meridional overturning circulation, so called the Brewer- Dobson circulation (shown as yellow arrows in Fig. 2.2). The Brewer- Dobson circulation (BD circulation) was firstly proposed by Dobson (*Dobson et al.*, 1929) and was then validated by observations (*Brewer*, 1949). The overturning BD circulation can be well explained by the seasonality of the wave forcing. Moreover, the stronger wave forcing in NH winter can well explain the stronger tropical upwelling in boreal winter (e.g., *Holton et al.*, 1995).

The most impressive dynamical events related to upward propagation of large-scale planetary wave into the stratosphere are sudden stratospheric warmings (SSWs). SSW events are good examples to validate the transport and mixing scheme of a model in a dynamical situation of strong wave activity. During and after SSWs, the exchange between air across the transport barriers, e.g. vortex edge, is expected to be intensified with some weakening of the mean flow. Thus, the permeability and isolation of the polar vortex can be investigated. Except for the dynamical diagnosis, a straightforward way for this study is to analyze the tracer distributions and variations with continuous comparisons with observations. Therefore, in the following part of this chapter, we will confine our attention to the SSW event period.

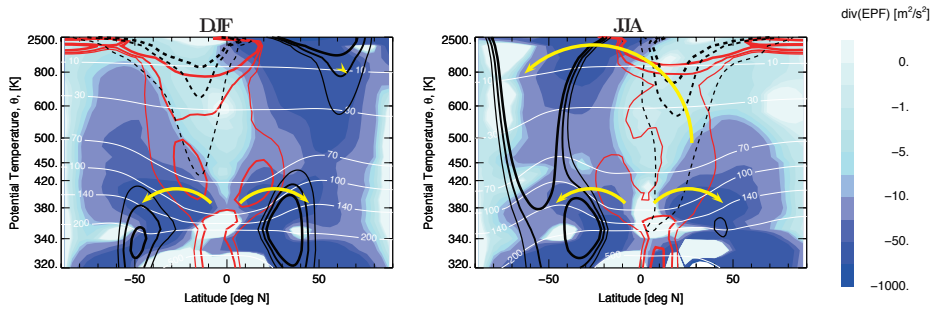

Figure 2.2: Divergence of the EP flux, as resolved by the ECMWF ERA-Interim winds, which drives the meridional, poleward component of the BD circulation (nonlinear color scale). Nonequidistant potential temperature θ is used as the vertical axis in order to magnify the UTLS region. The red isolines quantify upwelling due to diabatic heating Q^* with values 0.5, 1.0, and 2.0 K/day from thin to thick, respectively. White and black are the isobars and isotachs of the zonal wind, respectively (westerlies: 20, 25, and 30 m/s; easterlies: 10, 20, and 25 m/s from thin to thick). DJF (left) versus JJA (right) distribution. The thick yellow arrows schematically denote the shallow (around 400 K or between 100 and 70 hPa) and deep (around 1000 K or 10 hPa) branches of the BD circulation. The Figure is adapted from *Konopka et al.* (2015).

2.2 Tracer- tracer correlation

Before presenting a detailed analysis of the major SSW case study, here we introduce the tracer-tracer correlation technique that will be intensively used later. Tracer- tracer correlation is a useful diagnostic tool. Firstly, it can be easily and directly applied to observations, from e.g. satellites (*Müller et al.*, 1996; *Tilmes*, 2004), aircrafts (*Richard et al.*, 2001; *Ross et al.*, 2004) and balloons (*Müller et al.*, 2001; *Vogel et al.*, 2003). Furthermore, the correlations between two tracers enables a more robust analysis of chemical or dynamical changes of the atmosphere (*Müller et al.*, 1996; *Plumb et al.*, 2000; *Plumb*, 2007). Similarly to analyzing the variation of one single tracer, the tracer- tracer correlations are effected by both dynamical and chemical processes. Moreover, tracer- tracer relations of two long- lived tracers (e.g. CFC-11 and CFC-12) may be used to infer the ratio of the chemical life time of such tracers in the atmosphere from

observations (*Volk et al.*, 1997; *Hoffmann et al.*, 2014).

Chemical constituents in the stratosphere, where chemical sources and sinks are weak compared with dynamical timescales, are influenced by the Brewer-Dobson circulation and by quasi-isentropic mixing (which is most efficient within the extratopical surf zone in winter) and show compact tracer-tracer relations (*Plumb*, 2007). Mixing is suppressed at the edge of the winter polar vortex and at the edges of the tropics, so that tracer relationships distinct from those of middle latitudes occur in the tropics and in the polar vortices (e.g., *Plumb*, 1996; *Volk et al.*, 1996; *Müller et al.*, 1996, 2001; *Plumb*, 2007). Here, we focus on the relationship of O_3 with the long-lived tracer N_2O. Because chemical production and loss terms of O_3 increase strongly with altitude in the stratosphere, ozone can not be considered long-lived at altitudes above ≈ 20 km and relations with N_2O are not necessarily compact (*Hegglin and Shepherd*, 2007). Conditions are different in the polar vortex in winter, where the lifetime of ozone exceeds half a year in the absence of chlorine-catalyzed ozone loss in the lower stratospheric vortex (*Sankey and Shepherd*, 2003). However, the transport barriers in the stratosphere are sufficiently strong to allow distinct tracer-tracer relationships, in particular different O_3-N_2O relationships to develop in the polar vortex, the mid latitudes and in the tropics (*Michelsen et al.*, 1998; *Ray et al.*, 2002; *Müller et al.*, 2005; *Hegglin and Shepherd*, 2007).

2.2.1 Interpretation of $O_3 - N_2O$ correlation

Because different O_3-N_2O relationships prevail in the polar vortex, in mid-latitudes and in the tropics, mixing of air masses from these different regions will change O_3-N_2O relationships, even if relations in a particular region are linear (Fig. 2.3, top panel). Mixing between the polar vortex and mid-latitudes and between mid-latitudes and the tropics occurs along quasi-isentropic surfaces (*Proffitt et al.*, 1990; *Müller et al.*, 2005). Because the location of the isentropes in O_3-N_2O space, mixing of mid-latitude and polar air will lead to higher ozone and higher N_2O in the polar region and mixing of mid-latitude and tropical air will lead to lower N_2O and lower ozone in the tropics (Fig. 2.3, top panel). The effect of mixing between polar and mid-latitude air on O_3-N_2O relationships and the occurrences of this process along quasi-isentropic surfaces is also clearly visible in model simulations (*Sankey and Shepherd*, 2003; *Müller et al.*, 2005; *Lemmen et al.*, 2006). However, the strength of the transport barrier at the vortex edge is likely underestimated in model simulations (*Hoppe et al.*, 2014) so that

the intensity of mixing will be overestimated.

Upwelling and downwelling of stratospheric air changes tracer mixing ratios at a particular altitude (or potential temperature level) but does *not* change the tracer-tracer correlation (*Müller et al.*, 1996; *Ray et al.*, 2002). Therefore O_3-N_2O relationships will not be affected by up- and downwelling (Fig. 2.3, middle panel), while however the location of the potential temperature surfaces in O_3-N_2O space will change. Because of the vertical profile of ozone and N_2O below altitudes of ≈ 700 K, downwelling in the polar region will lead to an upward bending (more ozone, less N_2O) of the isentropes, while upwelling in the tropics will lead to downward bending (less ozone, more N_2O) of the isentropes (Fig. 2.3, middle panel, grey lines).

Finally, chemistry will impact O_3-N_2O relationships. Indeed, ozone-tracer relations have been used extensively to examine lower stratospheric ozone loss in the polar regions (e.g., *Proffitt et al.*, 1990; *Müller et al.*, 1996, 2001; *Tilmes et al.*, 2006). On the timescales and for the altitudes of interest here, only chemical changes for ozone needs to be taken into account. Thus, chemical loss of ozone in the polar regions shifts the O_3-N_2O relationship downward, towards lower ozone mixing ratios and chemical production of ozone in the tropics will shift the O_3-N_2O relationship upwards towards higher ozone mixing ratios (solid and dashed black lines in Fig. 2.3, bottom panel). In a model simulation the impact of chemistry on ozone-tracer relations can be investigated further through simulations using passive (i.e., chemically inert) ozone. This point will be discussed below in section 2.3.7.

2.2.2 Tracer space and physical space

The advantage of tracer-tracer correlations have been illustrated above. However, the main difficulty to interpret a tracer-tracer correlation lies in the translation between tracer space and physical space. Figure 2.4 shows schematically how these physical processes can be interpreted and separated by using N_2O–O_3 correlations. The left column in Fig. 2.4 show the APs in physical space using equivalent latitudes as the meridional axis. On the right side, the corresponding tracer space is shown in the same way as discussed in Fig. 2.3.

Through isentropic mixing, the APs in the mid latitudes change their composition as they mix with other APs isentropically transported from higher or lower latitudes (like fragments B, E and F in Fig. 2.4a1, b1). Consequently, mixing lines connecting the isolated correlations may appear or, when intensive and

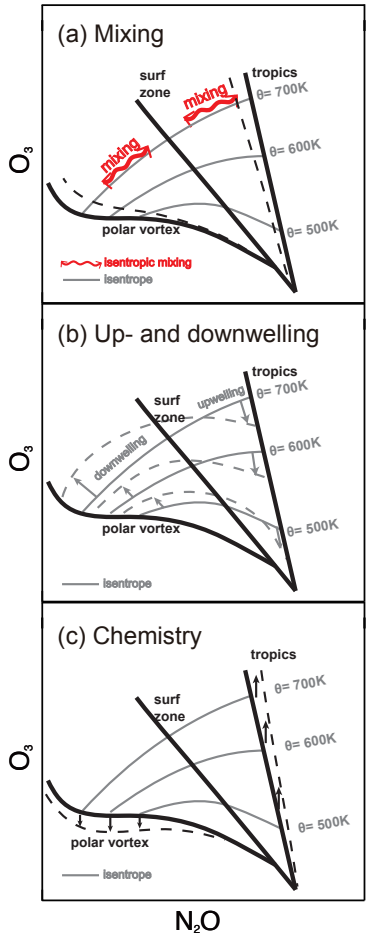

Figure 2.3: Schematic diagram showing the influence of (a) mixing, (b) up- and downwelling and (c) chemistry on N_2O-O_3 correlations.

persistent mixing happens, the whole correlation line inclines to one side (e.g. the thick black correlations in Fig. 2.4b2). Moreover, the enhanced mixing also results in a decay or growth of certain correlation branches (shown as thinned or thickened black curves in Fig. 2.4b2 and c2) and expressing the shrinking or expanding of corresponding regions.

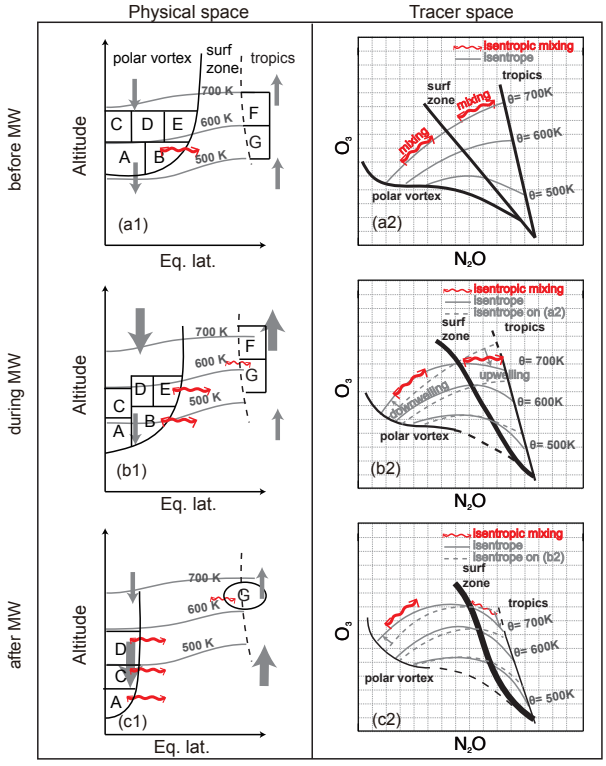

Figure 2.4: Schematic diagram of transport processes shown in physical space (left column) and tracer space (N_2O–O_3, right column) before (top), during (middle) and after (bottom) the major SSW. In the physical space (left column), equivalent latitudes are used as the horizontal coordinates to illustrate isentropic mixing (curved red arrows) and cross-isentropic transport (grey vertical arrows). The thickness of the grey arrows indicates the intensity of vertical motion. The characters denote exemplarily the vortex and tropical air masses which interact with the mid-latitude air. Black curves in (a2)–(c2) show respective N_2O–O_3 correlations. Grey lines denote the isentropic levels. In the tracer space, the position of isentropes before (dashed) and after (solid) the major SSW is also marked. The change of the position of a prescribed point in the tracer space along the isentropes quantifies isentropic mixing, whereas motion relative to these isentropes describes the effect of an idealized (mixing-free) cross-isentropic motion (up- or downwelling). Changes of the relative thickness of the different correlation branches mean their enhanced or weakened relative contributions to the composition of the considered part of the atmosphere (dashed lines indicate a possible missing part).

Conversely, if the APs are affected purely by vertical transport like strong cross-isentropic motion during the SSW (i.e. by up- or downwelling), the composition of the APs (and thus their position in tracer space) stays the same although their θ-coordinate significantly changes. As discussed in Fig. 2.3a, b, in the absence of mixing and chemistry, an AP will not change its coordinates in the tracer space although it will move in the physical space (e.g. vertical displacement of APs shown in Fig. 2.4b1). Furthermore, if only APs within a limited range of potential temperature are considered, the cross-isentropic transport results in an additional flux of the APs out of (export) or into (import) the considered domain in tracer space. Such vertical export or import of APs is reflected in tracer space as vanishing or growing of certain parts of the correlation line (vanishing parts of the vortex correlation are shown as dashed black curves in Fig. 2.4b2/c2). In the same way, export or import of APs from a limited range of latitudes (or equivalent latitudes) may influence the tracer–tracer correlation, e.g. if the subtropical barrier moves toward the equator.

Generally, the major SSW itself creates vortex fragments which in the time following can either merge and reform a new polar vortex, or can be isentropically mixed with the mid-latitude air. These two possibilities are exemplarily shown in Fig. 2.4b1 and c1 (mixing – fragments B and E; recovery – fragments A, C and D). Note that in the equivalent latitude space, the spatially separated vortex remnants form a compact and coherent circumpolar structure although smaller than the vortex at the beginning of the winter. Finally, also chemistry can influence the N_2O–O_3 correlations as discussed in Fig. 2.3c. Particularly, halogen or NO_x-induced ozone loss would shift the polar or the surf zone correlations downwards, whereas ozone production in the low latitudes would steepen the tropical or the surf zone correlations.

2.3 A case study: 2009 major sudden stratospheric warming

Sudden stratospheric warming (SSW) was first reported as early as 1952 based on radiosonde measurements over Berlin (*Scherhag*, 1952). SSWs are characterized by a rapid and intensive temperature rise (up to 30-40 K) in the middle stratospheric polar region as well as a reversal of westerly zonal wind (e.g., *Quiroz*, 1975; *Labitzke*, 1977; *Schoeberl*, 1978). The mechanism of SSWs has been understood as a result of breaking waves propagating from the troposphere upwards

into the stratosphere (*Matsuno*, 1971). Although the understanding of SSWs has been improving in the last six decades, there is still no standard criterion to identify SSWs. The definitions for SSW and classifications are extensively discussed by *Butler et al.* (2015). SSWs are usually classified as major warming, minor warming and final warming. The main difference of major and minor warming is whether the zonal mean zonal wind reverses. Final warmings are charactered by the establishment of easterlies without recovery to westerlies, which indicates the seasonal shift from winter to summer in the stratosphere.

We will only focus on the major mid-winter SSW (major SSW from now on). The most commonly used major SSW definition in the related studies was proposed by *Charlton and Polvani* (2007) (CP07 from now on). The zonal-mean zonal wind at 60°N and 10 hPa is used as the criterion of SSW (CP07). The advantage of this criterion is that it is easy to use and contains a lot of details to separate two close SSWs and to separate SSWs from the final warmings. The shortcoming is its simplicity that only one latitude and one pressure level are considered (*Butler et al.*, 2015). Moreover, as has been pointed out (*Taguchi*, 2011; *Gómez-Escolar et al.*, 2014), use of the highest polar cap temperature instead of the zonal wind reversal at 60°N and 10hPa, characterizes the response of the BDC to SSWs better. In the following, we emphasize the dynamics of SSW and the response of the BD circulation to SSW. Therefore, we use CP07 to identify the major SSW and use the 5-day smoothed polar cap temperature within $\pm$5 days of the wind reversal date to define the central date (or SSW onset date).

To improve the understanding of SSWs, many case studies based on reanalysis data, modeling and/or satellite data have been performed. *Manney et al.* (2005, 2008) described the synoptic evolution during the 2004 and 2006 Sudden Stratospheric Warmings (SSW). Based on the Aura Microwave Limb Sounder (MLS) observations, the meteorology and trace gases from the UTLS to the lower mesosphere during 2006 and 2009 SSW were extensively studied (*Manney et al.*, 2009a,b). Using satellite temperature measurements during three major SSWs, an anomalously strong descent of mesospheric air into the upper stratosphere was found along with the stratopause breaking down and then reforming above 75 km (*Manney et al.*, 2008, 2009b; *Randall et al.*, 2009; *Orsolini et al.*, 2010). The major SSW in 2009 was the most intensive and prolonged case in the record (*Manney et al.*, 2009b) and this event happened although typical known external factors, e.g. the Quasi-Biennial Oscillation, the Southern Oscil-

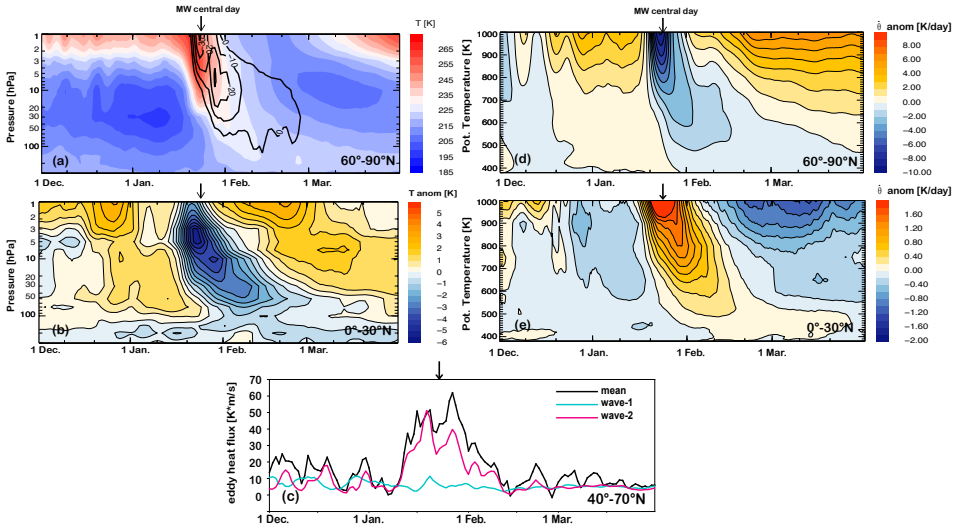

Figure 2.5: **(a)** Polar cap area weighted mean temperature (60–90°N) overlaid with zonal mean easterlies at 60°N (black contours in $\mathrm{m\,s^{-1}}$), **(b)** tropical zonal mean temperature anomaly from the 24-year climatology (0–20°N), **(c)** eddy heat flux (40–70°N, black) on 100 hPa and its decomposition into wave-1 (blue) and wave-2 (red) components **(d)** polar mean (60–90°N) anomaly of the heating rates from the 24-year climatology $Q = \mathrm{d}\theta/\mathrm{d}t = \dot{\theta}$ (for more details see the text), **(e)** same as **(d)** but for 0–30°N. The figures are based on the ERA-Interim reanalysis.

lation, the 11-year sunspot cycle, were all unfavorable for the occurrence of a SSW (*Labitzke and Kunze*, 2009). *Ayarzagüena et al.* (2011) and *Harada et al.* (2010) studied this event from the perspective of tropospheric forcing. Both studies pointed out that the pronounced planetary wave-2 in the stratosphere, which triggers the SSW, is associated with a high-pressure ridge over the Pacific.

2.3.1 Dynamical background

Figure 2.5 gives an overview of the dynamical background during the boreal winter 2008/09 based on ERA-Interim reanalysis. Following the central date definition above, 23 January is used as the central day in our study. Figure 2.5a

shows that the sudden rise of the polar cap temperature started in the upper stratosphere, around 10 January at 1 hPa. Thereafter, the warming propagated downward, arriving at 10 hPa and descended to the lower stratosphere until late January. The increase of polar temperature was accompanied by the generation of easterlies, which are also shown in Fig. 2.5a (black contours). The rise in easterlies and temperature lasted only 10 days at 1 hPa followed by a strong polar vortex cooling while the disturbance of wind and temperature in the lower stratosphere lasted more than 1 month without a complete recovery until the final warming in the spring of 2009.

Before the major SSW, the lower stratosphere in the tropics was slightly warmer than the long-term average due to the westerly phase of the QBO in this winter. Similar to the warming in the high latitudes, the tropical cooling (Fig. 2.5b) also started at about 15 January at 1 hPa and descended from the upper to the lower stratosphere over 2 weeks. As discussed in *Randel et al.* (2002), time-dependent upwelling in the tropical lower stratosphere is correlated with transient extratropical planetary waves, which transport heat from the tropics to high latitudes and, in turn, drive the BD-circulation.

A widely used diagnostic of upward-propagating planetary waves is the vertical component of the EP flux, for which the strongest contribution results from the horizontal eddy heat flux $\overline{v'T'}$ with $v' = v - \bar{v}$, $T' = T - \bar{T}$ and with the overbar denoting zonal mean and primes describing the deviations (i.e. fluctuations) for the temperature T and for the meridional velocity v (*Andrews et al.*, 1987; *Newman et al.*, 2001). Figure 2.5e shows the time evolution of the eddy heat flux at 100 hPa averaged between 40 and 70°N, which explains more than 80 % of the variability of the total vertical component of the EP flux. In addition, contributions of the wave-1 and wave-2 components to the mean eddy heat flux are also shown.

Newman et al. (2001) pointed out that the eddy heat flux measures activity of the waves and is highly correlated with the time evolution of the stratospheric polar temperature. As can be deduced from Figs. 2.5e and 2.5a (or Fig. 2.5b), the mean eddy heat flux at 100 hPa was well correlated with warming at the North Pole and cooling in the tropics. It shows a 1–2 weeks oscillation ranging within 0–25 K m s^{-1} in December and it began to increase from 6 January reaching the first peak on 18 January. After several days of a slight decay, it rose up to the second peak on 27 January and then gradually declined to zero around mid-February with some small fluctuations afterwards. The dominant wave number

before and during the major SSW was wave-2, which led to the vortex split. The dominant and extraordinary planetary wave-2 is associated with unusual development of the upper tropospheric ridge over Alaska (*Ayarzagüena et al.*, 2011; *Harada et al.*, 2010). However, after the major SSW, the main contribution to the total eddy heat flux resulted from higher wave numbers.

Large-scale tropospheric waves can propagate upward into the stratosphere through weak westerlies and break at the critical level, disturbing the mean flow (*Dickinson*, 1968; *Matsuno*, 1971). Such a transient wave breaking converts the zonal flow momentum to mean meridional circulation, and thus drives the extratropical downwelling and tropical upwelling of the BD circulation (e.g. *Holton et al.*, 1995). The temperature perturbations discussed above and shown in Fig. 2.5a, b result directly from diabatic heating and cooling caused by these wave-driven vertical motions. Subsequently, temperatures gradually relax toward their radiative equilibrium values by additional radiative cooling or heating, causing vertical motion, i.e. down- or upwelling, through isentropic surfaces. The polar and tropical (total) diabatic heating rate anomalies from the 24-year mean of ECMWF meteorological ERA-Interim reanalysis (*Dee et al.*, 2011) are shown in Fig. 2.5d, e. As expected, diabatic polar downwelling and tropical upwelling (quantified by these heating rates) were both accelerated after the onset of the major SSW. The polar vortex descent rate strongly increased around 25 January up to 15 K day^{-1} on 1000 K and only around 3 K day^{-1} on 500 K during the late January. The variability of the polar vortex descent rate reported here is consistent with findings by *Manney et al.* (2009b) and *Lahoz et al.* (2011) where the tracer isopleths method based on MLS observations of N_2O, CO and H_2O was used. The onset of the heating rate anomalies at each altitude, and thus their downward propagation, is roughly synchronous with the temperature anomalies shown in Fig. 2.5a, b. The radiative decay of the anomalies takes only about 10 days at 1000 K, but more than 1 month below 500 K. This is consistent with the stratospheric radiative relaxation time inferred from satellite measurements (*Mlynczak et al.*, 1999), which was found to increase from 10 days at 1 hPa to about 100 days at 50 hPa. This is also consistent with a strong suppression of planetary-wave propagation into the vortex after major SSW (*Hitchcock and Shepherd*, 2013).

2.3.2 Model setup

CLaMS simulations cover the 2008/09 boreal winter from 1 December 2008 to 1 April 2009 and extend between the Earth's surface and the potential temperature $\theta = 2500\,\mathrm{K}$ (i.e. roughly around the climatological position of the stratopause with $p \approx 0.3\,\mathrm{hPa}$). The horizontal separation of the APs, which were initialized on 1 December, is 70 km in the NH, where all our results are obtained, and 200 km in the SH. During the course of the simulation, this irregular grid of APs undergoes advection along the trajectories, chemistry and mixing every time step, with $\Delta t = 24\,\mathrm{h}$ (*Konopka et al.*, 2004; *Grooß et al.*, 2005; *Pommrich et al.*, 2014).

The horizontal winds are prescribed by the ECMWF ERA-Interim reanalysis (*Dee et al.*, 2011). To resolve both transport processes in the troposphere influenced by the orography and in the stratosphere where adiabatic horizontal transport dominates, a hybrid coordinate is used as proposed by *Mahowald et al.* (2002). In the stratosphere and in the UTLS, potential temperature θ is employed as the vertical coordinate of the model above about 300 hPa and the cross-isentropic velocity $\dot{\theta} = Q$ is deduced from the ERA-Interim forecast total diabatic heating rates Q, including the effects of all-sky radiative heating, latent heat release and diffusive heating as described by *Ploeger et al.* (2010). The time evolution of the anomaly of $\dot{\theta}$ averaged over the polar cap and over the tropics is shown in Fig. 2.5c, d and was discussed in the previous section.

N_2O and O_3, the most important species for this work, are initialized from the MLS data (more details on MLS can be found in the next subsection). The other chemical species are initialized from a multi-annual CLaMS simulation with simplified chemistry (*Pommrich et al.*, 2014) as well as from gridded MLS data of HCl, H_2O and CO. The employed method uses tracer–tracer correlations (for more details see *Grooß et al.*, 2014). At the upper boundary (2500 K) O_3 is set to the HALOE climatology after every 24 h time step. However, the impact of the upper boundary condition on the chemical tracers is not significant below 1000 K and our following analyses focus on levels below 1000 K. The chemistry module of CLaMS is described in detail in *McKenna et al.* (2002b).

By switching the mixing module off and on, we carried out two sets of simulations: full chemistry without mixing and full chemistry with mixing. The simulation with full chemistry and with mixing is the reference as the best model representation of the real atmosphere. Both simulations include ozone calculated with full chemistry (O_3) and passively transported O_3 without any chemistry

(pO_3).

2.3.3 Validation with MLS observations

MLS observes microwave emission from the limb of the Earth's atmosphere in the direction of the Aura orbit. The instrument measures vertical profiles every 165 km (1.5°along the Aura orbit), providing about 3500 profiles per day. We use version 3.3 N_2O and O_3 from the MLS product (*Livesey et al.*, 2013) both to initialize and to validate the CLaMS reference simulation. The vertical resolution of O_3 is about 2.5–3 km in the stratosphere with a 5–10 % uncertainty (*Livesey et al.*, 2013). The vertical resolution of N_2O is about 4–6 km with a 9–25 % uncertainty for the region of interest in this study (*Livesey et al.*, 2013). Averaging kernels are involved in the retrieval of the MLS profiles, which relate the retrieved MLS profiles to the true atmospheric state.

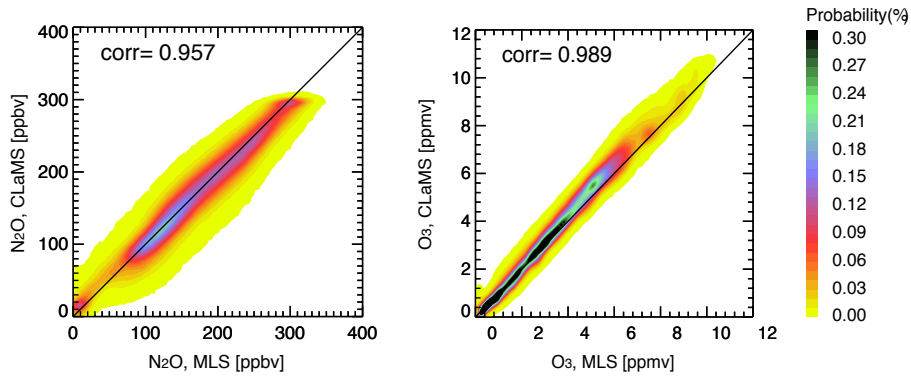

Figure 2.6: PDFs (probability distribution functions) of MLS observations and CLaMS reference simulation for the entire simulation period from 1 December 2008 to 1 April 2009 for APs in the Northern Hemisphere with 400 K $<$ θ $<$ 1000 K (left: N_2O, right: O_3).

For comparison, we map CLaMS mixing ratios to the observed MLS profiles using a back and forward trajectory technique (*Ploeger et al.*, 2013) and apply the MLS averaging kernels to CLaMS output in order to get comparable quantities (see Appendix). Because CLaMS APs are saved every day only at 12:00 UTC,

we calculate the noon-positions of the MLS observations within a 1-day window using back and forward trajectories, and then select the nearest CLaMS AP to the corresponding MLS observation. The mixing ratios at this AP are then compared with the respective MLS observations.

Hereby, a one-to-one MLS-CLaMS data set for N_2O and O_3 is established that is plotted in Fig. 2.6 as probability distribution functions (PDFs) calculated for the whole NH and for the entire simulation period (around 10 thousand points). According to a high correlation coefficient both for N_2O (0.957) and for O_3 (0.989), our reference simulation matches the MLS observations fairly well. The largest difference was diagnosed in the θ-range between 650 and 1000 K where CLaMS O_3 slightly overestimates the MLS observations. Three possible explanations for this small bias are: (1) there was not enough NO_x-induced ozone loss; (2) there was too much photolytical ozone production; (3) poleward transport from the tropics was too fast.

For a further comparison, we investigate the horizontal distribution of N_2O. Figure 2.7 shows the comparison between the CLaMS simulation and MLS observations for five selected days at $\theta = 800$ K (top 2 panels) and 475 K (bottom 2 panels). On 9 January, the vortex was centred around the North Pole and the vortex edge was well defined and not changing rapidly in the middle and lower stratosphere. Mainly influenced by the planetary wave-2, the polar vortex stretched to North America and Asia on both heights during the following days. Around the central day of the major SSW at 23 January, a double centre structure formed which split up until 25 January at 475 K and until 28 January at 475 K (not shown).

In the following days, an increasing number of filaments could be observed outside of the vortex characterized by low N_2O values. The two vortex centres slowly rotated anticlockwise. One of the vortex remnants over eastern North America and the Atlantic stretched further, split and dissolved, releasing its content to mid latitudes, while another one stayed over northern Asia and the Pacific Ocean. Although in the following weeks most of the vortex fragments were mixed with mid-latitude air, a part of them, like those over northern Asia and the Pacific Ocean, re-organized as a new and relatively weak vortex. However, this top-down process that started in late February at 800 K (a weak, circumpolar vortex edge can be diagnosed at $\theta = 800$ K at 20 February, see Fig. 2.7) and was finished in mid March at 475 K (not shown), is excluded from our analysis, which ends with 28 February.

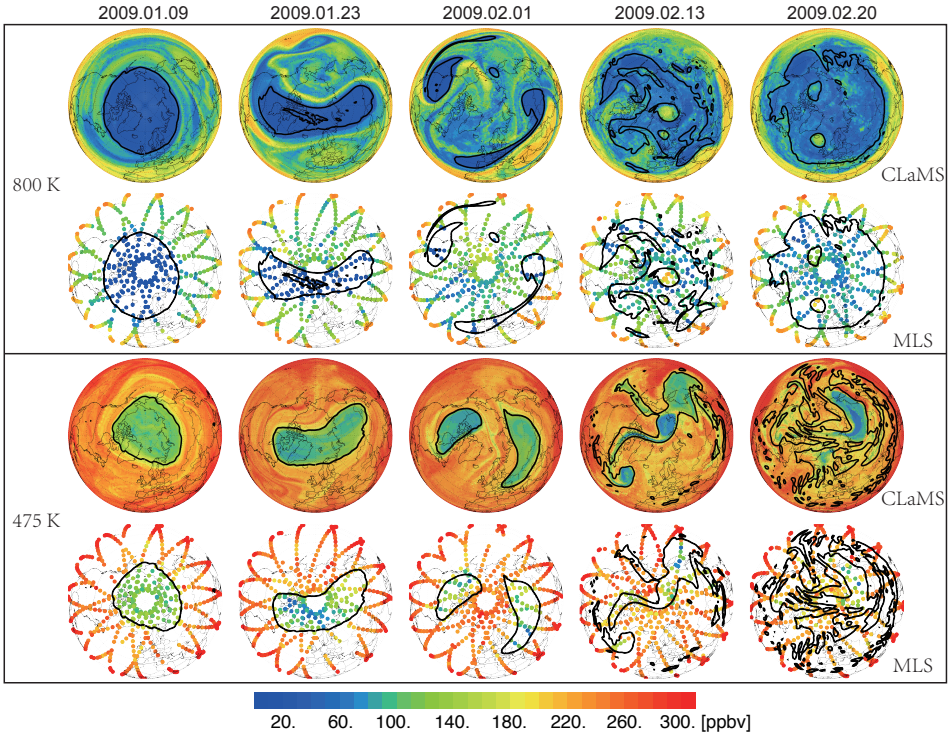

Figure 2.7: N_2O distribution at $\theta = 800\,K$ (top 2 rows) and 475 K (bottom 2 rows) interpolated from CLaMS simulation and MLS observations for five selected days in 2009 before and after the major SSW event. Nash's criterion (*Nash et al.*, 1996) is applied to define the edge of the polar vortex shown as the black contours. According to this method, the vortex edge is identified as the maximum PV (potential vorticity) gradient with respect to equivalent latitude constrained by the location of the maximum wind jet calculated along equivalent latitudes.

The distribution of simulated N_2O accurately represents the MLS observations, although more filamentary structures are resolved in the CLaMS simulations than MLS observations. It should be noted that applying averaging kernels to model result also smoothes out some valuable information, e.g. filamentary structures, and, consequently, may result in a misinterpretation of the stra-

tospheric composition, especially for high-latitude N_2O. More details are discussed in the Appendix A.1.

2.3.4 Planetary waves and mixing

Transport and mixing barriers in the winter hemisphere

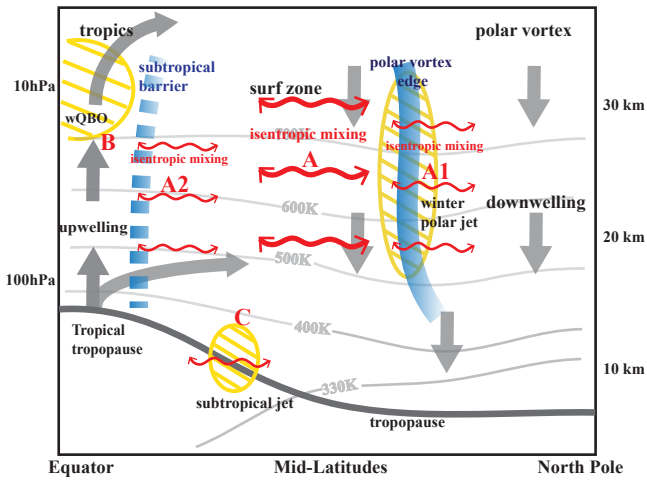

Figure 2.8: Schematic diagram of transport and mixing processes in the winter stratosphere. The thick blue lines show the barriers, the grey arrows indicate the direction of the BD circulation. Yellow shaded areas stand for strong westerlies. Red two-headed arrows indicate isentropic mixing, with thicker and thinner arrows showing stronger mixing in the surf zone and weaker mixing across the transport barriers, respectively. For a better overview, the tropopause with the subtropical jet is also marked.

In the winter stratosphere, two main barriers to transport exist, shown by the two thick blue lines in Fig. 2.8 (*Holton et al.*, 1995). One is the polar vortex edge, which can be identified as the maximum gradient of potential vorticity (PV) with respect to equivalent latitude within a certain range where the maximum of wind speed along equivalent latitudes (in the following equivalent latitude) occurs (*Nash et al.*, 1996). The second barrier (around 10–30°N equivalent latitude, varying with altitude) separates the mid-latitude surf zone (*McIntyre*

and Palmer, 1983) from the region of tropical upwelling, the so-called tropical pipe (*Plumb*, 1996).

This subtropical barrier is not as well-defined as the polar vortex edge and is usually characterized by a much weaker PV gradient between tropics and mid latitudes (*Polvani et al.*, 1995) although large meridional tracer gradients can be diagnosed (*Shuckburgh et al.*, 2001; *Punge et al.*, 2009; *Konopka et al.*, 2010). While the polar vortex edge is considered as a meridional transport barrier due to a strong polar jet, the subtropical barrier is only weakly influenced by the jets and is usually understood as a barrier for propagation of planetary waves. This barrier is strongly related to the phase of the quasi-biennial oscillation (QBO): during the westerly QBO, planetary waves generated in the winter hemisphere can propagate across the equator to dissipate at the summer hemisphere easterlies, whereas such propagation is suppressed during the easterly QBO phase (*Haynes and Shuckburgh*, 2000; *Shuckburgh et al.*, 2001; *Punge et al.*, 2009). Thus, during the 2008/09 winter, the subtropical transport barrier was weakened by the westerly QBO phase (dashed thick blue line in Fig. 2.8).

In a winter with weak activity of planetary waves and a strong vortex, the exchange and mixing of air across the vortex edge is suppressed. However, once a strong sudden warming event happens that usually follows a significant weakening of the vortex edge (with exceptions e.g. for the 2013 SSW, *Manney et al.*, 2015), enhanced wave forcing drives significant isentropic, two-way mixing (red curved arrows) as well as the large-scale BD circulation (grey arrows). The evolution of the dynamical fields, including cross-isentropic vertical velocity $\dot{\theta}$ and zonal wind, was discussed in the previous section (Fig. 2.5). But isentropic mixing and its relation to wave forcing need further investigation.

CLaMS mixing versus wave forcing

Mixing between the Lagrangian APs is parametrized in CLaMS through adaptive re-gridding. During this process, the involved APs (i.e. APs, which were generated by the mixing algorithm), are marked after every 24 h time step. Here we use the statistics of these events, i.e. the percentage of mixed APs relative to all transported APs, in the following denoted as mixing intensity. Note that the mixing state of the APs is newly marked for each time step, i.e. no accumulating of mixing intensity. In this way, we illustrate the impact of the major SSW on the distribution and evolution of mixing resolved by the model.

Figure 2.9 shows the time evolution of the zonally averaged mixing intens-

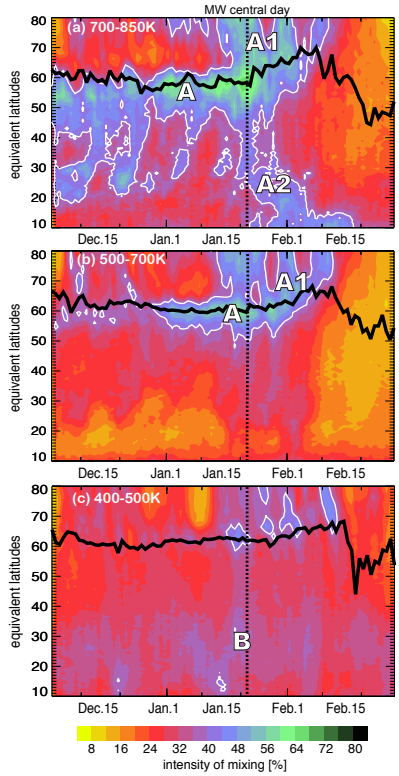

Figure 2.9: CLaMS zonal mean mixing intensity within three layers: **(a)** 700–850 K, **(b)** 500–700 K and **(c)** 400–500 K overlaid by the location of the vortex edge (thick black lines *Nash et al.*, 1996). The white contours indicate the mixing intensity of 40 %. The letters mark the regions of high mixing intensity and correspond to the letters in Fig. 2.10.

ity derived from CLaMS versus equivalent latitude. Figure 2.10 illustrates the relationship between the EP flux divergence and the CLaMS mixing intensity averaged over several stages of the polar vortex during the winter of 2008/09: (a) strong vortex conditions in January between 3rd and 13th, (b) 10-day period before the major SSW, i.e. between 14 and 23 January, (c) 10-day period after the major SSW, i.e. between 24 January and 3 February, and (d) weakened wave activities after the major SSW between 4 and 13 February.

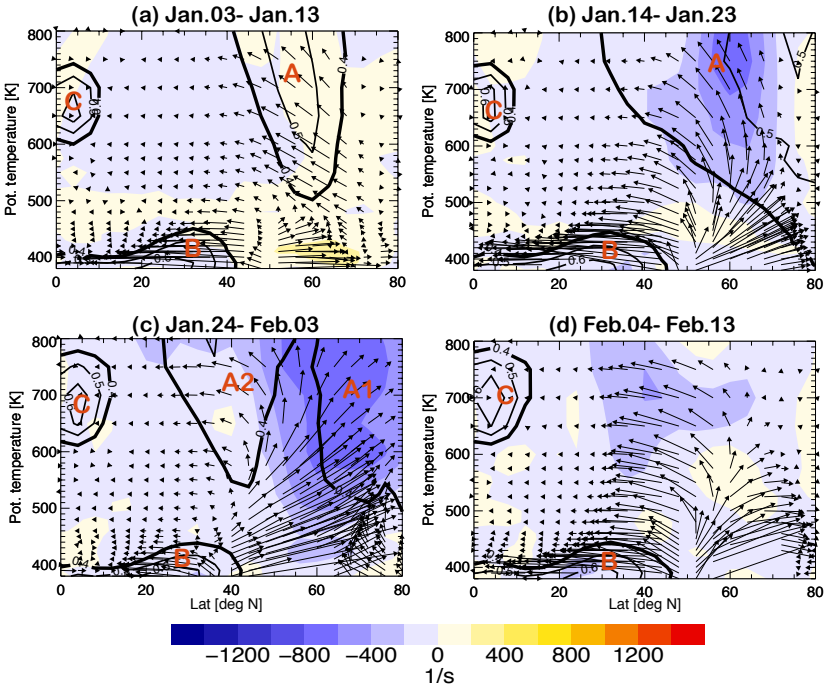

Figure 2.10: EP flux (arrows) and its divergence (coloured bluish). Black contours indicate the mixing intensity larger than 0.4. The panels **(a)**–**(d)** show mean values averaged over four time periods: **(a)** 3–13 January, **(b)** 14–23 January, **(c)** 24 January–3 February and **(d)** 4–13 February.

We notice that before mid January, maximum mixing remains equatorward of 65°N and generally outside the polar vortex boundary as defined by the Nash criterion (Fig. 2.9). In particular, above 700 K the rather abrupt poleward decrease in mixing strength clearly marks the polar mixing barrier isolating the core of the stable polar vortex from the surf zone. Note that the Nash criterion is not necessarily a perfect proxy for the mixing barrier, thus mismatching to

within a few degrees latitude, as apparent in Fig. 2.9a. In mid January the picture changes drastically. With the intensified wave activity disturbing the polar vortex, the westerlies decelerated. Consequently, the EP flux increased and its divergence became strongly negative, meaning an enhanced convergence of the EP flux (Fig. 2.10). Furthermore, the pattern of mixing intensity separated into two branches above 700 K after 24 January (Fig. 2.9a): one in high and another one in mid equivalent latitudes (marked as A1 and A2 in Figs. 2.9a and 2.10c, respectively).

This distribution of mixing intensity indicates that both the polar and subtropical barrier (the latter above 700 K) are weakened by the major SSW. Furthermore, daily PV or tracer distributions over the NH (cf. Fig. 3) exhibit that at this time several vortex fragments move equatorward and mix with mid-latitude air. At the same time, several fragments of tropical air masses which are generated at low latitudes, are transported poleward and mixed with mid- or high-latitude air.

Mixing intensity diagnosed in Fig. 2.9 shows some interesting, altitude-dependent patterns: At the highest levels (θ between 700 and 850 K) after the major SSW, the mid- and high-latitude mixing is comparable (cf. A1 versus A2 in Fig. 2.9a). At the levels between 500 and 700 K, the high-latitude mixing branch within the vortex dominates. Finally, in the lower stratosphere between 400 and 500 K, mixing has intensified in the polar region after the major SSW, while the mixing intensity in the surf zone (marked by B in Fig. 2.9c) has slightly increased during and after the major SSW. Note that the subtropical barrier can be identified as a minimum in mixing intensity between 10 and 20°N equivalent latitude (Fig. 2.9b). The position of this minimum does not significantly change during the time shown although the impact of the major SSW can be seen around 1 February, mainly at highest levels between 700 and 850 K.

From the vertical cross sections of EP flux shown in Fig. 2.10, we infer that in the first half of January, there were three intensive mixing regions (marked as A, B and C) with only weak, vertically propagating waves. As mentioned above, region A became stronger during the course of the winter and then divided into two branches (A1 and A2). Region B is related to the mid-latitude (surf zone) mixing in the lower stratosphere (400–500 K) that is influenced by the subtropical jet and the QBO. Region C is associated with strong vertical shear in the transition layer between the westerlies and easterlies of the QBO.

It is obvious that although high mixing intensities can be diagnosed in the

surf zone outside of the polar vortex (region A) before the major SSW, this signature intensifies after the onset of the major SSW (regions A1 and A2). Convergence of the EP flux indicates breaking of waves and thus to wave and mean-flow interaction. Once the local wind field is significantly disturbed by transport of momentum and heat flux, subsequent stirring and stretching of eddies (resolved by the ECMWF winds) drives the mixing parameterization in CLaMS. Note that after 10 February (20 days after the SSW), the mixing intensity quickly dropped as the vortex started to recover with a weak vortex edge between 50 and 60°N equivalent latitude at 800 K and 50°N equivalent latitude at 600 K (i.e. with a weak PV gradient according to the Nash criterion).

Based on the analysis of the temporal and spatial evolution of the mixing intensity resolved in CLaMS and the EP flux divergence, the simulated patterns show a clear and reasonable physical picture how mixing responds to large-scale wave forcing: when the transport barriers stay strong, the mixing pattern does also not change dramatically (Fig. 2.10a); when the general circulation is disturbed and the transport barriers are weakened, the pattern of mixing is highly associated with the local wave activities (Fig. 2.10b and c). However, the question still arises whether mixing resolved by the model can also be seen in the observations. This would help to provide a more quantitative understanding of how the major SSW influences the chemical composition of the stratosphere.

2.3.5 Impact of the MW on transport and chemistry

N_2O–O_3 correlations: MLS versus CLaMS

As discussed in the last section, the subtropical barrier and even more so the polar vortex barrier suppress the exchange of air across those barriers before the major SSW. Hence, long-lived species are well-mixed in the regions separated by these barriers and strong isentropic gradients of these species are expected across such barriers. In the tracer–tracer space (in the following abbreviated as tracer space), these well-mixed regions manifest as compact correlations; however correlations between the tracers are different in the regions separated by barriers (for a review of this method see *Plumb*, 2007).

Figure 2.11a1–c1 show the N_2O–O_3 correlations of MLS observations plotted as probability distribution functions (PDFs). The data cover the NH with equivalent latitudes between 0 and 90°N and within the potential temperature range between 450 and 700 K. The MLS observations are selected for three peri-

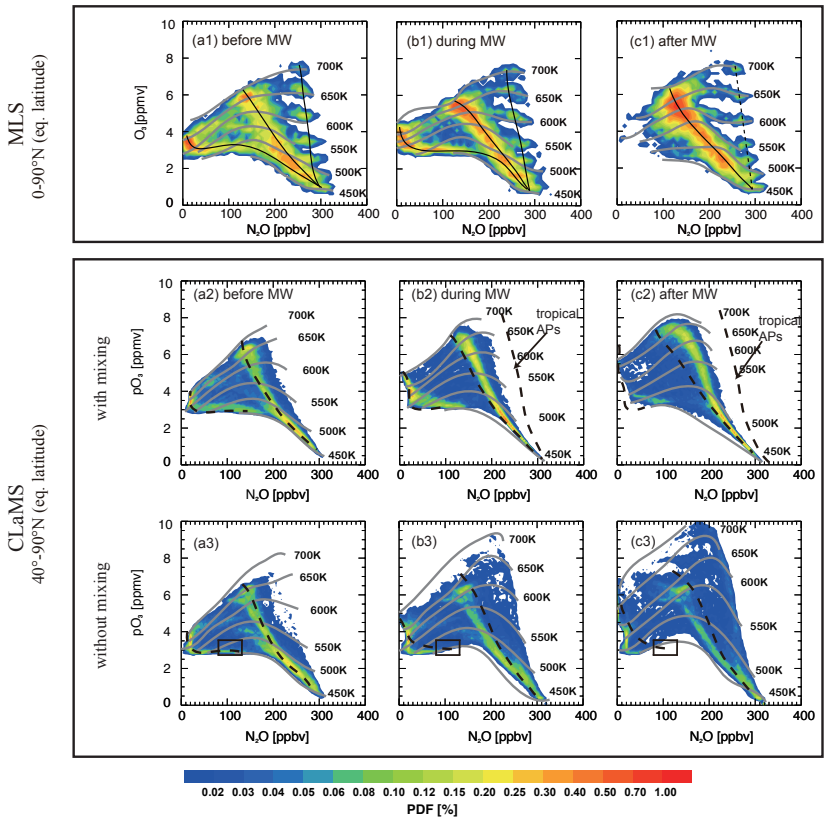

Figure 2.11: PDFs of N_2O–O_3 correlations (tracer space) shown for three periods: **(a)** 18–28 December, **(b)** 18–28 January and **(c)** 18–28 February. The top row (a1–c1) is based on the MLS observations within equivalent latitudes 0–90°N and potential temperature range between 450 and 700 K. The black lines in (a1–c1) represent the respective correlation branches (polar, surf-zone, tropics). The middle and bottom rows show CLaMS simulations without ozone chemistry but with and without mixing, respectively. CLaMS PDFs are calculated from the APs with the same potential temperature range but with equivalent latitudes between 40 and 90°N. The grey lines mark the isentropes (450, 500, 550, 600, 650, and 700 K). For better comparison between CLaMS with and without mixing, the dashed black curves in (a2–c2) show the estimated N_2O–O_3 correlation line from the case without mixing (i.e. from a3–c3). Reversely, dashed lines in (a3–c3) depict schematically transferred correlation branches from CLaMS with mixing (i.e. from a2–c2).

ods: 18–28 December (1 month before the major SSW), 18–28 January (during the major SSW) and 18–28 February (1 month after the major SSW). The grey lines in Fig. 2.11a1–c1 indicate the isentropes calculated from the pressure altitude of the observations and corresponding ECMWF temperature.

Under relatively strong vortex conditions before the major SSW, two stronger and one weaker branch of N_2O–O_3 correlations with enhanced PDF values can be distinguished in Fig. 2.11a1. These branches describe the well-mixed air masses within the polar vortex, the surf zone and the tropics (thin black lines from bottom to the top, respectively). The corresponding barriers in the physical space, i.e. the vortex edge and the subtropical barrier, manifest in tracer space as regions with lower PDF values separating the correlation branches (a detailed discussion follows in the next subsection). After the major SSW (see Fig. 2.11c1), the polar correlation totally disappears in tracer space and the tropical correlation becomes slightly weaker. Conversely, the PDF of the mid-latitude correlation strengthens in the time period after the major SSW.

Our first goal is to understand the changes in the N_2O–O_3 correlations observed by MLS before and after the major SSW (Fig. 2.11a1 to c1) as a result of different transport mechanisms (isentropic mixing, meridional transport). In particular, we would like to figure out why the polar and the tropical N_2O–O_3 correlations weakened after the major SSW and the mid-latitude correlation became stronger. First, we rule out ozone chemistry by using CLaMS simulations with passively transported O_3 (pO_3). At the end of this section, we will also include CLaMS results with the full stratospheric ozone chemistry.

2.3.6 Isentropic mixing versus cross-isentropic transport

Two sets of CLaMS simulations, with and without mixing, are used to study the mixing-induced differences between the PDFs of the pO_3–N_2O correlations. The results are shown in Fig. 2.11 (middle/bottom row for mixing/non-mixing cases). As in Fig. 2.11a1–c1, the PDFs are calculated for the same time periods before, during and after the major SSW (from a to c). However, the range of the considered equivalent latitudes is confined to 40–90°N (instead of 0–90°N shown in Fig. 2.11a1 to c1) to separate more clearly the effect of transport from the tropics on the composition of air in the mid latitudes (see discussion below). To provide better comparability, correlation branches of the non-mixing experiment are also depicted in the mixing case as dashed lines (and vice versa).

Transport from the tropics

By using such a limited range of equivalent latitudes, we exclude the APs on the tropical side of the subtropical barrier (that is around 20°N equivalent latitude) and it is obvious that the PDFs of the CLaMS run with mixing do not show any tropical correlation in the equivalent latitude 40–90°N (Fig. 2.11a2 to c2). However, a tropical correlation was found in the non-mixing run during and after the major SSW (Fig. 2.11b3/c3) because in this idealized simulation, tropical air was transported into the mid latitudes but had not been mixed. For a better comparison, this "artificial" tropical correlation (i.e. from Fig. 2.11b3/c3) is also shown in Fig. 2.11b2/c2 (solid dashed line).

Thus, a clear difference in the result of the mixing and non-mixing case indicates that the tropical APs are transported from lower latitudes to mid latitudes where they mix with the mid-latitude APs. Consequently, the slope of the surf-zone correlation moves towards the tropical correlation branch, especially between 550 to 650 K (cf. Fig. 2.11 from a2 to c2 and c2 with c3). This isentropic mixing in mid latitudes is also consistent with the increased mixing intensity marked as A2 in Figs. 2.9 and 2.10. In contrast, an idealized, pure trajectory calculation (i.e. CLaMS without mixing) completely neglects this effect and produces N_2O-O_3 correlations which cannot be reconciled with MLS observations (i.e. for equivalent latitudes 40–90°N, not shown).

Vortex breakup and decay

All APs which are transported along the trajectories without mixing do not change their composition and thus keep the same position in the N_2O–O_3 space unless they leave the considered range of equivalent latitudes or potential temperatures. Besides the almost isentropic import of tropical APs that was mentioned in the last subsection, strong downwelling within the polar vortex, mainly during the major SSW itself, can also be diagnosed in the tracer space.

The isentropes move upwards in tracer space during the major SSW (Fig. 2.11 from column a to b), as a consequence of diabatic cooling (downwelling) associated with warming in mid and high latitudes (see also Fig. 2.4). As a result of this cross-isentropic transport, the APs transported without mixing may be exported (or imported) from (or into) the considered θ-range between 450 and 700 K. For example, the polar APs within the black solid squares in Fig. 2.11a3 are missing in the box of Fig. 2.11c3. The box is defined by the N_2O

values between 80 and 130 ppbv and O_3 between 2.7 and 3.5 ppmv. Note that for CLaMS with mixing these regions are filled with APs indicating that mixing in the model re-establishes parts of the correlation.

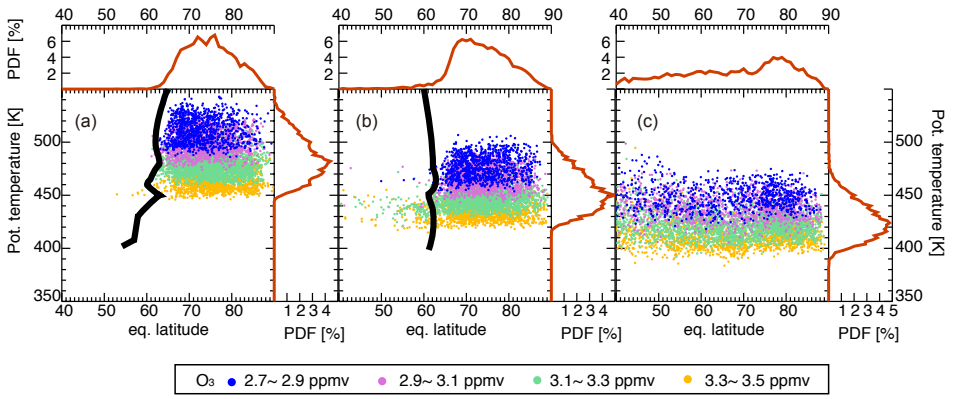

Figure 2.12: Spatial distribution in the equivalent latitude-θ space of the APs, defined by the mixing ratios of N_2O and pO_3 inside the square in Fig. 2.11a3, i.e. with N_2O and pO_3 values from 80 to 130 and from 2.7 to 3.5 ppmv, respectively, calculated from the CLaMS run without mixing. **(a)** 23 December 2008; **(b)** 23 January 2009 and **(c)** 23 February 2009. Colours indicate different ranges of pO_3 values and are defined in the box. The PDFs along the equivalent latitude and potential temperature axes are shown as red lines. Thick black lines denote the edge of the polar vortex.

To shed more light on the ongoing processes, in Fig. 2.12 we plot the equivalent latitudes and the potential temperature coordinates of these missing APs at the end of each of the considered time periods (from the CLaMS run without mixing). Furthermore, the APs are coloured by different ranges of pO_3 and the PDFs of their equivalent latitudes and θ coordinates describe their mean horizontal and vertical position during the course of the winter.

Figure 2.12 shows that after the major SSW onset, most of the APs which were originally located above 450 K, have been transported downwards below 450 K. Therefore, the downward cross-isentropic transport within the vortex (diabatic descent) with subsequent export of the APs out of the considered potential temperature range 450–700 K is the main reason for the missing correlation

inside the square of Fig. 2.11c3. Moreover, most of the APs were confined inside the polar vortex before the major SSW, while after the major SSW these APs were spread almost uniformly between 40 and 90°N equivalent latitude (Fig. 2.12c) due to chaotic advection with pronounced streamers and filaments after a complete breakup of the two vortices over eastern North America and the Atlantic (see N_2O distribution at 475 K in Fig. 2.7).

In the CLaMS run with mixing, the situation is stable as long as the well-defined vortex edge constitutes an effective mixing barrier (Fig. 2.11, column a). Later, during the major SSW, descent and chaotic advection have the same effect as in the idealized CLaMS simulation without mixing, i.e. part of the APs carrying the signature of the polar correlation are again eventually exported from the considered θ-range as they descend below 450 K.

However, increased mixing between these descending polar APs with the APs outside the vortex have two additional effects: (i) the signature of the polar correlation is spread to mid-latitude APs that do not descend beyond the considered θ-range, such that the signature remains visible (like vortex fragment D in Fig. 2.4b1/c1), and (ii) the mixing with mid-latitude (and even tropical) APs causes the polar correlation branch to become less compact and shift toward the mid-latitude correlation branch along the plotted isentropes (like air masses C and E in Fig. 2.4b1/c1). These effects can be well discerned by comparing the vortex branch of the correlation for the mixed case (Fig. 2.11b2/c2) with the non-mixed case (Fig. 2.11b3/c3), also denoted as dashed black curves in Fig. 2.11b2/c2.

After the breakup of the two vortices over eastern North America and the Atlantic in mid February, spreading of the polar APs across the hemisphere along with intense mixing with mostly mid-latitude and some tropical APs leads to an almost complete loss of the polar correlation branch (Fig. 2.11c2), which remains preserved only in a few unmixed vortex remnants (like fragments A, B and D in Fig. 2.4c1). As explained by *Plumb* (2007), the fast and nearly hemisphere-wide isentropic mixing (as promoted by the major SSW) leads to a single compact extratropical correlation.

Note that the weak polar correlation which is present in CLaMS (see Fig. 2.11c2) is not resolved in the MLS observations. A potential explanation is the limited spatial resolution of the MLS instrument with vertical resolution of 4–6 km for N_2O and 2.5–3 km for O_3, respectively, and horizontal resolution of 200 km for both species. This means that physical structures below these spa-

tial scales are smoothed out by the MLS instrument (an effect sometimes called optical mixing, see Appendix).

2.3.7 Impact of chemistry

Arctic O_3 loss is triggered by activated chlorine which mainly occurs in late winter and spring within a sufficiently cold polar vortex. The chlorine-induced ozone-loss also requires sunlight exposure (see e.g. *Solomon*, 1999). The NO_x-induced O_3 chemistry roughly follows the halogen chemistry after the vortex breakup with highest values occurring in the middle and lower stratosphere (see e.g. *Solomon*, 1999; *WMO*, 2014). To quantify the chemical effect on the N_2O–O_3 correlation, Fig. 2.13 shows the pO_3–N_2O correlation within 0–90°N and 450–700 K range, overlaid with the correlations from the full chemistry run (dashed curves).

In the early winter, we found a small but significant amount of ozone loss in the lower stratosphere (cf. dashed curve and PDFs between 450 and 550 K in Fig. 2.13b), which is consistent with the results of *Manney et al.* (2015). After the onset of the warming event, only few polar stratospheric clouds (PSCs) were formed and, consequently, the subsequent, chlorine-induced ozone-loss within the polar vortex was very limited (*Kuttippurath and Nikulin*, 2012; *Manney et al.*, 2015). This can also be inferred from the CLaMS-based correlation with pO_3 (PDFs in Fig. 2.13c) that is very close to the correlation based on full-chemistry O_3 (dashed curve in Fig. 2.13c). Besides the chlorine-catalyzed ozone loss, the NO_x-catalyzed loss of O_3 is of importance in our interpretation of the N_2O–O_3 correlations, especially when the temperature rises after the major SSW and thus most gas- phase chemical reactions are accelerated.

Two regions (marked in Fig. 11 as A and B) of this correlation plot have been investigated in more detail regarding the chemical change of ozone. Region (A) has N_2O mixing ratios near 140 ppbv and passive ozone near 7.4 ppmv on 23 January, corresponding to a most probable location of 35°N and 650 K (using a similar method as discussed in Fig. 2.12). It is evident that here ozone is chemically depleted. From the locations of 120 air parcels in this area, back trajectories were calculated for 1 month along which the chemistry, which was calculated using the CLaMS chemistry module, and additional output to analyse and quantify the contribution of the individual ozone depletion cycles (as defined by *Crutzen et al.*, 1995) to the ozone loss term. The average ozone production over this month through oxygen photolysis was 0.85 ppmv which was

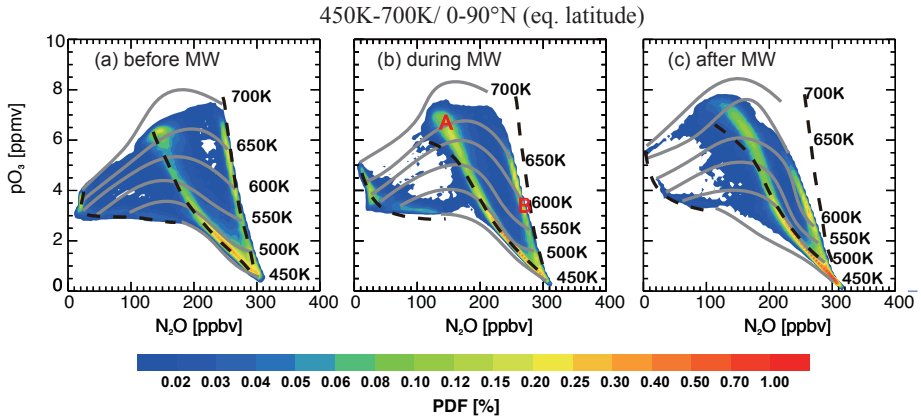

Figure 2.13: Impact of O_3-chemistry on the temporal evolution of the N_2O-O_3 correlations. The PDFs are calculated from the N_2O-pO_3 correlations of APs with equivalent latitudes 0–90°N and potential temperatures 450–700 K. The considered time periods are the same as in Fig. 2.11. The dashed black curves fit the maxima of the N_2O-O_3 correlations (PDFs) derived from a CLaMS run with a full stratospheric ozone chemistry. The correlation for passive ozone (pO_3) marked as A (N_2O near 140 ppbv and pO_3 near 7400 ppbv) and the correlation marked as B (N_2O near 140 ppbv and pO_3 near 7400 ppbv) show clear differences from the dashed curves showing simulation with full chemistry. The two groups of APs marked by those correlation features have been investigated in more detail of their ozone chemistry (see text).

outweighed by ozone loss of 1.45 ppmv, of which about half could be attributed to NO_x-catalyzed ozone loss cycles and the remaining half equally distributed to HO_x, ClO_x and O_x cycles.

In contrast, region (B) with N_2O mixing ratios of 260 ppbv and passive ozone mixing ratios of 3.8 ppmv corresponds to a most probable location of 11°N and 575 K. Here, chemistry causes an ozone increase. A similar chemistry simulation along 132 1-month back trajectories showed an ozone production through oxygen photolysis of 800 ppbv and net ozone depletion by 260 ppbv. Therefore ozone production dominates in this part of the tropics. Since gas-phase chemical reactions are temperature-dependent, we investigated whether the temperature

anomaly (see Fig. 1b) had a significant effect on ozone. An identical run along the 132 trajectories, however, with temperatures set 3 K higher, increased the ozone loss by 0.03 ppmv. The ozone production is not temperature-dependent. A change in the ozone loss rate of 1 ppbv per day is negligible compared to the changes caused by dynamics that are discussed here. Complementary to our discussion above, we find that in polar latitudes, the differences between correlations with or without chemistry are negligible, indicating a minor importance of the chlorine-induced ozone-loss during the 2008/09 winter.

2.4 Remarks

A remarkable major SSW in January 2009 led to strongly disturbed stratospheric dynamics which manifested in both accelerated polar descent and tropical upwelling. During the following 2 weeks up to the end of January, this transient signal of cross-isentropic transport propagated down from around 1 to 100 hPa. The radiative relaxation of this anomaly in diabatic heating was relatively fast ($\sim$ 10 days) in the upper stratosphere, but took more than a month in the lower stratosphere, which resulted in accelerated polar descent and accelerated tropical upwelling through late March (Fig. 2.5).

Associated with the disturbed dynamical background during the major SSW, strong variability of N_2O and O_3 was observed by the MLS instrument. We used CLaMS to simulate transport, mixing and chemistry to interpret the observed change of stratospheric composition. By comparison with MLS observations of N_2O–O_3 correlations, we showed how the polar vortex edge weakened and how the subtropical mixing barrier was affected by poleward transport followed by mixing in mid latitudes during and after the major SSW.

As an important but uncertain piece of atmospheric modelling, the mixing process could be explicitly and reasonably described in CLaMS simulations. The distribution of simulated mixing intensity showed that mixing across the vortex edge and also across the subtropical barrier (above 700 K) was enhanced after the onset of the major SSW, associated with wave forcing, quantified in terms of the EP flux divergence.

The observation- and model-based O_3–N_2O correlations have been shown to be a useful diagnostic to separate dynamical and chemical effects. Model results show that isentropic mixing is a key process to understand the drastic change of stratospheric composition triggered by the major SSW: the decay of the polar

O_3–N_2O correlation and the strengthening of the mid-latitude correlation. One month after the major SSW, almost half of the polar vortex dissolved due to isentropic mixing in O_3–N_2O correlation space, whereas the other part constituted the germ for the formulation of a new and relatively weak vortex. Halogen-induced ozone loss within the polar vortex was negligible in the late winter of 2008/09 and the dominant ozone chemistry during and after the major SSW was the extra-tropical ozone loss due to NO_x catalytic cycles mainly at 600–800 K and ozone production in the tropics.

However, there is also a limitation of the applicability of the MLS satellite data with a vertical resolution of a few kilometres. As shown in the Appendix, due to this limited spatial resolution, physical structures below these spatial scales and resolved by the model are smoothed out by the satellite's averaging kernel (an effect sometimes called optical mixing). Thus, although MLS satellite data offer a very good coverage, their poor vertical resolution does not allow us to narrow the possible range of the mixing parameters in CLaMS (i.e. of the critical Lyapunov exponent).

Finally, we can speculate that for a winter with significant, chlorine-induced ozone loss, followed by a strong major SSW and/or a final warming, the mid-latitude air can be influenced by processed, ozone-depleted air. Conversely, mid-latitude air (also O_3-rich air compared to polar vortex air in mid stratosphere) can be effectively transported into high latitudes.

Chapter 3

Response of water vapor in tropical lower stratosphere to SSWs

A single SSW event as resolved in the satellite observations and CLaMS simulation was discussed in the last chapter. We learned that major SSWs introduce intensive subseasonal variability of stratospheric dynamics and composition in the high latitudes as well as in the tropics during the boreal winter and spring. In this chapter, we will systemically investigate the SSWs in the last 35 years with respect to their impact on the amount of water vapor entering the stratosphere. This chapter is mainly based on the result of *Tao et al.* (2015b).

3.1 Water vapor in the lower stratosphere

As first suggested by *Brewer* (1949), water vapor enters the stratosphere through the cold tropical tropopause layer (TTL), where freeze-drying causes strong dehydration from large tropospheric to very low stratospheric mixing ratios. The fact of extreme dryness in the stratosphere inspired the theory of Brewer-Dobson circulation (BDC) (*Brewer*, 1949; *Dobson*, 1956). Besides the indicative role of mass circulation, the stratospheric water vapor has been receiving considerable attention because stratospheric water vapor has a substantial contribution to climate change: an increase (decrease) of stratospheric water vapor leads to stra-

tospheric cooling (warming) and to tropospheric warming (cooling) (e.g. *Rind and Lonergan*, 1995; *Forster and Shine*, 1999). *Solomon et al.* (2010) assessed the 10% decrease of stratospheric water vapor concentration during 2001-2005 slows the rate of increase in global surface temperature by about 25% that would have been caused by CO_2 and other greenhouse gases over the last decade. *Dessler et al.* (2013) further emphasized the possibility of a positive feedback of stratospheric water vapor to global surface climate change. Moreover, stratospheric water vapor affects stratospheric ozone chemistry through providing the source of OH for the ozone destruction by the HOx cycle as well as participating in the formation of PSCs in the polar regions (e.g. *Evans et al.*, 1998; *Stenke and Grewe*, 2005).

3.1.1 Observations

As early as in the 1940s, stratospheric water vapor has been observed by high-altitude aircrafts and balloons in the United Kingdom (*Rosenlof et al.*, 2001). Based on these early observations, the mean meridional circulation model (BDC as mentioned above) was discovered. Since that time, systematic measurements were carried out using different techniques. The most remarkable one is the multi-decadal (since 1980) water vapor observations with balloon-borne cryogenic frost point hygrometers (FPHs) over Boulder, Colorado (*Oltmans et al.*, 2000a; *Hurst et al.*, 2011). This water vapor observations over Boulder produce the longest in-situ record of water vapor vertical profiles, which is of great value in the study of the relationship between water vapor and climate change. Valuable information on water vapor in the UTLS region is also obtained from in-situ measurements on board scheduled flights of passenger air craft with in the In-service Aircraft for a Global Observing System (IAGOS) project (*Zahn et al.*, 2014; *Petzold et al.*, 2015).

However, all in-situ measurements are confined by a limited spatial and/or temporal resolution. Satellite observations which are available since the late 1970s provide global coverage, higher temporal resolution and possibility of longer record. The Halogen Occultation Experiment (HALOE) on board NASA's Upper Air Research Satellite (UARS) measured a long water vapor time series from 1991 until 2005 with latitude coverage from 80°S to 80°N (*Harries et al.*, 1996). However, HALOE measurements in the early 1990s might be affected by the volcanic aerosol (*Fueglistaler et al.*, 2013). Aura Microwave Limb Sounder (MLS) has operated since middle of 2004 until now, which offers

high quality water vapor measurements retrieved from the thermally emitted microwave radiation from the Earth's limb (*Read et al.*, 2007). For the instruments measuring water vapor, accurate measurements of water vapor especially around the tropopause layer is of great difficulties because of the large span of water vapor values from the upper troposphere to the lower stratosphere and of extremely high variations of water vapor concentration associated with dynamical processes (*Kunz et al.*, 2013; *Hegglin et al.*, 2014). In the following, both HALOE and MLS water vapor observations will be used in comparison to CLaMS simulations of water vapor.

3.1.2 Variability of water vapor in the tropical lower stratosphere

The stratospheric water vapor entry values derived from almost three decades of satellite observations follow roughly the evolution of tropical tropopause temperatures (or cold point temperature, CPT) and show multi-timescale variations ranging from daily to decadal (*Fueglistaler and Haynes*, 2005; *Fueglistaler et al.*, 2013; *Urban et al.*, 2014; *Hegglin et al.*, 2014). The most pronounced signature of water vapor variations in the tropical lower stratosphere is the tape recorder effect (*Mote et al.*, 1996) reflecting the seasonal cycle of tropical tropopause temperatures. This annual cycle signal imprinted on the stratospheric water vapor mixing ratios at the tropical tropopause ascends with the BD circulation. In addition to this almost periodic component, transient, sub-seasonal cooling episodes occur at timescales of 1-2 months as a result of forcing by extratropical waves (*Randel et al.*, 2002). Beyond this, observations over the last several decades indicate also a strong interannual variability of lower stratospheric H_2O (*Oltmans et al.*, 2000b; *Hurst et al.*, 2011; *Kunz et al.*, 2013). The inter-annual variability is mainly influenced by the quasi-biennial oscillation (QBO, mean period of 28 to 29 months) (*Plumb and Bell*, 1982; *Baldwin et al.*, 2001; *Dessler et al.*, 2013) and to a weaker extent by the El Niño Southern Oscillation (ENSO) (*Randel et al.*, 2004b; *Gettelman et al.*, 2001; *Calvo et al.*, 2010).

On a decadal timescale, the significance of stratospheric water vapor trends recently received attentions because of its importance for climate change. Many studies discussed the stratospheric water vapor trend based on long-term observations, e.g. Boulder observation of water vapor (*Hurst et al.*, 2011; *Kunz et al.*, 2013), HALOE satellite data (*Randel et al.*, 2006; *Fueglistaler*, 2012) or several combined observations (*Rosenlof et al.*, 2001; *Fueglistaler and Haynes*, 2005; *Urban et al.*, 2014; *Hegglin et al.*, 2014). However, a consensus about the strato-

spheric water vapor trend is difficult to be reached. In fact, the more observations we include and the longer the observational record is available, the more uncertain we find the water vapor trend. *Oltmans et al.* (2000a) and *Rosenlof et al.* (2001) suggested that water vapor in the lower stratosphere may have increased by 1% per year in the second half of the 20th century based on balloon measurements, whereas *Hegglin et al.* (2014) found no significant trend using a series of measurements. Both satellite limb measurements by the Halogen Occultation Experiment (HALOE) and balloon-borne measurements over Boulder revealed a decrease in stratospheric water vapor since the end of 2000, consistent with a stronger tropical upwelling and lower temperatures in the TTL (*Randel et al.*, 2006; *Bönisch et al.*, 2011). Less than 30% of this increase could be explained by oxidation of increasing methane concentrations (*Rohs et al.*, 2006; *Riese et al.*, 2006). Moreover, with changes in the BD circulation and chemistry in the stratosphere, the of CH_4 oxidation in the stratosphere change, which has an impact on stratospheric water vapor trends (*Röckmann et al.*, 2004). Recently, *Urban et al.* (2014) analyzed the tropical water vapor in the lower stratosphere using a series of observations and reported another drop in water vapor observations by the Aura Microwave Limb Sounder (MLS) onboard the AURA satellite, that happened after 2012, sharing similarity with the earlier drop around 2000.

The variabilities of stratospheric water vapor and its impact factors are still open questions so far. However, there are few studies on stratospheric water vapor from the perspective of interaction between different timescales of variability. Especially, contribution from subseasonal variabilities to long-term trend or variabilities are usually neglected. However, this contribution is worth to study because: 1) the variability of stratospheric water vapor long-term record is obviously not a single linear trend but a result of non-linear multi-scale interaction; 2) we are able to understand the seasonal and subseasonal variabilities much better than the uncertain long-term trend or variabilities.

3.2 CLaMS tropical water vapor in the lower stratosphere

3.2.1 Model setup and validation

One of the difficulties in quantifying the variability of stratospheric water vapor arises from limitations of the observational systems, especially due to issues

arising from instrument drifts and short overlap periods. As recently discussed by *Hegglin et al.* (2014), chemistry-climate models nudged to observed meteorology have the potential to overcome these problems by providing a transfer function between different date set, which reconstructs a more homogeneous long-term data record.

We established a long-term water vapor data set from 1979 to 2013 using the Chemical Lagrangian Model of the Stratosphere (CLaMS) (*McKenna et al.*, 2002a; *Konopka et al.*, 2004; *Pommrich et al.*, 2014). Temperatures, horizontal winds and diabatic heating rates are prescribed from the ECMWF ERA-Interim reanalysis (*Dee et al.*, 2011). Methane oxidation is included as a source of water vapor in the middle and upper stratosphere, with the concentration of hydroxyl, atomic oxygen, and chlorine radicals taken from a model climatology (*Pommrich et al.*, 2014).

The lower boundary for the water vapor mixing ratio calculation is located at approximately 500 hPa and is set to the ERA-Interim water vapor field. The calculation of water vapor mixing ratios is based on a simplified dehydration scheme. If saturation (with respect to ice) occurs along a CLaMS air parcel trajectory, the water vapor amount in excess of the saturation mixing ratio is instantaneously transformed to the ice phase and sediments out, using a parameterization based on a mean ice particle radius and the corresponding fall speed (*Hobe et al.*, 2011; *Ploeger et al.*, 2013). Furthermore, if the parcel is subsaturated and ice exists, this ice is instantaneously evaporated until saturation is reached.

Figure 3.1 shows the tropical water vapor on 400 K from our simulation, HALOE and MLS satellite observations. We find a very good agreement between the simulation and the MLS measurements (purple line in Fig. 3.1). With the observations of the HALOE satellite (green line), the simulation shows also good agreement. The good agreement between HALOE observations and the simulation is better after 2000 than before. Before 2000, the relatively low simulated water vapor values compared with HALOE are consistent with a low bias of tropical tropopause temperature in ECMWF reanalysis data (*Dee et al.*, 2011), which has been corrected in 2006 after including new satellite data (COSMIC) into the 4d-var assimilation procedure (*Fueglistaler et al.*, 2013). Note that the water vapor drops in the tropics around 2000 and 2012, observable in the satellite data and also reflected in the CLaMS simulation.

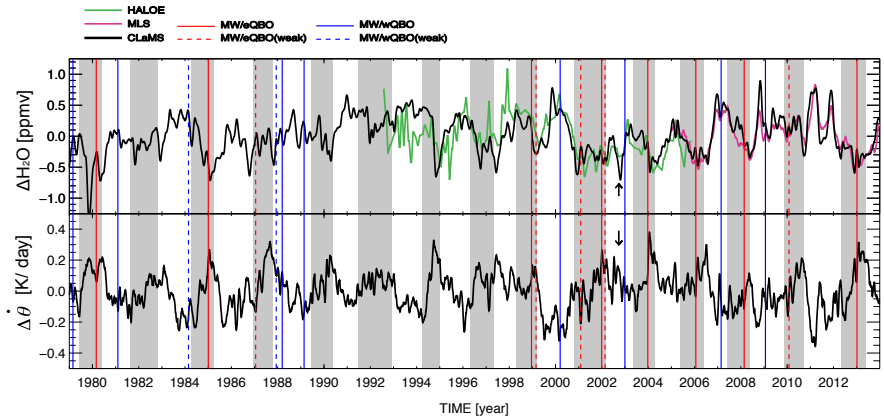

Figure 3.1: The evolution of water vapor volume mixing ratios (top) and the ERA-Interim diabatic vertical velocities $\dot{\theta}$ (bottom) in the tropics (10°S-10°N) at the 400 K potential temperature level ($\sim$18 km), shown as the deseasonalized anomaly with respect to the 35-year climatology. The black line shows the H_2O simulation from the CLaMS 35-year run; the green line shows HALOE; the purple line shows MLS satellite observations. A 15-day running mean is applied to all three data sets. The gray shadings highlight the QBO easterly phases (eQBO), which are defined by the ERA-Interim wind at 500 K (about 50hPa). The vertical straight lines mark the central days of SSWs: red during the eQBO, blue during the wQBO and dashed lines are major SSWs with a weak QBO (QBO index less than $\pm$ 5m/s). The black arrow shows the position of the only SSW in the southern hemisphere, which occurred in October 2002.

3.2.2 Possible impact factors

Following the statements in section 3.1, the stratospheric water vapor variability is controlled by the CPT which results from many factors and their non-linear interaction. The main factors associated with cold point temperature (CPT) variabilities include the large scale stratospheric circulation (*Gettelman and Birner*, 2007), the tropical zonal wind in the lower stratosphere (QBO phase) (*Plumb and Bell*, 1982; *Baldwin et al.*, 2001; *Dessler et al.*, 2013), tropical deep convection and its related tropical waves (e.g. Madden- Julian Oscillation) (*Virts and Wallace*, 2014) and sea surface temperature (e.g. ENSO) (*Randel et al.*, 2004b; *Gettelman et al.*, 2001; *Calvo et al.*, 2010). Here we will focus on the effect of major SSW events because the SSW, as a result of increased planetary wave activity is related to an acceleration of the BD circulation (*Holton et al.*, 1995). Hereby, the phenomenon of SSWs is not only a sudden temperature rise in the polar region but also a cooling in the tropics, which is expected to be reflected on the stratospheric water vapor entry values.

A glance at Fig. 3.1 meets our expectation. Here the CLaMS tropical zonal mean (10°S-10°N) deseasonalized water vapor is shown as a black line in the top panel, the diabatic vertical velocity $\dot{\theta}$ anomaly is shown as black line in bottom panel and the major SSWs are marked as the vertical straight lines (SSWs in the wQBO phase are colored in blue and those in the eQBO phase in red). Note that the major SSW events are identified using the methodology presented by *Charlton and Polvani* (2007) (CP07 from now on) based on ERA-Interim reanalysis. The corresponding central dates, the first day when zonal wind reversed at 60°N and 10 hPa, are listed in Table 3.1 (second column). As has been pointed out by *Taguchi* (2011) and *Gómez-Escolar et al.* (2014), use of the highest polar cap temperature instead of the zonal wind reversal at 60°N and 10 hPa, characterizes better the response of the BD circulation to SSWs. Thus, in our study the SSW central dates (Table 3.1 third column) are defined as the dates with highest mean polar cap temperature (60-90°N) within a $\pm$30 days window around each major SSW central date derived from the wind criterion (CP07). We notice that many of the water vapor drops follow the SSWs and the mean tropical upwelling $\dot{\theta}$ (Fig. 3.1 bottom) increases almost simultaneously. These characteristic drops in tropical water vapor usually happened 2-4 weeks after the central SSW days and, notably, all these H_2O drops approximately coincide with most of the lowest water vapor anomalies during the considered 35 years except for the 3 lowest values in the mid-1990s.

No.	SSWs/wQBO Central Date (Wind)	SSWs/wQBO Central Date (Temp.)	SSW magnitude ΔT_{10} (K)	ENSO index ΔSST (K)	MJO phase and amplitude
1	22 Feb 1979	27 Feb 1979	5.9	0.1	Ph.4/ **1.5**
2	4 Mar 1981	5 Feb 1981	13.7	−0.4	Ph.7/ 1.2
3	14 Mar 1988	12 Mar 1988	13.6	**0.7**	Ph.2/ **1.9**
4	21 Feb 1989	20 Feb 1989	12.3	**−1.4**	Ph.1/ 0.5
5	20 Mar 2000	13 Mar 2000	10.4	**−1.1**	Ph.5/ 0.8
6	18 Jan 2003	29 Dec 2002	13.1	**0.9**	Ph.4/ **2.2**
7	24 Feb 2007	24 Feb 2007	3.3	**0.6**	Ph.4/ **1.8**
8	24 Jan 2009	23 Jan 2009	14.4	**−0.7**	Ph.1/ 1.1
9	24 Feb 1984*	24 Feb 1984*	12.3	−0.3	Ph.8/ 0.9
10	8 Dec 1987*	8 Dec 1987*	12.1	**1.1**	Ph.3/ **1.8**
Avg.	21 Feb	15 Feb	10.8±4	−0.1±0.8	
No.	**SSWs/eQBO Central Date (Wind)**	**SSWs/eQBO Central Date (Temp.)**	**SSW magnitude ΔT_{10} (K)**	**ENSO index ΔSST (K)**	**MJO phase and amplitude**
1	1 Mar 1980	1 Mar 1980	14.2	0.4	Ph.3/ 0.5
2	1 Jan 1985	1 Jan 1985	12.5	**−1.0**	Ph.6/ 1.2
3	15 Dec 1998	17 Dec 1998	13.1	**−1.4**	Ph.6/ 0.8
4	30 Dec 2001	28 Dec 2001	16.0	−0.3	Ph.7/ **2.0**
5	5 Jan 2004	25 Dec 2003	12.5	0.4	Ph.6/ **2.4**
6	21 Jan 2006	21 Jan 2006	7.7	**−0.7**	Ph.5/ **2.6**
7	22 Feb 2008	23 Feb 2008	5.9	**−1.2**	Ph.1/ 0.8
8	6 Jan 2013	11 Jan 2013	11.6	−0.4	Ph.6/ **2.2**
9	23 Jan 1987*	18 Jan 1987*	7.7	**1.1**	Ph.3/ 0.4
10	26 Feb 1999*	27 Feb 1999*	12.5	**−1.1**	Ph.1/ 1.4
11	11 Feb 2001*	1 Feb 2001*	4.8	**−0.6**	Ph.3/ **1.8**
12	17 Feb 2002*	19 Feb 2002*	4.0	-0.1	Ph.5/ **1.5**
13	9 Feb 2010*	30 Jan 2010*	11.4	**1.2**	Ph.7/ **2.0**
Avg.	16 Jan	16 Jan	11.7±3	−0.5±0.7	

Table 3.1: Central dates of the SSWs in eQBO (top) and wQBO (bottom) phase. The second column shows the central dates according to the wind reversal criterion of *Charlton and Polvani* (2007). The third column shows the central dates according to the maximum polar cap temperature (*Taguchi*, 2011). The QBO phase is defined by 30-day smoothed equatorial mean wind at $\theta = 500$ K (∼50hPa). The central dates marked with stars are the major SSWs within the transition regime between two QBO phases. The magnitudes of SSWs in the forth column are estimated from the polar cap (50°N - 90°N) temperature anomaly at 10 hPa averaged over ± 5 days around the temperature-based central date. The fifth column shows Oceanic Niño Index estimated by 3-month (DJF) running mean of ERSST.v4 sea surface temperature (SST) anomalies in the Niño 3.4 region (5°N-5°S, 120°-170°W) and the bold numbers are those above the threshold of ± 1 K. The MJO phases and amplitudes are from the Australia Bureau of Meteorology and are based on a combined Empirical Orthogonal Function analysis using fields of near-equatorially averaged (15°S-15°N) 850 hPa and 200 hPa zonal wind and OLR (*Wheeler and Hendon*, 2004).

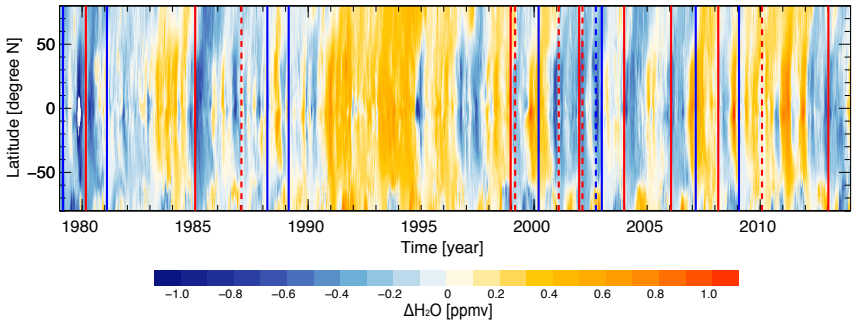

Figure 3.2: The distribution of zonal mean water vapor volume mixing ratios at the 400 K potential temperature level (∼18 km), shown as the deseasonalized anomaly with respect to the 35-year climatology. The vertical straight lines mark the central days of SSWs as Figure 3.1.

Furthermore, we extend Fig. 3.1 to the distribution of zonal mean H_2O along latitudes at $\theta = 400$ K as shown in Figure 3.2. The SSWs central dates are also marked in the same way in Fig. 3.1. Clearly, the water vapor drops that follow the SSWs are not confined within the tropics but extend to middle and even high latitudes. The extension of water vapor drops to 30-40°N is rapid because it occurs though (fast) isentropic mixing processes. The propagation of negative water vapor amonalies to high latitudes takes usually more than half a year and hemispherically asymmetric structure. The development of this hemispheric asymmetry varies from one case to another and thus will not be investigated further in this study.

Gómez-Escolar et al. (2014) pointed out that the enhanced tropical cooling in the lower stratosphere related to SSWs is strongly modulated by the QBO phases. Thus, we consider the QBO phases during SSWs in the following analysis. The QBO phase for each SSW is defined using the 30 day smoothed equatorial mean wind at $\theta = 500$ K (approximately 50 hPa) calculated for each temperature-based central date. Major SSWs with equatorial mean wind at 500 K less than ± 5 m/s have occurred in the transition regime between two QBO phases and therefore can not be attributed clearly to a QBO phase. These SSWs are excluded in the

following statistical analysis (the corresponding central dates are marked with stars in Table 3.1). February 21st and January 16th are the average SSW central dates in eQBO and in wQBO phase respectively. These two dates will be used in the following statistical analysis as the central dates for the years without occurrence of major SSWs in the corresponding QBO phases.

In addition to the factors contributing to the zonally symmetric variations of water vapor anomalies (e.g. BD circulation intensity and QBO), the factors associated with zonally asymmetric variability (mainly ENSO and MJO) should also be considered. *Randel et al.* (2009) pointed out El Niño (La Niña) events could induce warming (cooling) of the TTL and cooling (warming) of the tropical lower stratosphere. *Calvo et al.* (2010) connected El Niño events with an enhancement of the BD circulation and a drying in the tropical lower stratosphere. Here we listed the ENSO index for each winter (3-month mean refer to the SSW central date) with occurrence of SSWs in the fifth column of Table3.1. The ENSO index is the Oceanic Niño Index (ONI) based on the three-month running-mean sea surface temperature (SST) departures from average in the Niño -3.4 region of the equatorial Pacific Ocean (5°N-5°S, 170°W-120°W). An ONI index larger than 0.5 indicates an El Niño event and an ONI index smaller than -0.5 indicates a La Niña event. We find the cold and warm ENSO phases during the winters with SSWs are almost equal: 9 La Niña winters against 7 El Niño winters out of 23 winters in total. This result is consistent with the study by *Butler and Polvani* (2011) showing that the frequency of SSWs during each ENSO phase is almost equal. *Butler and Polvani* (2011) also stated that the SSWs are more frequent during ENSO winters than during ENSO-neutral winters. Therefore, we speculate that the both ENSO phases potentially enhance the extratropical planetary waves and their propagation into the stratosphere.

The Madden- Julian oscillation (MJO) is the most prominent mode of subseasonal ($\approx$30-60 day) variability in the tropics (*Madden and Julian*, 1972). It is associated with an enhanced convective signal slowly moving eastward ($\approx 5\text{ms}^{-1}$) over the tropics. It has been suggested that the subseasonal variabilities of temperature and the wind field in the UTLS are influenced by the MJO and its related Kelvin waves (*Kiladis et al.*, 2001; *Randel and Wu*, 2005). In addition, studies suggested that the SSWs tend to follow certain MJO phases due to the teleconnections between MJO and the sea surface temperature in the North Pacific (*Garfinkel et al.*, 2012; *Liu et al.*, 2014). We use the daily multivariate MJO index that is described in *Wheeler and Hendon* (2004). The eight MJO phases

indicate the location of the convectively active region: phases 2-4 corresponding to the Indian Ocean and the western Maritime Continent and phases 5-7 to the eastern Maritime Continent and the western Pacific Ocean. The MJO is considered as being active when the amplitude of the MJO index exceeds 1.5. Our result shows that about half of the winters with SSWs (12 out of 23 winters) are accompanied by active MJO (amplitude larger than 1.5). However, no particular MJO phases favor the onset of SSWs according to the last column of Table3.1.

It is possible that the large-scale waves triggered by tropical deep convection, which are related to MJO or ENSO, extend to the tropopause layer and influence the CPT. Another possibility is that ENSO- or MJO- related tropical anomalies enhance the planetary waves in the troposphere and the increased wave-propagation disturbs the polar vortex, which accelerates the tropical upwelling. Because each boreal winter experienced a different evolution of MJO and ENSO, either of the possibility is hard to prove. We can not completely exclude the influence of ENSO or MJO on the stratospheric water variabilities in the following analysis. However, the ENSO pattern or MJO related convection by themselves cannot explain the zonally averaged temperature and water vapor variabilities in the TTL. Focussing on a view of the whole tropical stratosphere, the zonally symmetric factors, e.g. large scale stratospheric circulation and QBO, are dominant and the contribution of ENSO or MJO is of secondary order (*Gettelman et al.*, 2001; *Fueglistaler and Haynes*, 2005).

3.3 SSW effect

3.3.1 The tape recorder signal and QBO

Figure 3.3 provides the vertical structure of the tape recorder as observed by MLS (a) and simulated with CLaMS (b). The figure shows tropical zonal mean water vapor (10°S-10°N) with the time axis confined to boreal winter (DJF). We focus on boreal winter, because the major SSWs all happened in the northern hemisphere with the exception of one in the southern hemisphere in October 2002 (black arrow in Fig. 3.1; this SSW will be excluded from the further discussion). A good agreement is achieved in terms of mean vertical structure and the slow upward phase propagation. However, the layer with the lowest water vapor mixing ratios around the tropopause is located $\sim$10 K higher in the CLaMS simulation than in the MLS observations (Fig. 3.3 (a-b)). Furthermore, a faster

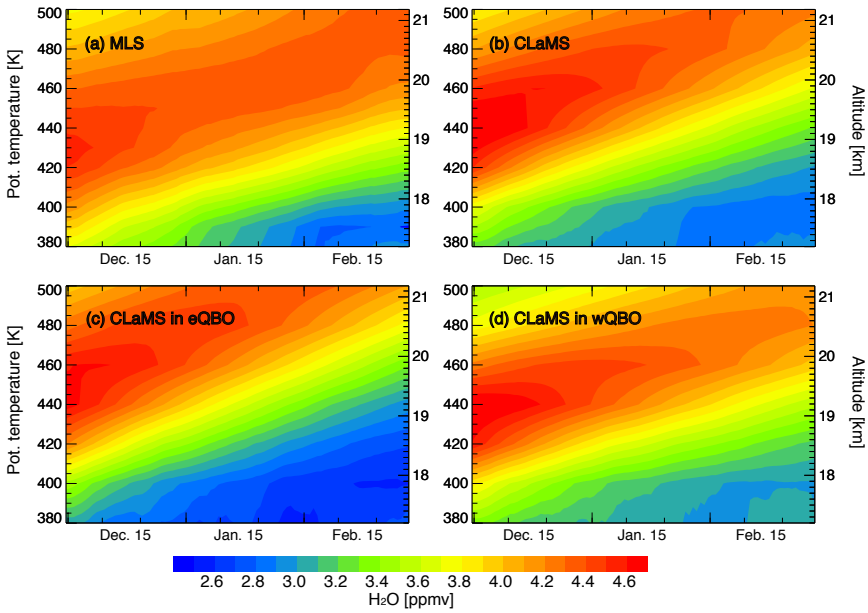

Figure 3.3: Tropical water vapor climatology (10°S-10°N, 2005-2013) during boreal winter (DJF) for (a) MLS observations and (b) CLaMS simulation. The same is shown for: (c) eQBO phase composites and (d) wQBO phase composites, from CLaMS. Note that the averaging kernels of MLS are applied to the CLaMS simulation (b) for better comparison.

upward propagation of the tape recorder signal is found above 430 K in CLaMS simulations. This excessive tropical upwelling is consistent with the temperature low bias in the ERA-Interim forecast (*Dee et al.*, 2011), which has also been found in CLaMS simulation of the CO tape recorder (*Pommrich et al.*, 2014)

To quantify the effect of the QBO phase on the amount of water vapor entering the stratosphere, the vertical structure of the tape recorder derived from a 35-year CLaMS climatology is divided into two composites containing either years with eQBO or with wQBO phase (Fig. 3.3c and d). In the 35 years, there are 18 boreal winters with wQBO phase and 15 winters with eQBO phase. Note that both the MLS and HALOE data sets are too short to make this type of analysis statistically significant. Similar as in Fig. 3.3a and b, the tape recorder signal is seen in both QBO phases. However, obvious differences related to the QBO phase exist: First, the H_2O minimum between 380 and 420 K, resulting from intensive dehydration at the tropical tropopause during winter, is by $\sim$0.5 ppmv lower during the eQBO than during the wQBO phase. Second, the tropical upwelling as represented in the H_2O tape recorder is faster for the eQBO years than for the wQBO years. All these impacts of the QBO phase on the tropical H_2O are consistent with previous studies (see e.g. *Baldwin et al.*, 2001).

3.3.2 Net effect of major SSWs

Because the annual cycle is the dominant feature of water vapor entering the tropical stratosphere, we consider in the following deseasonalized anomalies (i.e. relative to the 35-year mean) of H_2O and temperature. Besides, we categorize the eQBO (wQBO) winters into eQBO (wQBO) winters with and without occurrence of major SSWs (eQBO/MW, wQBO/MW, eQBO/noMW and wQBO/noMW). The composites of the deseasonalized anomalies of H_2O (colored) and temperature (gray contours) according to these categories are shown in Figure 3.4 (a1, eQBO/noMW; a2, wQBO/noMW; b1, eQBO/MW; b2, wQBO/MW). For years with major SSWs, $\pm$90 days periods around each SSW central date (as shown in Table 1) are used for the composites. Note that the mean central date of wQBO/MW (15 February) is one month later than that of eQBO/MW (16 January). Considering the time shift of SSW relative to the QBO phase, the composite for eQBO/noMW (wQBO/noMW) cases is centered at January 16th (February 15th) with a $\pm$90-day window. To separate the SSW effect from the QBO variability, we composite the differences between eQBO/MW(Fig. 3.4(b1)) and eQBO/noMW (Fig. 3.4(a1)) as shown in

Fig. 3.4 (c1) that estimates the SSW net effect in the eQBO phase (analogously for wQBO in Fig. 3.4(c2)).

First, the eQBO case is colder ($\sim$ 1.5 K) and drier ($\sim$ 0.5 ppmv) in the lower stratosphere compared with the wQBO case, independent of the major SSW occurrence (c.f. Fig. 3.4(a1) with (a2) for winters without SSW and Fig. 3.4(b1) with (b2) for winters with SSW). Beyond the upward-propagating anomaly branch starting in early winter (white arrows), a fast upward propagating branch with low H_2O anomaly values (green arrows) can be diagnosed in both QBO phases during SSW (Fig. 3.4(b1) and (b2)). The upward-propagating low H_2O anomaly can be better seen if it is separated from the QBO variability (Fig. 3.4(c1) and (c2)). These sub-seasonal signatures start at $\theta = 380$ K about 15-30 days after the (mean) central day and propagate up to 480 and 420 K in the eQBO and wQBO phase in the following 1-2 months. Furthermore, both of these sub-seasonal negative H_2O anomalies are accompanied by drops of the tropical temperature (gray dashed contours). However, the tropical cooling in the eQBO is strongest (up to 2 K anomaly) at 430 K about 15 days after the SSW onset and reduces the tropopause temperature by approximately 1 K. The cooling for wQBO/MW (Fig. 3.4(c2)) weakens below about 450 K and the negative temperature anomaly almost disappears when reaching the tropical tropopause. This asymmetric response of tropical temperature relative to the QBO phase is consistent with the results discussed by *Gómez-Escolar et al.* (2014) (see also next section).

It is shown in Fig. 3.4(c1) and (c2) that H_2O differences are below 0.2 ppmv and without statistical significance before the SSW central date. The direct dehydration following the SSWs (after the central date) is evident for both QBO phases (green arrows in (c1) and (c2)). There is a drop of water vapor (0.2- 0.3 ppmv) around the tropopause 15-30 days after the SSW central day, which results from TTL cooling after the SSW onset, shown by the temperature differences (gray contours) due to SSWs in Fig. 3.4(c1) and (c2). Both responses pass the Monte Carlo difference test (see supplement) at 0.9 confidence level (crosses). The anomalies propagate upwards and strengthen by $\sim$1 ppmv. The enhancement of upward-propagating anomalies are related to the dilution rate of tropical air by middle latitude air through horizontal transport (termed in-mixing) that is of importance to the water vapor tape recorder in the lower stratosphere (*Mote et al.*, 1998). The ascending anomaly increases more strongly (and steeper) during eQBO. It is mainly because of the faster upward transport and consequently

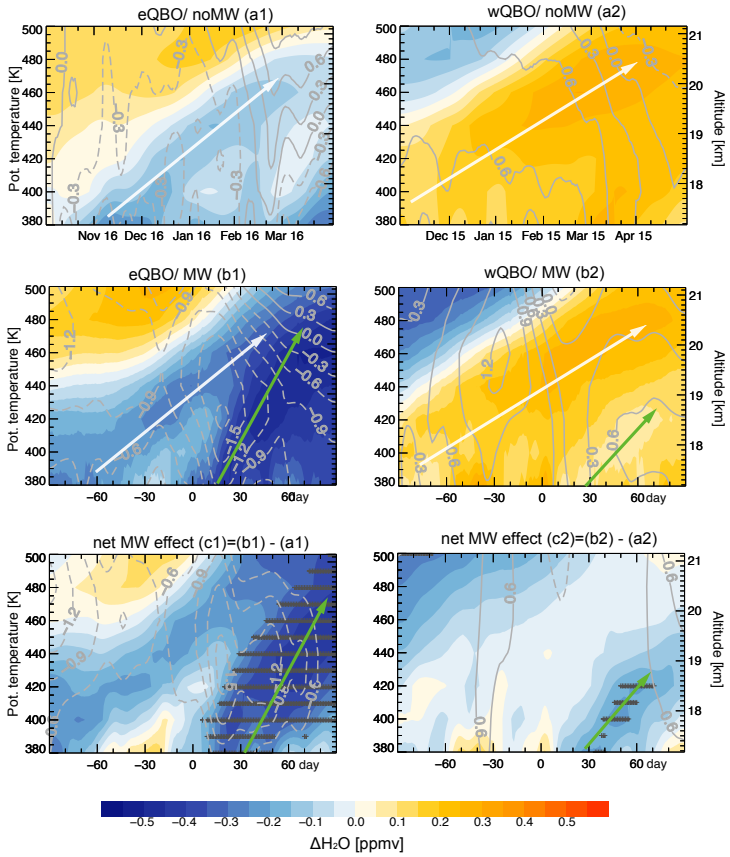

Figure 3.4: Composites of CLaMS tropical (10°S-10°N) deseasonalized anomaly for water vapor (colored) and temperature (gray contours, solid/dashed for positive/negative values) for eQBO (left column) and wQBO composites (right column). In the first row (a1/ a2) all the boreal winters without SSWs are shown. In the middle row (b1/ b2) the winters with SSWs within a ±90 days window around each SSW are collected. In the bottom row, the respective differences, i.e. (b1)-(c1) and (b2)-(c2), show the net effect of the SSWs during the eQBO and wQBO, respectively. Note that in years without a SSW event, the mean central dates of MW/eQBO (Jan 16) and MW/wQBO (Feb 15) cases are used. Crosses denote ΔH_2O results with statistical confidence above 0.9 (Monte Carlo difference test).

less in-mixing from middle latitude air during the easterly phase.

Another important difference is related to the QBO phase: The SSW-related cooling and subsequent dehydration during the eQBO phase can be well separated from the change of the background and contribute to about $\sim$0.3 ppmv H_2O drop about 2-4 weeks after the central date of the SSW. On the other hand, a much smaller decrease of H_2O relative to the background about $\sim$0.1 ppmv can be diagnosed during the wQBO phase. Note that the mean strength of SSWs in two QBO phases does not differ much, less than 10% (see the 4th column of Table 1). Therefore, the strength of SSWs in different QBO phases can not explain the different responses of tropical water vapor to SSW.

In a recently published study, *Evan et al.* (2015) investigated extreme low temperature and water vapor by in-situ measurements during the Airborne Tropical TRopopause Experiment (ATTREX) in winter 2013. The local temperature drop reached up to 2 K and the decrease of water vapor up to 1.5 ppmv at 82 hPa based on the in-situ measurements. Consistent with our analysis based on the CLaMS simulation, *Evan et al.* (2015) attributed the extreme low water vapor to the response to the major SSW modulated by the eQBO during that period.

3.3.3 SSWs, BDC and the QBO-dependent dynamical background

The extratropical planetary waves in the stratosphere intensify during the weeks directly preceding the SSWs (*Limpasuvan et al.*, 2004). The intensified waves lead to upper-stratospheric wave breaking, which triggers the SSWs and accelerates the deep branch of the BDC (e.g. *Holton et al.*, 1995). The enhanced wave breaking results in enhanced polar downwelling, enhanced tropical upwelling and increased cooling in the tropical stratosphere. The wave forcing during SSWs intensifies not only in high latitudes but also in the subtropical lower stratosphere. The related subtropical wave driving can be a result of modified wave-propogation conditions (lower-stratospheric zonal mean wind) (*Garcia and Randel*, 2008) or because waves are generated by deep convection in the tropics and subtropics (*Kerr-Munslow and Norton*, 2006; *Norton*, 2006; *Chen and Sun*, 2011).

Gómez-Escolar et al. (2014) pointed out that the response of tropical temperature to SSW is strongly modulated by the QBO. Figure 3.5 shows a diagram of this mechanism (Figure 8 from *Gómez-Escolar et al.*, 2014). At altitudes above $\sim$40 hPa, tropical temperature anomalies associated with SSWs persist longer during the westerly QBO phase (wQBO) than during the easterly QBO phase

(eQBO). The wave breaking at low latitudes is modulated by the QBO related zero-wind line (the transition layer between the QBO westerlies and easterlies). During the eQBO phase, the zero-wind line is much lower (around 30 hPa) than during wQBO phase (around 10 hPa). Hence, the low-latitude wave breaking occurs at lower levels during eQBO winters and efficiently accelerates the shallow branch of the BDC (*Garny et al.*, 2011; *Gómez-Escolar et al.*, 2014).

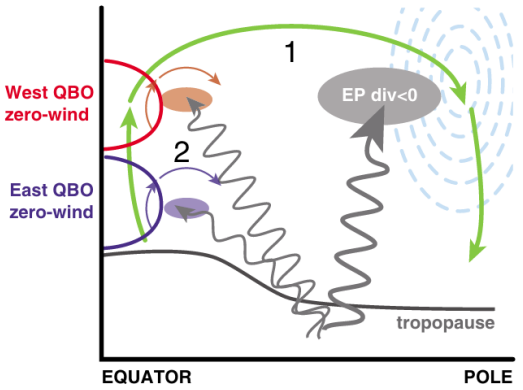

Figure 3.5: Scheme of the mechanisms for tropical stratospheric cooling associated with a SSW occurrence. The tropical region is affected by two pathways: (1) the increased circulation is associated with enhanced wave driving and (2) the subtropical wave dissipation controlled by the position of the zero- wind line which in turn is modified by the QBO phase. Figure adapted from *Gómez-Escolar et al.* (2014)

Therefore, drops of tropical temperature in the lower stratosphere are expected during winters with SSWs in both QBO phases, due to an accelerated deep branch of the BDC and intensified tropical upwelling. However, the SSW-induced sub-seasonal temperature variability in the TTL is modulated by the QBO-dependent zero wind line and, consequently, extends to lower levels in the eQBO than in the wQBO winters (see gray contours in Fig. 3.4(b1/b2)). When a SSW happens in a wQBO winter, temperature variations occur mainly above 440 K and do not significantly influence the stratospheric water vapor entry values. However, in an eQBO winter, the tropical response from the shallow branch of the BDC occurs at lower altitudes, close to the tropopause and thus more likely

drives an extra-dehydration at the tropical tropopause 10-30 days after the SSW event.

3.4 Potential contribution of SSWs to water vapor trend

In the previous section, we have discussed the impact of SSWs on tropical H_2O in the lower stratosphere and its relation to the QBO phase. The mean lower stratospheric H_2O decrease is $\sim$0.2 ppmv during 1-2 months after a SSW. Although the influence of the SSWs on tropical H_2O is confined to the sub-seasonal timescale, the resulting H_2O decrease may contribute to a long-term H_2O change when the frequency of SSWs in the recent 2-3 decades is taken into account. An interesting fact is that SSWs are relatively rare in the 1990s and have become more frequent after 2000 (see Table 3.1): only 2 events happened in the 1990s but 11 events in the 2000s. Thus, this significant increase in the frequency of the SSWs after 2000 may have affected the decadal variability of tropical H_2O.

To illustrate the change of tropical H_2O around 2000, we calculate the difference of H_2O before and after 2000 and plot the results in Fig. 3.6. Here we count the winter of 1999/2000 into 2000s and exclude the winter of 2009/2010 to avoid a sampling-bias due to asymmetric contributions of the QBO phases. Hence, 5 eQBO and 5 wQBO winters are counted before and after 2000. Again, we use the same method as discussed in the last section to remove the seasonality from the H_2O signal.

Figure 3.6 shows an overall drier lower stratosphere in the winters and springs of 2000s than in the 1990s accompanied by enhanced cooling especially after mid-January. Two characteristic and statistically significant patterns (confidence larger than 0.9 overlaid by crosses) can be diagnosed in the stratospheric H_2O decadal difference: the slowly ascending, tape recorder pattern and a fast ascending branch with negative values of 0.2 ppmv. The first pattern is the anomaly due to lower tropical temperature caused by enhanced upwelling in 2000s as discussed in *Randel et al.* (2006) that is also related to an increased number of SSWs during this period. The second, fast ascending contribution in February, March and April is very similar to the pattern of the time evolution of H_2O due to the SSWs discussed in the previous section (Fig. 3.4). Hence, the dryer lower stratosphere after 2000 appears to be related to the dehydration effect of SSWs.

Figure. 3.7 shows the same plot as Fig. 3.6 but extended to the whole year. It is obvious that tropical air is significant drier in the1980s and the 2000s than that

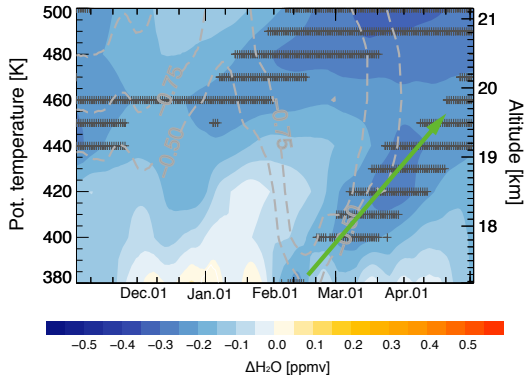

Figure 3.6: Differences of tropical (10°S-10°N) water vapor (colored) and temperature (gray contours) deseasonalized anomalies derived from the 35-year CLaMS simulation between winters in 2000s and winters in 1990s (2000s minus 1990s). Gray crosses indicate statistical confidence larger than 0.9 as derived from the Monte Carlo test.

in 1990s. This is consistent with previous studies of stratospheric water vapor trends (*Randel et al.*, 2006; *Fueglistaler*, 2012) and is, at the same time, connected to the SSW-occurrences in these three decades: 8 major SSWs in 1980s and 11 events in 2000s but only 1 event in 1990s. Similar in both figures are the two ascending drying anomalies (with respect to 1990s), originally starting in boreal winter (green arrows) and boreal summer (red arrows) respectively. The first one starting in boreal winter (green arrows) is related to SSWs and is the main focus of out study. The second one starting in summer (red arrows) shows a strong contribution during 1980s. Although the summer ascending anomaly undoubtedly contributes to the long-term variability of stratospheric water vapor, its reasons stay unclear and need further investigation.

The winter anomalies in both figures (3.6 and 3.7) started in late February and early March. This is just the time period of high frequency of major SSWs in these two decades. Furthermore, the amplitude and duration of wintertime ascending drying anomalies are both remarkable. The drying anomalies reached the maximum of 0.3 ppmv and lasted for 4-5 months with a relative fast upwelling. To emphasize this point, we averaged H_2O in the tropical lower stratosphere (400 K) from February to April every year and ploted these H_2O values

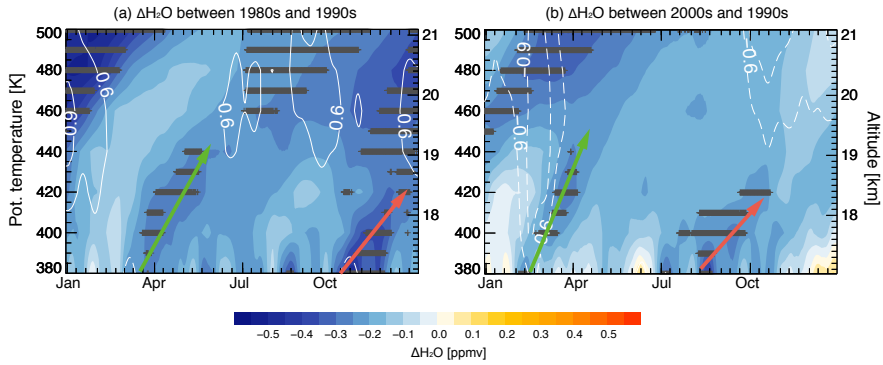

Figure 3.7: Decadal differences of tropical (10°S-10°N) water vapor (colored) and temperature (white contours) deseasonalized anomalies derived from the 35-year CLaMS simulation. Differences between following decadals are shown: (a) winters in 2000s and winters in 1990s (2000s minus 1990s); (b) winters in 1980s and winters in 1990s (1980s minus 1990s). Gray crosses indicate statistical confidence larger than 0.9 as derived from the Monte Carlo test. Green arrows indicate the asscending anomalies starting at boreal winter while red arrows show that starting from summer.

together with the decadal frequency of SSWs (Figure 3.8). Figure 3.8 shows a remarkable anti-correlation between the SSW-occurrences and the H_2O values in the three decades.

3.5 Discussion and remarks

Dehydration of air entering the tropical stratosphere was clearly diagnosed after SSWs. The related tape recorder pattern starts at the tropical tropopause and propagates upward in both QBO phases during the following 2-3 months. The enhanced breaking of planetary waves in the subtropical lower stratosphere during eQBO phase results in a distinct cooling and a subsequent drying at the trop-

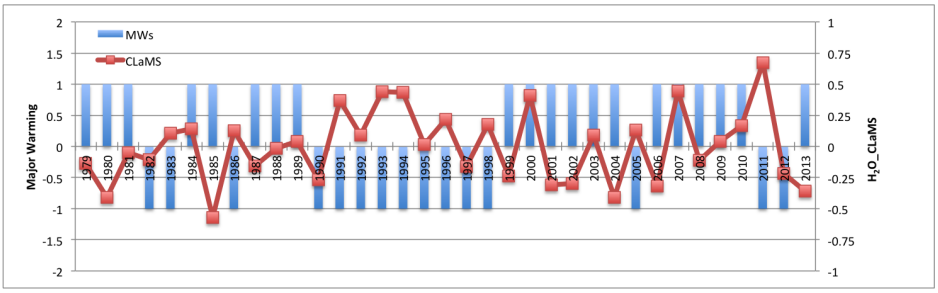

Figure 3.8: The bar chart shows the record of major SSWs from 1979 to 2013: winters with SSWs are valued 1 and winters without SSWs are values -1. The scatter-line shows the mean water vapor mixing ratio (400 K, 10°N-10°S, unit: ppmv) of February, March and April using the CLaMS simulation.

ical tropopause by ∼0.3 ppmv around 3 weeks after the SSW. In the wQBO phase this drying effect is also present, but smaller and more uniformly distributed over time. Moreover, the SSW-induced tropical upwelling is stronger in the eQBO than in the wQBO phase and results in a faster upward transport of the dehydrated air masses.

Since the sharp and unexpected drop (∼0.4 ppmv) in stratospheric water vapor after 2000 was documented (*Randel et al.*, 2006), a number of studies tried to explain this drop in different aspects: drop of tropical temperature in relation to strengthened BD circulation (*Randel et al.*, 2006; *Bönisch et al.*, 2011) and sea surface temperature (SST) increases in the tropical warm pool (*Rosenlof and Reid*, 2008). In our study, an extra-dehydration in relation to SSW was clearly diagnosed, related to the a decadal variability in the frequency of major SSWs. The results support the study by *Randel et al.* (2006) and *Bönisch et al.* (2011) that long-term water vapor variabilities in TTL is mainly a result of the variabilities of the cold point temperature. In addition, extra-dehydration due to SSWs (less in-mixing from higher latitudes due to faster upwelling), can last longer than 4 months, that at the same time propagates upwards, although the SSW itself is confined to boreal winter. Therefore, we looked into 10-year differences of H_2O anomalies in Figure 3.6 and found a similarity of H_2O decadal difference and the SSW-associated drying effect (Fig. 3.4). The similar pattern in H_2O differences between 1980s (8 major SSWs) and 1990s (1 major SSW) further

supports our main hypothesis: the SSW-associated drying effect possibly has a contribution to the long-term variability of stratospheric H_2O. The quantification of various contributions to the variability of stratospheric H_2O needs further investigation (e.g. the full-dynamic control simulation without SSWs).

Chapter 4

Improvement of mixing parameterization

4.1 Motivation

First, we recall the physical idea behind the mixing scheme in CLaMS. We are trying to find a mechanism that allows regions to be identified where mixing happens on the scale resolved by the model. Typically, such regions are often related to atmospheric instabilities like the formation of deep convection. In the first chapter, the Richardson number was introduced to quantify instabilities, which are associated with wind shear and the static stability (N^2). Due to high static stability in the stratosphere, only sufficiently strong deformations of the horizontal wind are excepted to drive mixing within a considered stratospheric layer. Since most applications of CLaMS in the past were focused on the stratosphere, the mixing in the current version of CLaMS is induced by sufficiently strong vertical and horizontal shear rates of mostly isentropic wind (diagnosed within each model layer).

The Brunt-Väisälä frequency N^2 is a key parameter to describe the atmospheric stability. Figure 4.1 shows the climatology of the zonal mean (dry) Brunt-Väisälä frequency N^2 for winter (DJF) and summer (January). Clearly, N^2 is much higher in the stratosphere than in the troposphere. The high static stability (N^2) is located above the tropical and extratropical tropopause and the maximum N occurs in the tropical lower stratosphere (often denoted as the Tropopause Inversion Layer (*Birner et al.*, 2006)), which becomes obvious when

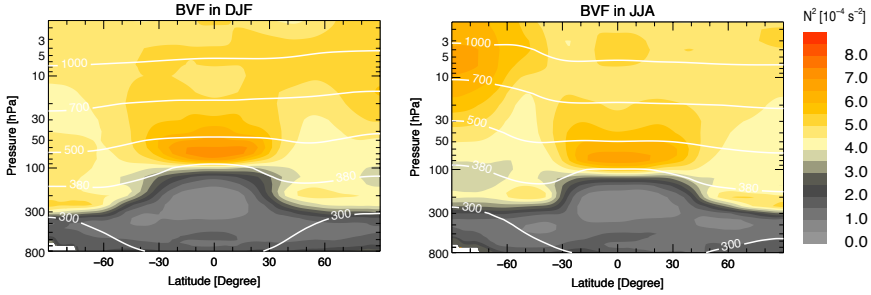

Figure 4.1: Zonally averaged squared Brunt-Väisälä frequency N^2 for winter (DJF) and summer (JJA). The Brunt-Väisälä Frequency (N) is based on ECMWF ERA-interim reanalysis for the year 2008. The white lines are potential temperature levels.

N^2 is plotted in the tropopause-relative vertical coordinate (*Grise et al.*, 2010). The high N^2 in the stratosphere is a result of the temperature rise with altitude above the tropopause. The troposphere is characterized by much weaker stability compared with the stably stratified stratosphere. The minimum of N^2 is found in the tropical upper troposphere and extends to the extratropical troposphere in the summer hemisphere. The transition layer from the troposphere to the stratosphere (the UTLS region) is marked by a sharp gradients of N^2 and the highest gradient is found above the tropical tropopause.

Weak static stability is found in the troposphere, especially in the tropics. When the static stability N^2 becomes small, tropospheric mixing is expected in the weakly stratified regions. Furthermore, the weak static stability favors convective process which can effectively drive convective mixing. As a result, the convective mixing is expected to influence the distributions of tracers in the upper troposphere and even in the lower stratosphere (e.g., *Gidel*, 1983; *Dickerson et al.*, 1987; *Gray*, 2003; *Hegglin et al.*, 2004).

Here we use the multi-annual, global CLaMS simulations of the whole troposphere and stratosphere. We use high quality in-situ measurements of CO (*Volk*

et al., 2000; *Homan et al.*, 2010; *Viciani et al.*, 2008) and ozone (*Yushkov et al.*, 1982) with high spatial vertical resolution to compare with the simulation. CO is a tropospheric tracer and its lifetime ($\sim$3 months) is long enough for tracking the transport from the troposphere to the stratosphere. Ozone is a long-lived tracer in the lower stratosphere and the high concentration of ozone marks the air mass of stratospheric origin. Therefore, CO and ozone will be used as tropospheric and stratospheric tracers respectively.

CO is prescribed in CLaMS at model levels at and below ζ= 200 K (i.e. below about 4 km) by using the satellite-based observations with the highest vertical sensitivity around 500 hPa measurements of pollution in the troposphere (MOPITT) (*Pommrich et al.*, 2014). Because of sampling and smoothing processes, CO is underestimated by MOPITT in the boundary layer and the lower troposphere. In order to correct this underestimation, CO values in the lower boundary, i.e. the orography-following model layer below $\zeta = 200$ K, are scaled up by an adjustable factor in the CLaMS simulation. The factor is adjusted to particular research purpose and this scale factor is set to two in the simulation. The concentration of ozone at the surface is set to zero and and ozone is prescribed from the HALOE climatology above $\theta = 500$ K. A simplified chemistry scheme is applied in the CLaMS simulation. More details about the chemistry scheme and boundary conditions is discussed in *Pommrich et al.* (2014).

Figure 4.2 shows the CLaMS simulation and in-situ measurement of CO and O_3 based on one flight over Sao Paulo state in Brazil on 4 February 2005 during the Tropical Convection, Cirrus and Nitrogen Oxides (TROCCINOX) campaign. The Geophysica aircraft intercepted a severe convective event on 4 February 2005. A strong uplift of young air masses and brightness temperature (BT) lower than 190 K were observed during the flight (*Chaboureau et al.*, 2007). Therefore, these measurements are a good example to test the representation of deep convection in the CLaMS simulation. The figure (top left panel) shows that the CLaMS CO is underestimated compared with both the in-situ CO values from both the COLD measurement (*Viciani et al.*, 2008) and HAGAR measurement (*Volk et al.*, 2000; *Homan et al.*, 2010). Because it is shown that CO from HAGAR measurements tend to be lower than the COLD CO measurements, the underestimation from CLaMS simulation is more significant compared to COLD measurements than compared to HAGAR measurements. A clear difference between the observations and simulation can be diagnosed between 340 K and 360 K where enhanced CO associated with the convective uplift was observed. Moreover, the

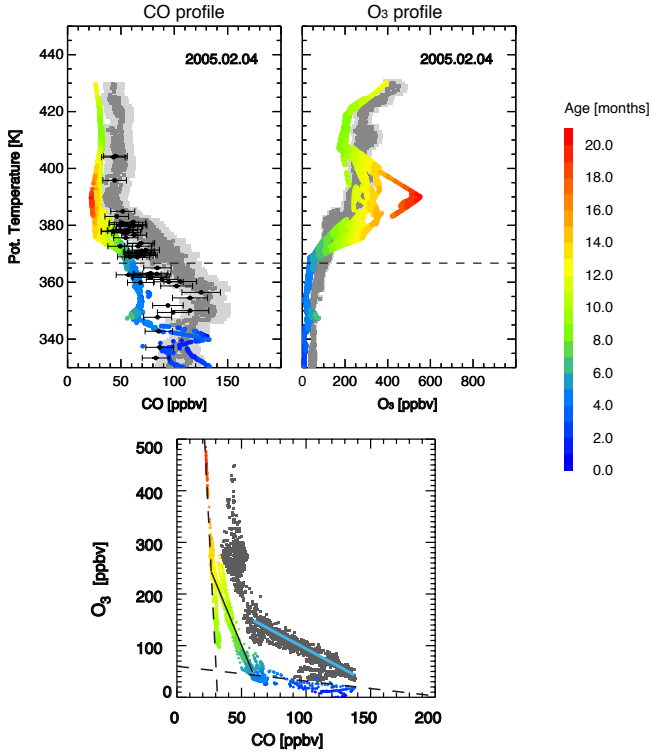

Figure 4.2: The comparison between simulation of CO from CLaMS (colored) with the in-situ measurements from COLD (dark grey) and from the HAGAR instrument (black) on the Geophysica aircraft on 4 February 2005 during the Tropical Convection, Cirrus and Nitrogen Oxides (TROCCINOX) campaign. Top two panels show the CO and O_3 profiles and the black dashed lines show the tropopause derived from the corresponding in-situ temperature measurements. The bottom panel shows the corresponding O_3-CO correlation. The mean age of air calculated with CLaMS is color-coded in the unit of months. The total measurement uncertainty is shown for both instruments (light grey shading for COLD and black error bars for HAGAR). Total measurement uncertainty is determined as the square root of the sum of squares of the accuracy and precision of the measurements.

difference between the simulation and COLD measurement is also clear between 360 K and 390 K but the difference between the simulation and HAGAR measurement is within the instrument uncertainty.

The simulated O_3 (top right panel) values between 370 K and 400 K are overestimated compared to the O_3 from the FOZAN measurement (*Yushkov et al.*, 1982). The simulation shows an aged stratospheric air mass intrusion with high ozone and low CO value around 390 K, which is inconsistent with the O_3 measurements. The overestimation of O_3 with CLaMS can result from the missing chemistry of O_3 loss in the stratosphere in the CLaMS run. It can also be caused by insufficient representation of convective uplift and mixing, which possibly decreases the O_3 concentration and increases the CO values in the lower stratosphere.

Next we consider the correlations between the stratospheric tracer O_3 and tropospheric tracer CO (O_3-CO correlation) shown in Figure 4.2. A series of previous studies have used O_3-CO correlations based on in-situ measurements to identify the exchange between the stratosphere and troposphere in the UTLS region. (*Hoor et al.*, 2002; *Pan et al.*, 2004, 2007; *Kunz et al.*, 2009). The idealized 'L shape' in O_3-CO correlation space without mixing is composed of two quasi-linear correlation branches. The stratospheric branch is characterized by compact low CO values and high variable O_3 values whereas the tropospheric branch shows the opposite behavior. The mixing process between the two branches manifests itself as mixing lines, which can be used for model validation.

The bottom panel of Fig. 4.2 shows the O_3-CO correlation of the in-situ measurements (grey) and CLaMS simulation (colored). The overall underestimation of CO can be also seen in this plot, similar to the CO profile discussed in Fig. 4.2. We can roughly identify the mixing lines of simulation and in-situ observations shown as the solid black and blue lines respectively. The mixing line of the observation is close to the tropospheric reservoir while the simulation-based mixing line leans to the stratospheric reservoir. The difference would become even worse if the artificial CO factor of 2 was removed. In other words, the CLaMS simulation tends to underestimate the tropospheric contribution and to overestimate the stratospheric contribution on STE.

Konopka et al. (2007) and *Pommrich et al.* (2014) reported that the CLaMS simulation shows reasonable tracer transport for most flight dates except for the dates with severe convection. One possible reason could be that the deep convection is not well resolved by the ECMWF reanalysis which drives the CLaMS

transport (mainly diabatic heating rate from ERA-interim, see *Ploeger et al.* (2010)). Although this point is difficult to address with direct measurements, *Wright and Fueglistaler* (2013) compared the diabatic heating in the UTLS from several reanalysis data sets and pointed out that the ERA-interim climatological diabatic heating is weakest in the tropical middle to upper troposphere among all the data sets (Figure 2 in *Wright and Fueglistaler* (2013)). This indicates that the ascending branch of the Hadley circulation in the inner tropics could be underestimated by ERA-interim.

Secondly, we discuss now the possibility that the convection-associated transport and mixing in the troposphere is insufficiently represented in the current mixing scheme of CLaMS. To reach a more global view instead of using only measurements during one single flight, we include more in-situ measurements of CO and O_3 of several campaigns. More information about these campaigns are shown in Appendix A.4. The in-situ measurements are divided into two groups according to the corresponding brightness temperature (BT) from Cloud Archive User Service (CLAUS) data with 1/3° horizontal resolution (*Hodges et al.*, 2000). One group embraces all the measurements where the corresponding brightness temperature is lower than 245 K. It contains $\sim$ 38000 measurements, which are interpreted as influenced by the deep convection. Another group includes the measurements where the brightness temperature is higher than 270 K, which is considered as the measurements without influence of moist convection. Around 24000 measurements are involved in this group.

Figure 4.3 shows the O_3-CO correlation of the two groups of in-situ measurements (top) compared with the CLaMS simulation (bottom). Following *Pan et al.* (2004) and *Kunz et al.* (2009), we assume that the undisturbed stratospheric air is characterized by CO mixing ratios lower than 35 ppbv (the area marked by "1") and tropospheric air mass is marked by ozone mixing ratio lower than 75 ppbv (the area marked by "2"). Accordingly, the points in the area marked by "3" are seen as the mixed air masses. For the group without deep convection, 41% out of the total measurements are found in area 3. STE of the group without deep convection is mainly caused by the bidirectional extratropical mixing along isentropes across the tropopause (*Hoor et al.*, 2002). The simulation of this group (bottom right) shows comparable representation of mixing: 37% of the air masses are considered mixed.

Among the measurements of the group with deep convection, there are 38% mixed air masses. The mixing is highly related to convection, including fast up-

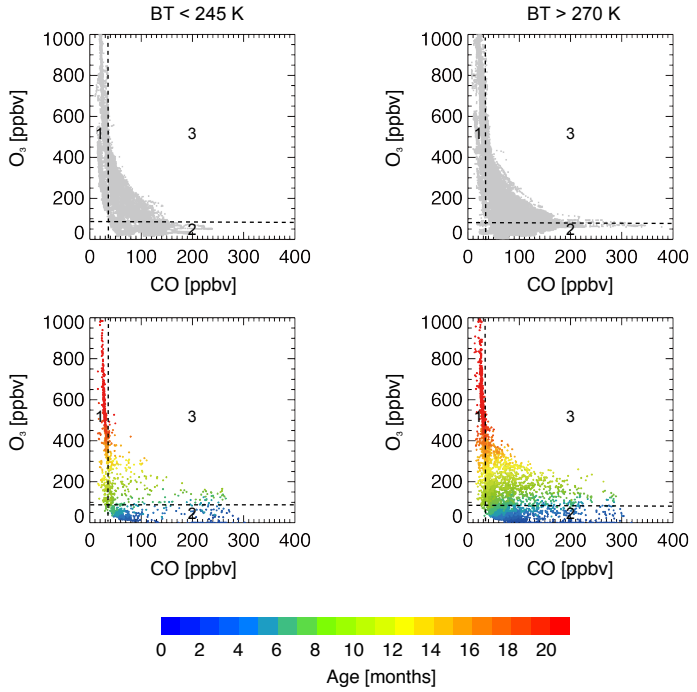

Figure 4.3: Comparison of O_3-CO correlation of in-situ measurements (top) with the CLaMS simulation (bottom). The left panel shows all the measurements and simulation when the local brightness temperature (BT) was below 245 K; the right panel shows those when the local BT was above 270 K. The mean age of air calculated with CLaMS is color-coded in the unit of months. The BT for corresponding measurements is interpolated from the CLAUS 0.3° resolution dataset. The dashed lines separate the O_3-CO correlation space into 3 regions: area 1 (unmixed stratospheric air where CO < 35 ppbv), area 2 (unmixed tropospheric air where O_3 < 75 ppbv) and area 3 (mixed air).

lift and convective mixing. However, the simulation shows underestimation of mixing: only 27% of mixed air masses in the area 3. Therefore, on the one hand, the current transport and mixing scheme in CLaMS shows a good ability to estimate the isentropic mixing. On the other hand, the representation of mixing and fast uplifting due to convection is insufficient in CLaMS. Note that the convective fast uplifting from the boundary layer and the tropospheric mixing are two different perspectives in CLaMS transport: the representation of convective uplifting should be carried out by re-estimation of the vertical velocity in the advection part of transport (trajectory) while the tropospheric mixing due to weak stabilities or even instabilities should be realized through extending the current mixing scheme.

4.2 Parameter for vertical stability – moist Brunt-Väisälä frequency

To improve tropospheric mixing in CLaMS, the first step is to find a parameter that quantifies the stability of the atmosphere. We start from the Boussinesq approximation of the vertical momentum equation describing the vertical motion of an air parcel in a hydrostatic reference atmosphere with mean profiles $p_0(z)$ and $\rho_0(z)$, i.e.:

$$\frac{dw}{dt} = -g\frac{\tilde{\rho}}{\rho_0} - \frac{1}{\rho_0}\frac{\partial \tilde{p}}{\partial z}, \tag{4.1}$$

where $\tilde{p}$ and $\tilde{\rho}$ is the deviation from the mean state and w denotes the vertical velocity. Following Archimedes, the first term on the right hand side describes the effect of buoyancy. Buoyancy per unit mass F_B is determined by the ratio between the mass of the air parcel with the volume V and the mass of the environmental fluid replaced by it, and is given by:

$$F_B = -\frac{\rho g V - \rho_0 g V}{\rho V} = -g\frac{\rho - \rho_0}{\rho} \approx -g\frac{\rho - \rho_0}{\rho_0} = -g\frac{\tilde{\rho}}{\rho_0}, \tag{4.2}$$

where ρ in the denominator of the forth term is approximated to the environmental density ρ_0 according to the Boussinesq approximation.

Assuming an adiabatic deviation of the air parcel from its mean state, i.e. $D\theta/Dt = 0$, using the ideal gas law and the incompressible assumption, the fol-

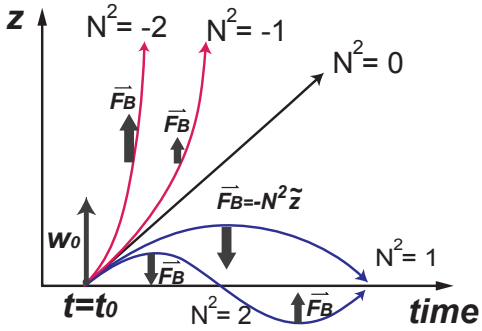

Figure 4.4: The different response of an air parcel to a vertical velocity w_0 under different stability condition in terms of N^2.

lowing relation can de derived (*Vallis*, 2006):

$$\frac{\tilde{\rho}}{\rho_0} = -\frac{\tilde{\theta}}{\theta_0}. \tag{4.3}$$

Accordingly, net buoyancy force F_B can be further written as:

$$F_B = -g\frac{\tilde{\rho}}{\rho_0} \approx g\frac{\tilde{\theta}}{\theta_0}. \tag{4.4}$$

Since the pressure gradient term tends to opposite to F_B, F_B is the upper limit of vertical acceleration dw/dt, which can also be written as $d^2\tilde{z}/dt^2$ with $\tilde{z}$ denoting the vertical displacement from the equilibrium state. By neglecting the pressure gradient term and assuming $\tilde{\rho} \sim -(d\rho_0/dz)\tilde{z}$ in eq. 4.1, the following relation can be derived:

$$\frac{d^2\tilde{z}}{dt^2} + N^2\tilde{z} = 0, \tag{4.5}$$

with

$$N^2 = -\frac{g}{\rho_0}\frac{d\rho_0}{dz}. \tag{4.6}$$

where N denotes the Brunt-Väisälä frequency. Figure 4.4 shows the vertical displacement variability of an air parcel with an initial upward vertical velocity (w_0) under five different stability conditions in terms of N^2. When $N^2 > 0$ (shown

as the blue curves), the solution of 4.5 is $\tilde{z} = Ae^{\pm iNt}$, which is a gravity wave with a vertical amplitude A and a period $2\pi/N$. Brunt-Väisälä frequency N^2 is then interpreted as the angular frequency of the oscillation. The smaller the N^2 is, the longer the oscillation period is. When $N^2 < 0$ (the red curves), the vertical acceleration is in the same direction with vertical displacement so that any small perturbation will be amplified, i.e. resulting in an unstable behavior.

Using the approximation of 4.3 and $\tilde{\rho} \approx -\tilde{\theta}\rho_0/\theta_0 = -\rho_0/\theta_0(d\theta_0/dz)\tilde{z}$, the form of Brunt-Väisälä frequency in eq. 4.6 can be rewritten as:

$$N^2 \approx \frac{g}{\theta_0}\frac{d\theta_0}{dz}. \tag{4.7}$$

Therefore, the relation between the net buoyant force and the 'measure of stability' expressed in terms of Brunt-Väisälä frequency can be derived from eq. 4.4 and eq.4.7 as:

$$F_B = g\frac{\theta - \theta_0}{\theta_0} = g\frac{\tilde{\theta}}{\theta_0} \approx -N^2\tilde{z}, \tag{4.8}$$

which is shown as the thick vectors F_B in Fig. 4.4.

Thus, because of 4.7, the sign of buoyancy F_B is related to the sign of $d\theta_0/dz$. For the hydrostatic dry atmosphere, this condition translates into the dry adiabatic lapse rate Γ_d, given by

$$\Gamma = -\frac{dT}{dz} = \frac{g}{c_p} = \Gamma_d \approx 10\ \mathrm{K/km} \tag{4.9}$$

An air column with a temperature profile (lapse rate γ) decreasing faster than Γ_d is unstable (*Wallace and Hobbs*, 1977). For the hydrostatic atmosphere with water vapor content saturated with respect to liquid water, the same consideration (see also Appendix A.5) leads to the following stability conditions in the temperature space:

$$\gamma < \Gamma_s - \text{stable} \tag{4.10}$$

$$\Gamma_s < \gamma < \Gamma_d - \text{conditionally unstable} \tag{4.11}$$

$$\Gamma_d < \gamma - \text{unstable} \tag{4.12}$$

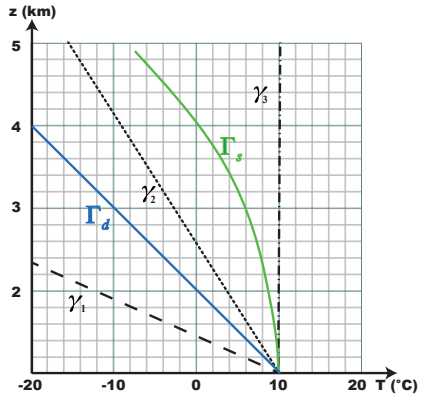

Figure 4.5: The three stability conditions under three environmental lapse rates: unstable (environmental lapse rate γ_1); conditionally unstable (environmental lapse rate γ_2) and absolutely stable (environmental lapse rate γ_3). The blue line shows the dry adiabatic lapse rate and the green curve shows the saturated lapse rate.

with the saturated lapse rate Γ_s,

$$\Gamma_s = \frac{\Gamma_d}{1 + \frac{L}{c_p}\frac{dw_s}{dT}} \approx 6 \text{ K/km} \tag{4.13}$$

where L denotes the latent heat of vaporization and w_s denotes the saturation mass mixing ratio with respect to water (e.g., *Wallace and Hobbs*, 1977).

The three types of stability are shown in Figure 4.5. During a dry adiabatic ascent, cooling of an unsaturated air mass follows the dry adiabatic lapse rate ($\Gamma_d \sim 10$ K/km, the blue line). When the environmental temperature profile, for example the γ_1 in Fig. 4.5 decreases faster than Γ_d and thus the air parcel is warmer than the environment, the atmosphere is unstable and otherwise, it is stable. When an air mass is saturated, the latent heat release from condensation will compensate the cooling during the further ascending. Thus, the lapse rate for the wet ascending (saturated lapse rate Γ_s, the green curve in Fig. 4.5) is smaller than Γ_d. In this sense, when the environment temperature decreases with altitude slower than Γ_d but faster than Γ_s e.g. γ_2, it is stable for an unsaturated air mass but unstable for a saturated air mass, which is called 'conditionally unstable'.

For quantifying the contribution of latent heat release to the vertical instabilities, Brunt-Väisälä frequency can be modified by introducing the moist Brunt-Väisälä frequency N_m:

$$N_m^2 = \frac{g}{\theta_e}\frac{\partial \theta_e}{\partial z}. \tag{4.14}$$

where θ_e is equivalent potential temperature, the temperature an air parcel would reach if all the water vapor in the air parcel were to condense, releasing its latent heat and then brought down to 1000 hPa (*Holton* (1992); *Ertel* (1938), more details about θ_e can be found in Appendix A.5). In particular, when the air contains no moisture, the wet potential temperature θ_e is equal to the potential temperature θ. Because of the energy released by the phase transition from water vapor to liquid water (or to the ice phase), the N_m^2 is smaller than N^2 and N_m^2 can be negative where N^2 is positive (conditionally unstable). The energy released by the phase transition from liquid water to the ice phase can be neglected in most cases because the respective latent heat is smaller by a factor of 10 than the latent heat of gas-liquid transition (334 kJ for melting versus 2270 kJ for evaporation for 1 kg liquid water).

To quantify the effect of moisture on the buoyancy force F_B, eq. 4.8 has to be replaced by:

$$F_B = -N_m^2 \tilde{z}. \tag{4.15}$$

Therefore, conditionally unstable buoyancy and negative values of N_m^2 are two sides of the same coin.

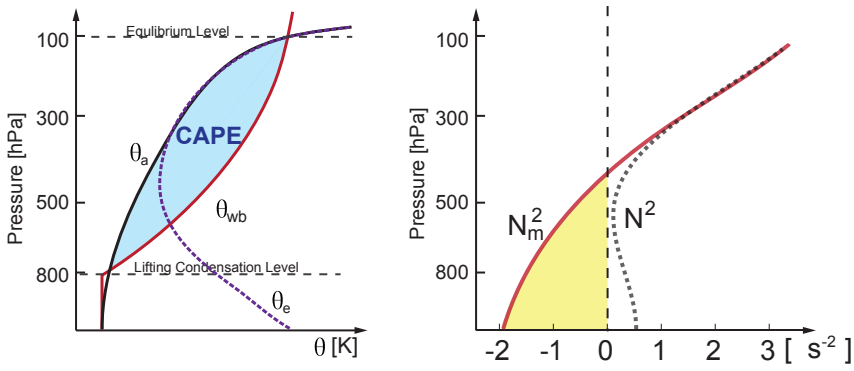

Figure 4.6: CAPE versus Brunt-Väisälä frequency.

For convective precipitation, severe weather analysis and forecasting, the concept of convective available potential energy (CAPE) is widely used (*Moncrieff and Miller*, 1976) (see Figure 4.6) which is defined (in J/kg) as the follow-

ing integral:

$$\text{CAPE} = \int_{LFC}^{EL} \frac{g(\theta_{wb}(z) - \theta_a(z))}{\theta_a(z)}\, dz, \tag{4.16}$$

where θ_a is the potential temperature of the environment (ambient air) and θ_{wb} is the so-called wet-bulb potential temperature or saturation potential temperature which needs some further explanation: We begin with the lifting condensation level (LCL) defined as the height at which a parcel of air becomes saturated when it is lifted adiabatically from the Earth's surface (so the potential temperature does not change). Starting from the LCL, the air parcel is then transported along a moist adiabatic process (i.e. a pseudoadiabatic process for which the air is saturated). The corresponding potential temperature within such a parcel defines the web-bulb potential temperature. Note that a distinction is made between the reversible process, in which total water is conserved, and the pseudoadiabatic or irreversible moist adiabatic process, in which liquid water is assumed to be removed as soon as it is condensed. When rising up to a certain level almost all the water vapor in the air parcel is condensed and removed. Finally, around 100 hPa, the equilibrium level (EL) is reached. EL is defined as the height where the (potential) temperature of a buoyantly rising parcel again equals to the (potential) temperature of the environment, i.e. $\theta_a = \theta_{wb}$.

Alternatively, the CAPE can be also quantified through the amount of work done by the positive buoyancy during the moist convective process from the LFC to the EL as:

$$CAPE = \int_{LFC}^{EL} F_B\, dz. \tag{4.17}$$

We conclude that whereas CAPE describes the integral property of an (conditionally) unstable profile, N_m^2 quantifies more the altitude-resolved property of such a profile. In the following, we use N_m^2 to identify atmospheric conditions when convective mixing may happen and to quantify the threshold for triggering deep convection in the parameterization.

4.2.1 Moist Brunt-Väisälä frequency representation of deep convection

In the previous section, we physically interpreted moist Brunt-Väisälä frequency N_m based on the thermodynamics and clarified the theoretical connection with the buoyancy force, environmental thermal structure and CAPE. In this section,

we will analyze the distribution of N_m derived from ERA-Interim reanalysis data and compare it with CAPE from ERA-interim and brightness temperature (BT) from CLAUS data. Figure. 4.7 shows the distribution of zonally averaged moist

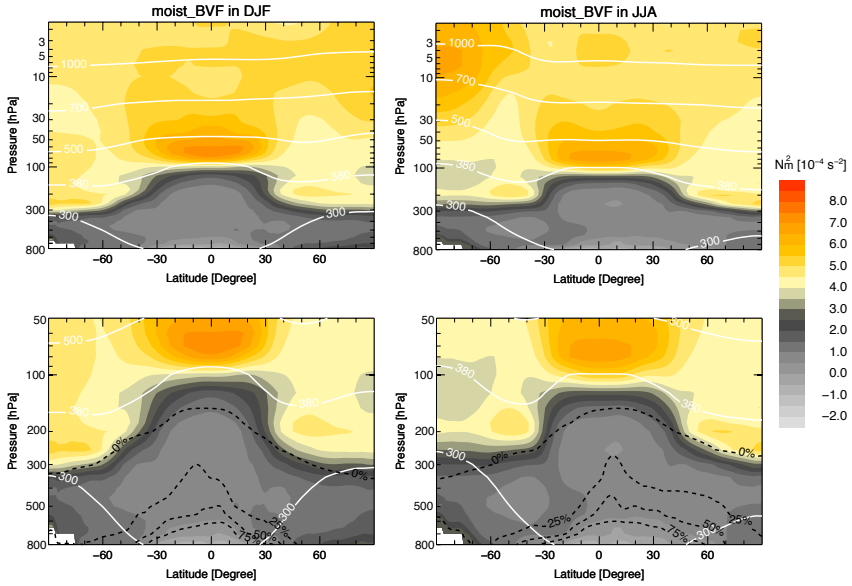

Figure 4.7: The top panel is the same as Fig. 4.1 but for moist Brunt-Väisälä frequency N_m^2 . The bottom panel is the same as top panel but the vertical range is limited in the troposphere and the lower stratosphere. The black dashed contours show the 0%, 25%, 50% and 75% relative difference to the dry Brunt-Väisälä frequency shown in Fig. 4.1.

Brunt-Väisälä frequency N_m^2 in winter (DJF) and summer (January). Given that N_m^2 is smaller than N^2, we can see that the largest differences between N_m^2 and N^2 are confined to the troposphere (here plotted as the relative difference, i,e. $(N_m^2 - N^2)/N^2$). The differences between the moist and dry Brunt-Väisälä frequency result from the effect of moisture, which mainly exists in the lower to middle troposphere and it maximizes in the tropics. Moreover, the difference is larger in boreal summer than that in boreal winter. In boreal winter, the 25% contour stretches from 60°S to 40°N, while it covers the whole northern hemisphere and

extends to 60°S in boreal summer.

The moist Brunt-Väisälä frequency N_m^2, which relates the buoyancy and vertical motion, is expected to be an indicator of moist deep convection. Fig-

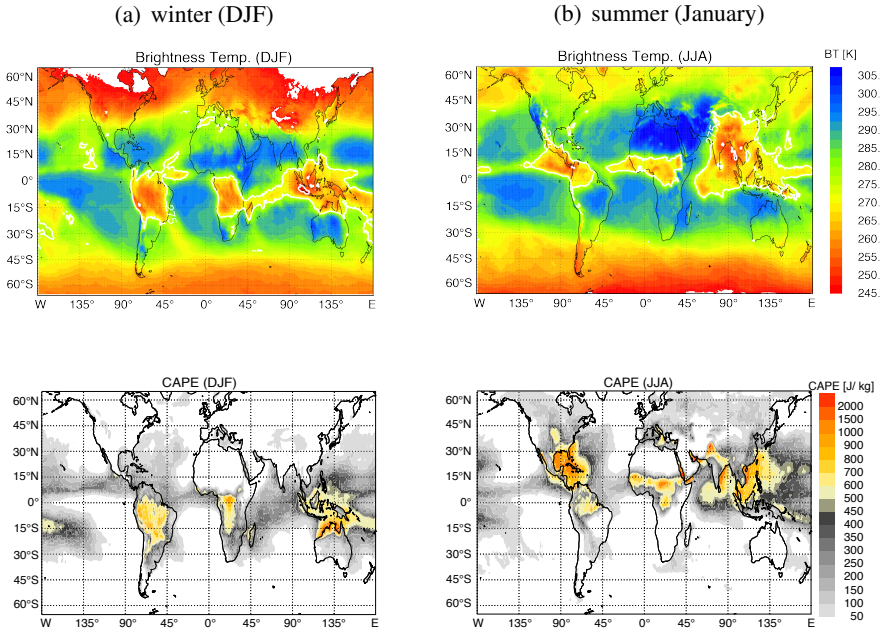

Figure 4.8: Top: the brightness temperature distribution from CLAUS dataset and the white contours indicate the BT lower than 275K in tropics; bottom: the convective available potential energy (CAPE) distribution from ERA-interim and the region where CAPE value higher than 500 J/kg is highlighted with yellow-orange colors. The left panels are for the winter 2008-2009 (DJF) and the right panels are for the summer 2008 (JJA).

ure 4.8 shows the horizontal distributions of brightness temperature (top) and CAPE (bottom) averaged over the 2008-2009 winter (DJF) and 2008 summer (JJA), respectively. The observations of convection are provided by CLAUS infrared brightness temperature (BT) assimilation data of 1/3° and 3 hour resolution (*Hodges et al.*, 2000) (more details about CLAUS in appendix A.3). A relatively low brightness temperature is an indicator of a high cloud top. Here we focus on the BT in the tropics (30°S−30°N) because less deep convection

happens in high latitudes and the infrared BT in high latitudes are strongly affected by high-albedo surface with ice and snow as well as the large zenith angle of the geostationary satellites.

The BT distribution illustrates the regions of deep convection in the tropics. The well-known seasonality of deep convection is displayed: The Intertropical Convergence Zone (ITCZ) moves from the equator to the north ($\sim$10°N) from boreal winter to summer and an enhanced ITCZ can be seen in the northern hemisphere during summer; the deep convection is more likely over land than over sea in general; the strongest convective regions are found over the Maritime Continent in both seasons, South America and South Africa in DJF and South Asia and West Africa in JJA.

The maps of CAPE agree with the corresponding BT distribution to a high degree. However, some differences can be noticed, especially in JJA. For example, the deep convection region over northern South America extends to the East Pacific. It is detected by the BT data while large CAPE values occurs less frequently in the northern South America but more in the Gulf of Mexico. The Asian summer monsoon region is another example: large CAPE is found mainly over the west Pacific and Indian Ocean whereas the low BT locates more over the south Asia. Note that CAPE, an indicator of the available energy which could be released for the convection. But large CAPE cannot guarantee the occurrence or quantify the intensity of convection. It is because CAPE ignores entrainment into convective plume and the air masses have to overcome the negative buoyant force between the surface and the LFC level. This amount of necessary energy suppresses the development of convection in the boundary layer, which is called Convective Inhibition (CIN). If not enough 'input' energy is provided by external forcing, e.g. surface heating, moistening, strong front or orographic lifting, the 'output' energy CAPE cannot be released. These are possibly the reasons for the differences between the climatologies of CAPE and of BT.

Figure 4.9 illustrates the distributions of conditionally unstable regions ($N_m^2 < 0$) below $\zeta = 300$ K and the distributions of weak stabilities at the upper layers in the troposphere. Note that N_m^2 is derived from the ERA-interim reanalysis data, which is of $\sim$100 km horizontal resolution. These data cannot fully capture the convective process with a typical scale smaller than 100 km but show weak stabilities or even instabilities in these regions.

When comparing with CAPE and BT, the statistics of the unstable as well as weakly stable moist Brunt-Väisälä frequency shows reasonable distributions

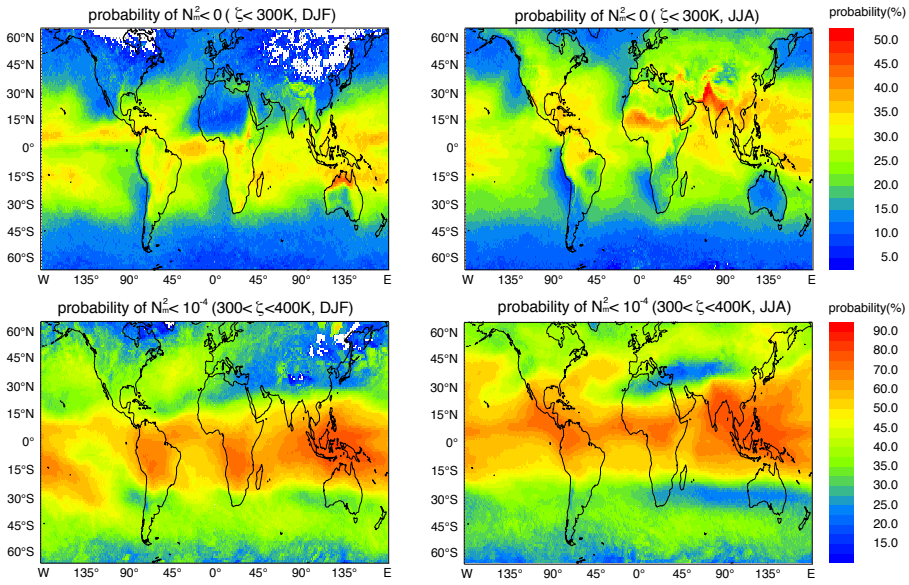

Figure 4.9: Top: the probability of moist Brunt-Väisälä frequency N_m^2 being negative below 300 K in the hybrid isentropic coordinate; bottom: the probability of moist Brunt-Väisälä frequency N_m^2 being smaller than $1.0 \cdot 10^{-4}$ s^{-2} from 300 K to 400 K in the hybrid isentropic coordinate. The left panels are for the winter 2008-2009 (DJF) and the right panels are for the summer 2008 (JJA).

in Fig. 4.9. The deep convection patterns shown by CAPE and BT are also represented by the high probability region with instabilities for $\zeta < 300$ K and weak stabilities in the ζ range between 300 K and 400 K. It is also noticed that the map of unstable N_m^2 below 300 K agrees better with maps of CAPE while the distribution of weakly stable N_m^2 between $\zeta = 300$ K and 400 K agrees better with BT instead, especially in boreal summer. This confirms that the measure of instability by moist Brunt-Väisälä frequency in the lower troposphere basically reflects the distribution of CAPE because the unstable N_m^2 represents the growth stage of CAPE in the lower layers. In the middle to upper troposphere, on the other hand, the weakly stable N_m^2 reproduces the distribution of BT, which shows the pattern of the convective cloud top in the tropics. Here we conclude that the moist Brunt-Väisälä frequency is a good indicator of weak stability that triggers deep convection in the troposphere. It can be utilized as a parameter to quantify

the convective mixing.

4.3 Extension of transport scheme: tropospheric mixing and deep convection

To extend the CLaMS mixing scheme, we follow two heuristic ideas: First, due to a much lower vertical stability in the troposphere than in the stratosphere, we would like to enhance tropospheric mixing in the model almost everywhere where (moist) vertical stability is sufficiently small. This is motivated by the general observation that the troposphere, especially the boundary layer and the regions with deep convection, is vertically well-mixed, if compared with the strongly stratified stratosphere where vertical profiles of many species show pronounced small scale structures and filaments. Second, we would like also to take into account additional transport driven by convection, especially by deep convection which is not sufficiently resolved in the reanalysis data.

Thus, whereas the first approach is related to changes in the mixing part of CLaMS and affects the next neighbors of each Lagrangian air parcel, the second goal is related to changes in the advection part of CLaMS, i.e. to modification of the trajectory calculation. As we show in the following two subsections, both extensions are driven by instabilities quantified in terms of the (moist) Brunt-Väisälä frequency N_m^2. By including the revised scheme, we seek for a better tracer distribution in the free troposphere, which could potentially improve the performance of the model within the UTLS region. Because all our changes are confined to the lower and middle troposphere where moist Brunt-Väisälä frequency N_m^2 strongly deviates from the dry Brunt-Väisälä frequency N^2, we expect that all these change will not significantly affect the stratospheric transport in CLaMS which has been successfully validated in many previous studies (e.g., *McKenna et al.*, 2002a; *Müller et al.*, 2005; *Tao et al.*, 2015a). Furthermore, the scheme should not give a heavy burden on the computation time compared to the current version of CLaMS.

4.3.1 Extension of the mixing scheme (tropospheric mixing)

In the following, we assume that the additional tropospheric mixing should be triggered whenever the corresponding N_m^2 of the model grid is less than a critical value of N_m^2 denoted in the following as BVF_0. BVF_0 is a free parameter which,

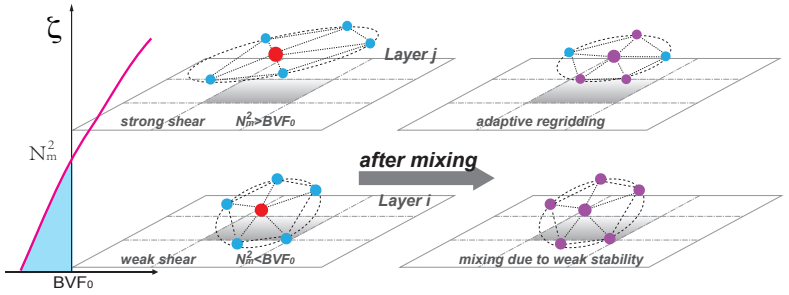

Figure 4.10: Mixing driven by vertical weak stability and strong wind shear. The profile on the left side is an idealized N_m^2 profile derived from the reanalysis and interpolated on the CLaMS air parcels (red). The lower part is representative for the troposphere with $N_m^2 < \mathrm{BVF}_0$ and the upper part for the stratosphere with $N_m^2 > \mathrm{BVF}_0$. Thus, in the lower layer static stability and the wind shear are weak with the opposite configuration in the upper layer, schematically representing troposphere and stratosphere, respectively. In the upper layer, adaptive regridding is used to include mixing (default mixing in CLaMS). In addition, in the lower layer, air parcels will be also mixed if criterion $N_m^2 < \mathrm{BVF}_0$ is valid. The purple parcels are mixed parcels of red and blue parcels.

basically, can be adjusted by comparison with the experimental data. We expect that BVF_0 should be a very small number close to zero (the threshold of N_m^2 will be shown in Fig. 4.11), which is able to identify some (convective) instabilities. If an air parcel fulfills the criterion $N_m^2 < \mathrm{BVF}_0$, the air parcel will be mixed with all next neighbors diagnosed by Delaunay triangulation in the respective CLaMS layer under consideration (so we use the same next neighbors as in the current scheme). In this way the composition of the considered air parcels are affected, but not their geometric positions.

Figure 4.10 is a schematic diagram illustrating how the tropospheric extension of mixing works. If this additional mixing is applied, we set the new mixing ratio of a considered air parcel and its next neighbors through averaging their composition, which is shown as a change of the parcel's color. This setting completes the mixing without changing any model parcel position and the number of parcels because it can be executed directly in the current mixing module (more precisely, after deformation driven adaptive grid procedure introduced in the first

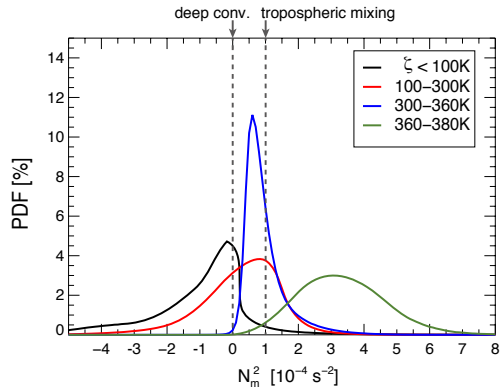

Figure 4.11: The probability distribution functions (PDFs) of N_m^2 in the tropics (30°S- 30°N) based on the ERA-interim reanalysis data of the year 2008. The PDFs of N_m^2 for four vertical ranges (in the ζ coordinate) are shown in different colors. The criterion used for the current 'troposphere mixing' ($\mathrm{BVF}_0 = 1.0 \cdot 10^{-4}$ s^{-2}) and for the 'deep convection' scheme ($\mathrm{BVF}_0 = 0.0$) are marked as the dash straight lines. The parameterization of the 'deep convection' will be explained in the next section.

chapter 1.4.1).

The proportion of APs participating in the 'tropospheric mixing' is determined by the criterion based on N_m^2. Figure 4.11 shows the PDFs of N_m^2 in the tropics (30°S- 30°N) within four different vertical ranges. We notice that the PDFs of N_m^2 vary with altitudes. The dependence of PDFs on the seasons was also checked but it is not significant. The probability of N_m^2 in the model lower boundary (shown as the black curve) that is defined as the layer below $\zeta = 100$ K in CLaMS reach its maximum when N_m^2 is around zero. Also the PDF of N_m^2 below $\zeta = 100$ K is asymmetric about zero and has larger probability ($\sim$80%) for negative values. The N_m^2 within 100 K $< \zeta <$ 300 K (the red curve) reach the maximal probability at around $N_m^2 = 1.0 \cdot 10^{-4}\mathrm{s}^{-2}$. Its PDFs also show asymmetry about its maximum and the probability for N_m^2 being negative is still large ($\sim$40%). The PDF of N_m^2 within 300 K $< \zeta <$ 360 K (the blue curve) concentrates within the values between 0 and $2.0 \cdot 10^{-4}\mathrm{s}^{-2}$. Its probability for being negative is almost negligible and the probability for $N_m^2 < 1.0 \cdot 10^{-4}\mathrm{s}^{-2}$ is about 65%. Up to 360 K $< \zeta <$ 380 K, almost all the N_m^2 values are positive and the

probability for $N_m^2 < 1.0 \cdot 10^{-4}\mathrm{s}^{-2}$ is also very small ($\sim$4%). In the following CLaMS runs testing the extension of the mixing scheme, the criterion of N_m^2 (BVF_0) is set to $1.0 \cdot 10^{-4}\mathrm{s}^{-2}$. According to the PDF of N_m^2, nearly all the APs ($\sim$95%) in the tropics within the model lower boundary and more than half of APs in the tropical troposphere are affected by 'tropospheric mixing' while the effect of 'tropospheric mixing' is restricted to the troposphere. We tested several criteria for BVF_0 (0, 0.5, 1, 2, unit: 10^{-4} s^{-2}) through 6-month CLaMS runs and the run with $\mathrm{BVF}_0 = 1.0 \cdot 10^{-4}$ s^{-2} showed the best results (not shown) compared with START-08 in-situ CO and O_3 measurements (overviewed by *Pan et al.* (2010)). Nevertheless, futher optimization of the criterion needs to be done in the future.

4.3.2 Parametrization of unresolved convection (deep convection)

It is generally believed that the exchange of mass driven by deep convection can efficiently inject the air masses from the boundary layer into the upper troposphere or even, although very rarely, into the lower stratosphere. In fact, the extension of mixing presented in the previous subsection is still limited by the model layers and, consequently, is not suitable to parametrize unresolved convective events which should connect the boundary layer with layers in the upper troposphere. Because the identification of neighbors is confined inside of each model layer, the exchange across layers is so far driven by the vertical velocity $\dot{\theta}$ derived from the diabatic heating rates.

There have been some studies attempting to apply Eulerian convective parameterizations to Lagrangian transport models. *Collins et al.* (2002) implemented convective transport into a Chemistry-Transport Model (CTM) using convective mass fluxes on an Eulerian grid. The convective mixing is implemented in the UK Met Office's long-range dispersion model (NAME) through randomly redistributing Lagrangian particles between the cloud base and cloud top (*Jones et al.*, 2007) and the convective mixing scheme was recently updated to a 1-dimensional 'mass-flux' model (*Meneguz and Thomson*, 2014). *Stohl et al.* (2005) included the convective transport and mixing to FLEXPART using another Eulerian parameterization scheme by *Emanuel* (1991). *Forster et al.* (2007) further reexamined and revised the convective scheme of FLEXPART to reduce the computation cost and evaluated by comparison with ^{222}Rn measurements from two aircraft campaigns. These results with the models implemented Eulerian convective parameterization illustrate that the convection has large poten-

tial to vertically redistribute the chemical components. On the other hand, it is also shown that the simulation results are subject to large uncertainties due to different convection parameterizations. Our main aim in this section is to improve the representation of deep convection in CLaMS by a simple modification of the trajectories (i.e. of the advective part of the transport). Therefore, we propose a simple modification based on the current transport scheme, i.e. on the Lagrangian trajectories in CLaMS.

Note that another possible improvement to the extension of mixing scheme is to redefine the model layers based on entropy and static stability as proposed by *Konopka et al.* (2012), which in principle connects the thickness of the model layers to the static stability ($\Delta z \propto 1/N_m$). In this way, the layer would be thicker in a relatively unstable or weakly stable region and thus the corresponding mixing would cover a larger vertical distance. This possibility will be explored in the future.

An important property of convection is that convective updrafts are compensated by a large-scale downdrafts. While the updrafts are mostly confined within the convective temporal and spacial scales, the downdrafts occur in a much larger scales through the general circulation and large-scale downwelling. However, on tropical isentropes around the convective outflow, the integrated mass fluxes are not perfectly balanced, as downwelling overweights upwelling (at least in the ERA-Interim world, see *Fueglistaler et al.* (2009)), giving in this way some space for (unresolved) updrafts. Furthermore, the relatively weak upward mass flux derived from the ERA-Interim diabatic heating rates in the troposphere compared with other reanalysis data sets (*Wright and Fueglistaler*, 2013) gives also some additional freedom to increase the convective upward transport.

Here, we present an alternative method to increase upward transport in the regions meeting the criterion of N_m^2 in order to lift young air masses from the boundary layer. Figure 4.12 shows the concept of estimating the uplift of boundary air by adding a $\Delta\theta$ to the trajectory in the vertical direction when instabilities diagnosed in terms of low values of N_m^2 are diagnosed along the trajectory.

To derive the expression for $\Delta\theta$, we start from the second law of thermodynamics, i.e.:

$$dS = \frac{\delta Q}{T}. \tag{4.18}$$

We assume that the source of heating is the latent heat release of water vapor condensation. The infinitesimal latent heat release from water vapor condensation

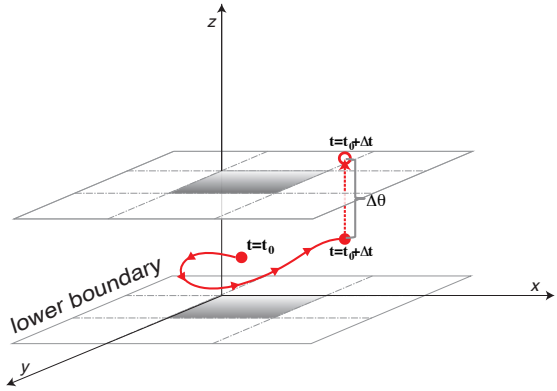

Figure 4.12: The original trajectory (thick solid red) and the modified trajectory (dashed red) with convective transport from the lower boundary layer for one time step (Δt). The vertical displacement $\Delta\theta$ is estimated through the latent heat release of condensation.

of an (unit mass) air parcel is given by

$$\delta Q = -L_v d\mu_s \tag{4.19}$$

where L_v is the specific latent heat for evaporation (or condensation) and μ_s is the saturation water vapor mass mixing ratio.

Thus, considering the relationship between infinitesimal increment of entropy dS and the infinitesimal increment of potential temperature $d\theta$ (see the derivation in Appendix A.5):

$$ds = c_p \frac{d\theta}{\theta} \tag{4.20}$$

and substituted δQ by the relation in eq. 4.19, the $d\theta$ can be derived as

$$d\theta = -\frac{L_v \theta d\mu_s}{c_p T}, \tag{4.21}$$

where T is the saturation temperature. Then we make the integral of $d\theta$ from the initial state θ_0 to the state $\theta_0 + \Delta\theta$ when certain amount of water vapor $\Delta\mu_s$ is

condensed:

$$\int_{\theta_0}^{\theta_0+\Delta\theta} \frac{d\theta}{\theta} = -\int_{\mu_s(\theta_0)}^{\mu_s(\theta_0+\Delta\theta)} \frac{L_v d\mu_s}{c_p T}. \tag{4.22}$$

The result of the integral after transformation can be written as:

$$\Delta\theta = \theta_0[\exp\left(\frac{L_v\Delta\mu_s}{c_p T}\right) - 1], \tag{4.23}$$

where $\Delta\mu_s = \mu_s(\theta_0) - \mu_s(\theta_0+\Delta\theta)$. Because $\frac{L_v\Delta\mu_s}{c_p T} \ll 1$, a first order approximation of the right hand side of eq. 4.23 through the Taylor expansion of the exponential function (*Ertel*, 1938) is

$$\Delta\theta = \frac{L_v\theta_0\Delta\mu_s}{c_p T}, \tag{4.24}$$

which gives a relationship between the total change of the potential temperature and the change of water vapor mass mixing ratio. Strictly, $\Delta\mu_s$ is the change of the water vapor saturation mass mixing ratio before and after a model time step. In the 'deep convection' scheme, $\Delta\mu_s$ is estimated by the total water vapor mass mixing ratio μ_w before the model time step with the assumption that 1) the time scale of deep convection and its associated condensation is smaller than one model time step; 2) the residual water vapor content after deep convection ($\mu_s(\theta_0+\Delta\theta)$) is so small that it can be neglected. Thus, the $\Delta\mu_s$ is assumed to be the total water vapor mass mixing ratio μ_w along the air parcel trajectory when the criterion of 'deep convection' ($N_m^2 < BVF_0$) is fulfilled. Therefore, the uplifting of air parcels in the 'deep convection' scheme is estimated by

$$\Delta\theta = \frac{L_v\theta_0\mu_w}{c_p T}. \tag{4.25}$$

This part of the parametrization should be treated with great caution because any modification to the trajectories influence the density of parcels in the model. Note that the number of parcels in CLaMS is not strictly conserved but kept rough constant within about $\pm 10\%$ flexibility through the adaptive regridding procedure (current mixing scheme). It means that the mixing procedure is able to adjust a certain increase or decrease in the number of air parcels but this amount should be under $\pm 10\%$.

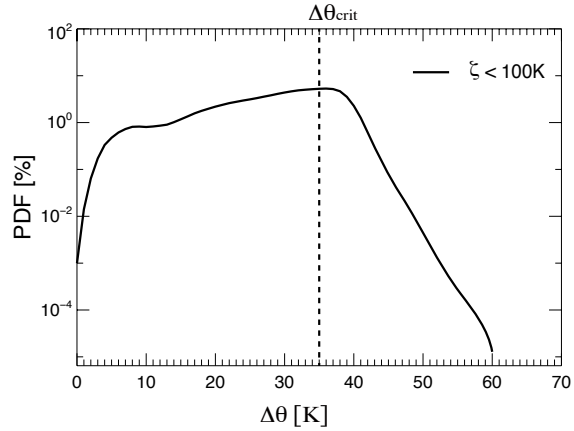

Figure 4.13: The probability distribution functions (PDFs) of $\Delta\theta$ in the tropics (30°S- 30°N) for the air parcels in the lowest level of CLaMS ($\zeta < 100$ K≈ 2 km) where N_m^2 is negative using the ERA-interim reanalysis data of the year 2008. The restriction used for the current 'deep convection' scheme ($\Delta\theta > 35$ K) is marked as the dash straight line.

Therefore, the first criterion of applying $\Delta\theta$ to the original trajectory is that the trajectory goes through an (conditionally) unstable or weakly stable environment. This criterion for the test runs for the 'deep convection' is $N_m^2 < 0$ as shown in Fig. 4.11. According to the PDFs shown in Fig. 4.11, about 80% of the grid points in the tropics meet the criterion. Secondly, we restrict the 'deep convection' scheme to the trajectories starting from the model lower boundary. After applying these two restrictions, Figure 4.13 shows the one-year climatological PDF of $\Delta\theta$ in the tropics (30°S- 30°N). The probability of $\Delta\theta$ larger than 35 K is around 35% and it decreases rapidly from 35 K to 60 K. When the $\Delta\theta$ is too small for crossing the lower boundary, it is not necessary to add $\Delta\theta$ to the trajectory. Thus, we only apply the $\Delta\theta$ to the trajectory when the $\Delta\theta$ is sufficiently large. In the test runs, the minimum $\Delta\theta$ is set to 35 K shown as the dashed line in Fig. 4.13.

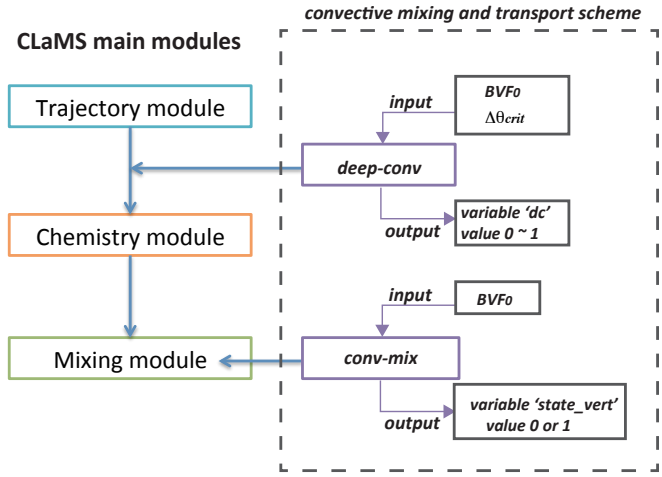

Figure 4.14: Implementation of deep convection and tropospheric mixing into the CLaMS trajectory and mixing modules.

4.3.3 Implementation into CLaMS

The moist Brunt-Väisälä frequency N_m^2 is computed from the ECMWF ERA-Interim temperature and specific humidity profiles, and is added as a diagnostic variable to the other ECMWF meteorological fields, which drive transport and chemistry in CLaMS. The quality of the ECMWF humidity was recently assessed by *Kunz et al.* (2014). Thus, N_m^2 and all other fields are available every 6 hours and can be directly interpolated onto the Lagrangian air parcels of CLaMS.

A schematic structure of the new modules is shown in Figure 4.14. The extension of the convective transport is executed by the module called 'deep-conv'. Here, we check along each 6 hours trajectory starting in the boundary layer if the criteria for deep convection are fulfilled (see section 4.3.2). If yes, the trajectory is shifted upwards by $\Delta\theta$ calculated from the relation 4.24.

A new block of extended mixing is added to the mixing module, which is named 'vert-mix'. The 'vert-mix' selects the Lagrangian grids where N_m^2 is smaller than BVF_0 and then mixes them with their next neighbors.

For later diagnostics we use two variables, 'dc' and 'state-vert' to tag all those air parcels which were affected by deep convection or tropospheric mixing,

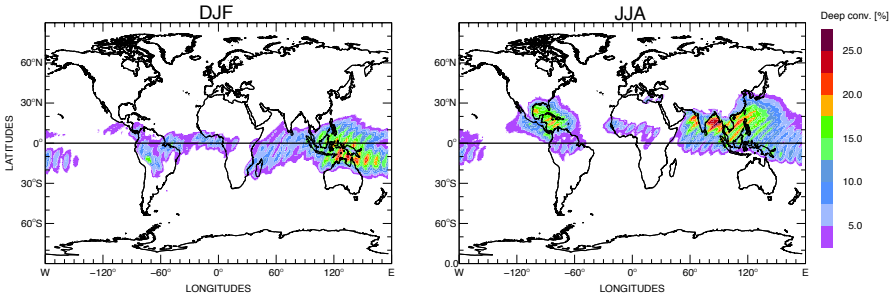

Figure 4.15: The horizontal distribution of additional upward transport due to deep convection parameterization at θ= 340 K in DJF (left) and JJA (right). The intensity of this transport is described by the probability of parcels involved in the deep convection module.

respectively. If the trajectory is modified by 'deep-conv', 'dc' is assigned the value '1'. Otherwise, it is assigned the value '0'. Because the variable 'dc' is also involved in the mixing procedure, it is mixed like a tracer. Thus, the output of 'dc' after each time step indicates how much every air parcel is affected by the deep convection. The variable 'state-vert' records the mixing state for the tropospheric mixing. When an air parcel was involved in the tropospheric mixing, the variable 'state-vert' is assigned to the value '1', otherwise, it is set to zero. Note that there is another similar variable 'state' which records the state due to mixing following the adaptive re-gridding procedure (>0/0 affected/not affected by the re-gridding algorithm).

4.4 Results

4.4.1 Result of diagnostic variables

We run the standard CLaMS (CLaMS-R) and CLaMS with deep convection and tropospheric mixing (CLaMS-C) covering the year 2008. The trajectory time step is set to 6 hours for getting close to the time scale of deep convection (*Vogel et al.*, 2011) and the critical Lyapunov exponent $\lambda_c = 3.0$ is applied after every advection time step, which is introduced as a mixing parameter in section 1.4.1.

Figure 4.15 shows the climatological distribution of the parameter 'dc' at

$\theta = 340$ K isentropic level derived from CLaMS simulation. This distribution quantifies the probability where additional (deep) convection occurs transporting air parcels from the boundary layer to the considered θ-level. There is a qualitative good agreement of deep convection intensity compared with the distribution of brightness temperature and CAPE as shown in Fig. 4.9. The high values of 'dc' probability concentrate within low latitudes. In DJF, the high values are found over the Maritime Continent, South Indian Ocean, South-West Pacific Ocean, South America and Middle Africa. During JJA, the regions with high values shift northward of the equator whereas during DJF the distribution is more symmetric over the tropics.

The 'deep-conv' scheme uplifts the young air parcels from the lower boundary to the higher model layers if such air parcels meet the criterion $N_m^2 < 0$. The vertical distance $\Delta\theta$ of the uplift itself is determined by the potential latent heat from the maximum available water vapor condensation and is mostly ($\sim$99%) not larger than 50 K (Fig. 4.13). Therefore, the effect of 'deep-conv' is confined within the troposphere so that 95% parcels with non-zero 'dc' values can be found below $\sim$350 K.

At the same time, the 'vert-mix' scheme implemented in the mixing module identifies the regions where stability is sufficiently weak ($N_m^2 < 1.0 \cdot 10^{-4}$ s^{-2}) for all the model layers. Therefore, parcels everywhere in the troposphere can be mixed if the value of N_m^2 interpolated at the position of the air parcel is sufficiently small. The results of 'state-vert' (state of tropospheric mixing) at θ= 330 K, θ= 360 K and θ= 380 K are shown in Figure 4.16.

Because we set the criterion for 'tropospheric mixing' to a small positive number instead of zero, the probability of 'state-vert' to be triggered is larger than that of 'dc'. We notice that the distribution of 'state-vert' varies with altitude, which is also noticeable in Fig. 4.11. At θ= 330 K, the tropospheric mixing affect almost all the air parcels in the tropics as well as in the subtropics in the summer hemisphere. At θ= 360 K, the influence of the 'tropospheric mixing' is smaller and basically concentrates in the convection-active region, e.g. the Maritime Continent and tropical Pacific Ocean in DJF and Asian monsoon region in JJA. Up to θ= 380 K, the 'tropospheric mixing' further decreases and the most intensive mixing due to convective instability occurs over the Maritime Continent and southeastern Pacific Ocean during boreal winter while the highest values of mixing are found over South Asia and the Tibetan Plateau during the summer months. Therefore, it is very likely that young air masses in these regions are

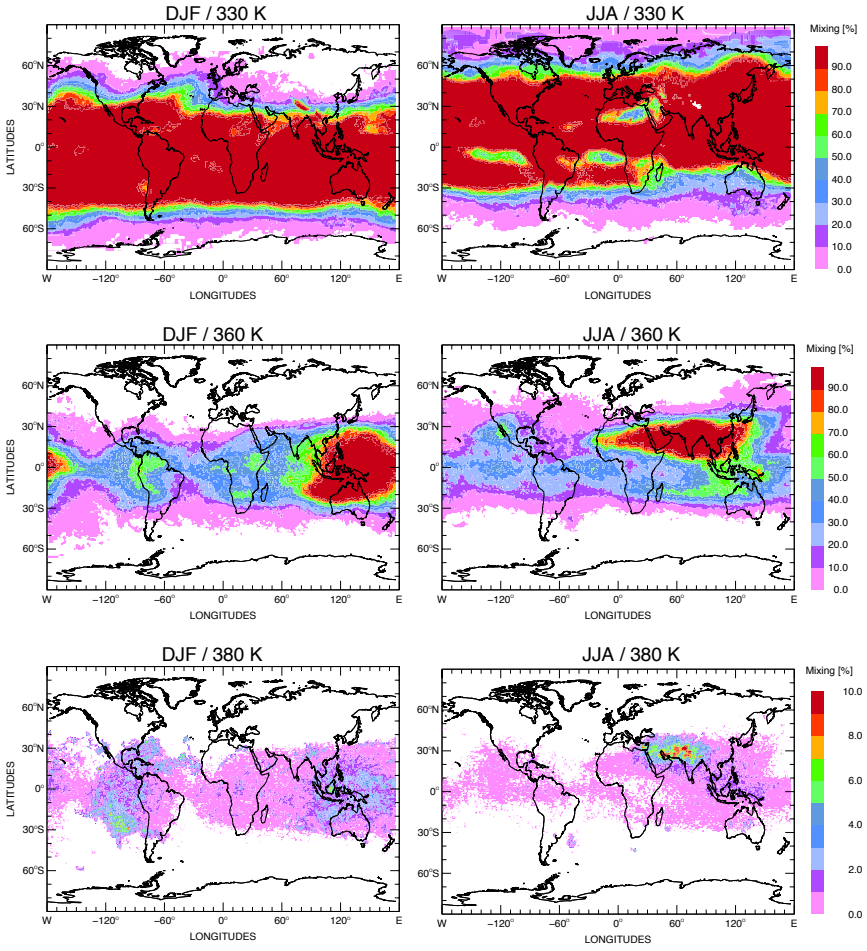

Figure 4.16: Climatology of tropospheric mixing ('state-vert') at θ= 330 K (top), θ= 360 K (middle) and θ= 380 K (bottom) in DJF (left) and in JJA (right). The intensity of tropospheric mixing is quantified as the probability (PDF) that air parcels are affected by the tropospheric mixing scheme.

intensively redistributed due to ‘tropospheric mixing’.

4.4.2 Result of tracers

We compare now the mean Age of Air (AoA) distributions between the one-year CLaMS run with deep convection and tropospheric mixing (’CLaMS-C’) and the reference run (‘CLaMS-R’) where both effects are excluded. Inserting a linear increasing artificial tracer in the lowest model layer (‘clock tracer’), AoA is quantified as the time lag between the local tracer value and the value of the ‘clock tracer’ in the boundary layer (*Hall and Plumb*, 1994).

Figure 4.17 compares the zonally averaged AoA one-year climatology of

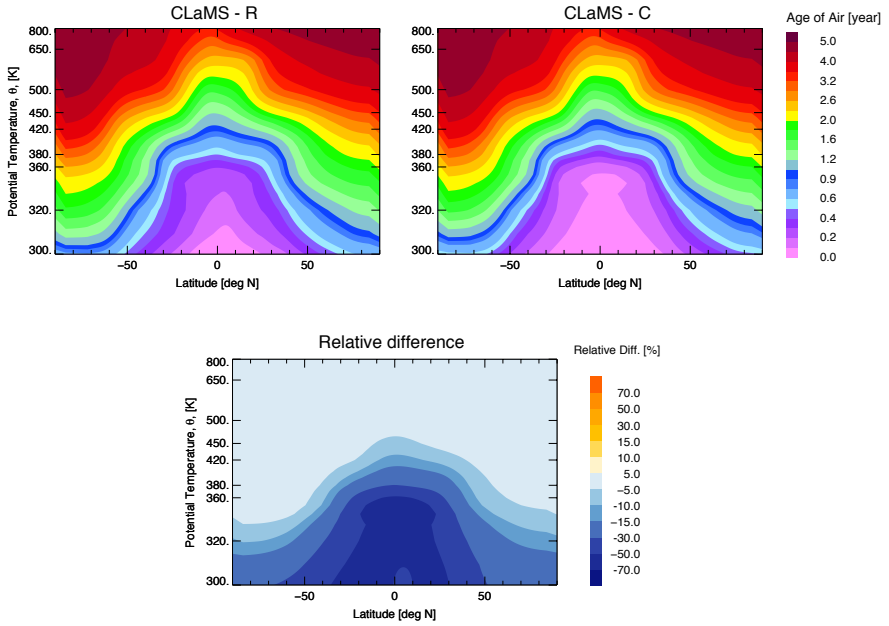

Figure 4.17: The one-year climatology of AoA distribution with CLaMS-R (reference, top left), CLaMS-C (full mixing, top right) and the relative differences between CLaMS-C and CLaMS-R ((CLaMS-C- CLaMS-R)/ CLaMS-R) (bottom).

CLaMS-R (top left) and CLaMS-C (top right). The relative differences of

AoA between CLaMS-R and CLaMS-C ((CLaMS-C- CLaMS-R)/ CLaMS-R) are shown in the bottom panel. Clearly, the AoA in CLaMS-C significantly decreases in the troposphere compared with CLaMS-R. The differences in AoA maximize in the tropical troposphere and also extend to the subtropics and even high latitudes in the lower troposphere. It is worth noting that up to the TTL ($\sim$380 K), the tropical air stays younger in CLaMS-C than in CLaMS-R despite the fact that the effect of tropospheric mixing is weak around $\theta = 380$ K (see Figure 4.16).

Therefore, we further look into the AoA distribution on $\theta = 380$ K in June and December, respectively. Figure. 4.18 shows the monthly mean AoA at θ=

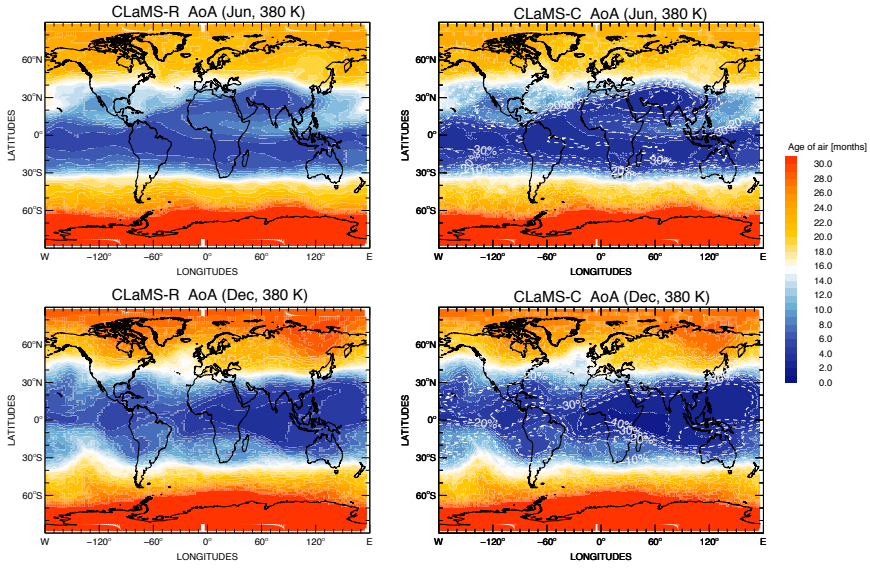

Figure 4.18: Monthly mean AoA at $\theta = 380$ K for CLaMS-R (left) and CLaMS-C (right) in June (top) and December (bottom). The relative differences of CLaMS-C to CLaMS-R up to -10%, -20% -30% and -40% (CLaMS-C < CLaMS-R) are shown as the white dashed contours.

380 K with CLaMS-R (left) and with CLaMS-C (right). The overplotted white contours quantify the differences relative to the reference run (CLaMS-R). In June, younger air covers all the longitudes from 30°S to 40°N , in particular

in the Asian Monsoon region centering at the south Asia and Tibetan Plateau where also the convective activity is most intensive during summer as shown in Fig. 4.15 and Fig. 4.16. The youngest air is found over the Asia monsoon region where the relative differences reach the maximum of ∼40%. In December, the younger air (the relative difference larger than 10%) covers also the whole tropics from 30°S to 30°N. The maximum of younger air moves to the Maritime Continent, corresponding to the active convection in this region during the boreal winter.

The distribution of CO shares some similarity with the distribution of the AoA because their sources are both in the lower boundary. Figure 4.19 shows

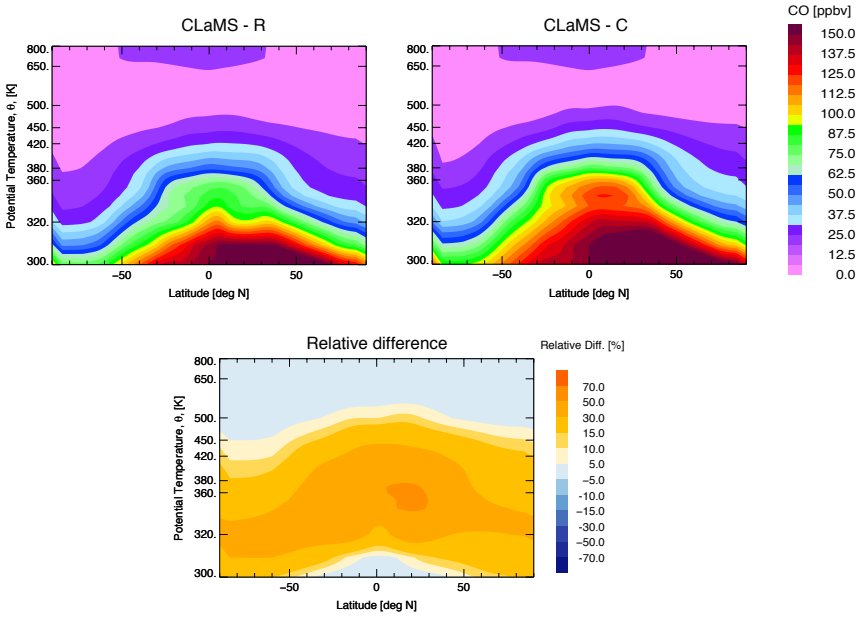

Figure 4.19: Same as Fig. 4.17 but for CO.

the climatological distribution of CO for the two runs, respectively. We see that the mixing ratios of CO significantly increase in the troposphere and 30%-40% relative difference to CLaMS-R basically follows the tropopause (bottom in Fig. 4.19). The increase of CO also extends to the lower stratosphere, which reaches $\theta = 500$ K in the tropics. The highest relative differences is located in

the TTL. Note that a maximum of relative difference is found at 20°N around the tropopause in the bottom panel of Fig. 4.19, which is mainly attributed to the

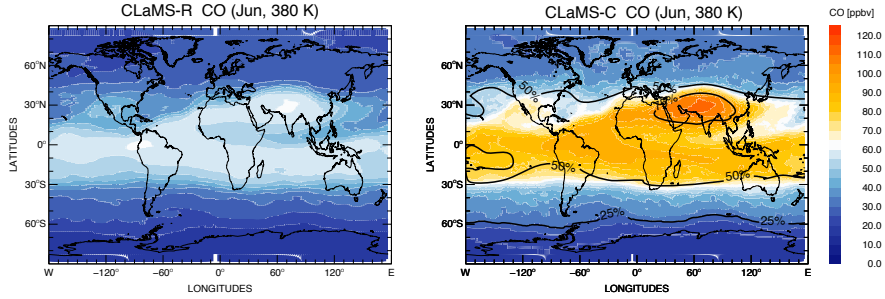

Figure 4.20: Same as Fig. 4.18 but for CO. The relative differences up to 25%, 50% and 75% are shown as the black contours.

increase of CO over the Asian monsoon region during the boreal summer shown in Figure 4.20 .

To obtain a regionally-resolved view of the increase of CO due to enhanced tropospheric transport, Fig. 4.20 shows the climatology at θ=380 K in June. We find that the differences in CO from the two runs are pronounced at $\theta = 380$ K. The gradients of CO with CLaMS-C around 35°N and 30°S are enhanced compared with CO with CLaMS-R. The pattern of CO increase shown as the black contours is similar to the relative difference of AoA shown in Fig. 4.18. Because the vertical gradient of CO is larger than that of AoA around the tropopause, the values of CO increase is much larger than the AoA decrease. Except for the South of 60°S, the relative increase of CO is higher than 25%. The increase of CO up to 50% covers the tropics, which is most intensive over Asian monsoon region centering in the Tibetan Plateau ($\sim$75%).

Figure. 4.21 quantifies the differences between the reference and the extended mixing by using ozone as a stratospheric tracer. It is seen that ozone overall decreases in the troposphere. The decrease of O_3 mixing ratio with CLaMS-C is more intensive in the TTL and in the subtropical lower troposphere. Therefore, the decrease of O_3 is a combined result of the convective transport and extended mixing.

Figure. 4.22 shows the horizontal distribution of O_3 in June. The decrease of O_3 is similar as the pattern of CO increase in June, although the relative difference is smaller than that of CO. The most pronounced decrease of O_3 also

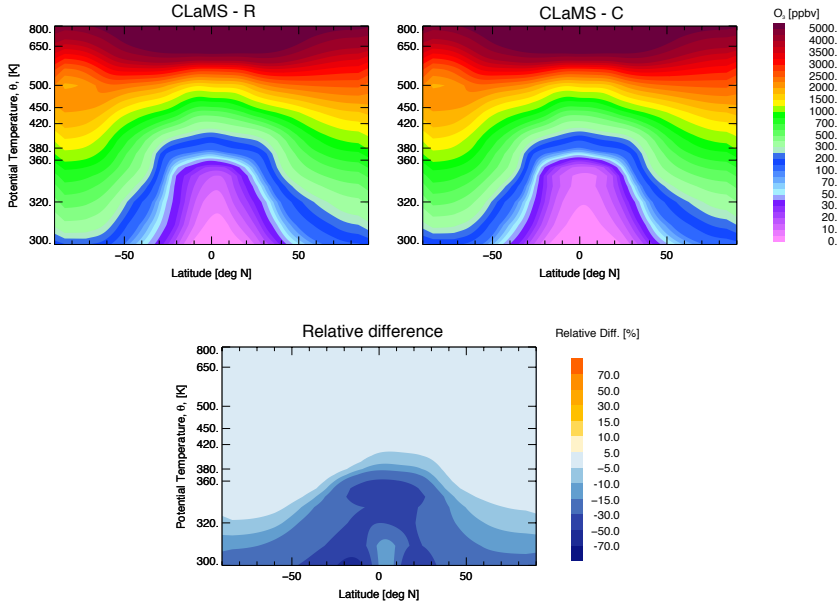

Figure 4.21: Same as Fig. 4.17 but for O_3.

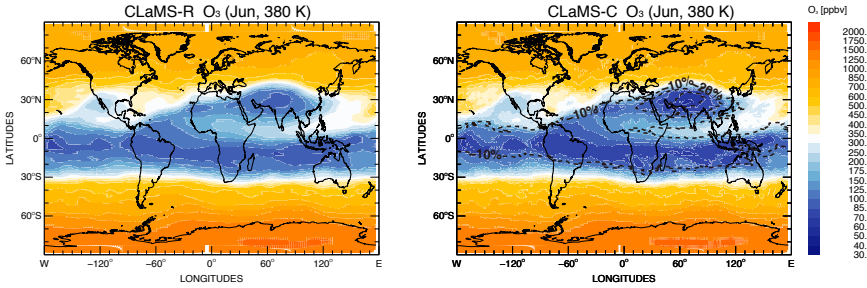

Figure 4.22: Same as Fig. 4.18 but for O_3 only in June. The relative differences up to -10%, -20% and -30% are shown as the black dashed contours.

occurs again over Asian monsoon region and maximum relative difference is up to 30%.

4.4.3 Comparison with in-situ measurements

Finally, the CLaMS run with 'deep convection' and 'tropospheric mixing' was extended to the period of the TROCCINOX campaign in 2005. We again compare the new simulation results for CO and O_3 with the in-situ measurements on 4 February 2005 when a severe convective event was captured during the flight. Figure 4.23 shows the comparison in the same way as shown in Fig. 4.2. It is

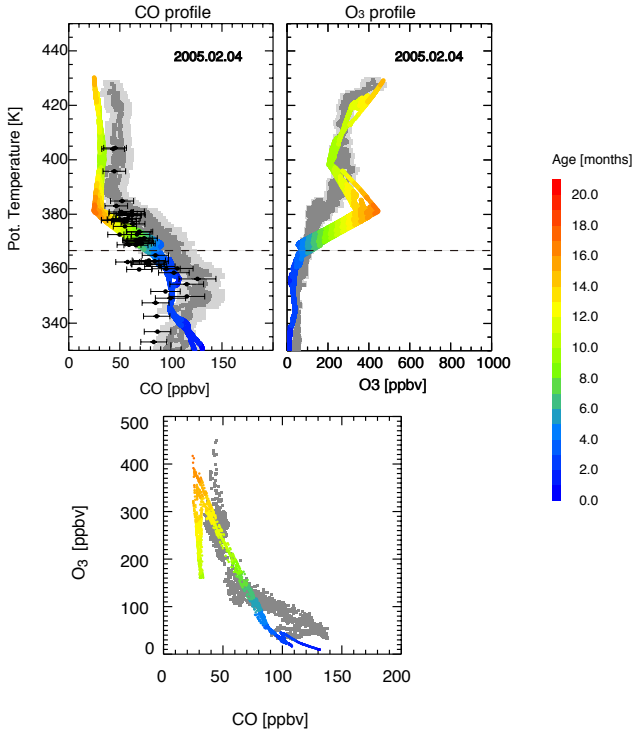

Figure 4.23: The same as Fig. 4.2 but shows the results of with the CLaMS run with 'deep convection' and 'tropospheric mixing' implemented (CLaMS-C).

shown that a better agreement of CO between the simulation and the measurements (both COLD measurement and HAGAR measurement of CO (*Pommrich et al.*, 2014)) is archieved especially from 350 K to 370 K than the CLaMS-R

simulation shown in Fig 4.2. The simulated CO values are within the uncertainty of the HAGAR measurements above 340 K in the plot and the overestimation below 340 K is likely because of the artificially doubled CO lower boundary in the model (section 4.1). At the same time, the simulated CO is getting close to the COLD measurements than the previous simulation. This indicates that implementing of 'deep convection' and 'tropospheric mixing' improved the CLaMS simulation. Furthermore, although the simulated O_3 values are still overestimated between 370 K and 400 K, the maximum value in this vertical range is reduced by 100 ppbv compared to the simulated O_3 profile in Fig. 4.2 that reached almost 600 ppbv at 390 K. Consistently, the correlation between CO and O_3 in the bottom of Fig. 4.23 illustrates a better quantification of mixing between stratospheric and tropospheric air compared with the correlation shown in Fig. 4.2.

4.5 Summary and remarks

The aim of this chapter was to improve the representation of transport in the troposphere due to unresolved convection and vertical mixing. For this purpose, the moist Brunt-Väisälä frequency N_m^2 was chosen as a new parameter to identify the regions which have some potential for both convection and tropospheric mixing. Using N_m^2, the transport scheme was extended. The respective simulation results of AoA, CO and O_3 were shown and were compared with the current version of CLaMS. Our new results including the convective scheme showed a reasonable representation of convective patterns in the lower troposphere. The extension of the mixing scheme increased the tropospheric mixing in the troposphere and at the same time enhanced the STE in the UTLS region through interaction with the mixing driven by the wind shear.

The extension of the transport scheme can be further improved by optimizing the criteria for convective instability, which will be done in the future by comparison with more in-situ measurements. Especially, up to now we only use N_m^2 in the lowest model level for triggering the parametrization of unresolved convection, which could be improved by replacing this quantity by an integral over all negative values of N_m^2 as well as by using the well-established CAPE parameter. Furthermore, since the extension of mixing is based on the next neighbors diagnosed by Delaunay triangulation within each layer, the performance of tropospheric mixing could be improved when the real neighbors (i.e. across the boundaries of the layers) are taken into account. Last but not least, although we

strictly restricted the modification to the trajectory, the mass conservation and the current mixing scheme are also affected by our new approach and need further investigations.

Chapter 5

Summary and outlook

5.1 Summary

Atmospheric mixing as the irreversible part of transport at the molecular scale is driven by eddies and turbulence at larger scales. In this sense, the energy driving atmospheric mixing is supplied by the large-scale dynamical and thermal processes, like strong wind shear in the vicinity of the jets or by the convection due to some instabilities. Since understanding of mixing is a prerequisite for quantification of the stratosphere-troposphere exchange (STE) or of the halogen-induced ozone loss in the winter polar stratosphere, a physics-based numerical representation of mixing in the model is required for the atmospheric transport models.

As an important but uncertain piece of atmospheric modeling, mixing in the transport models based on the Eulerian approach is strongly distorted by the ubiquitous numerical diffusion. The Lagrangian view provides possibilities of explicitly describing the physical mixing through parametrization along Lagrangian trajectories. The mixing parametrization implemented in CLaMS so far is triggered by strong flow deformations mainly driven by the vertical and horizontal shear of the wind and is suitable in the strongly stratified parts of the atmosphere like the stratosphere or large parts of the upper troposphere. However, mixing in the unstable parts of the atmosphere like convection in the troposphere is still not represented in CLaMS. On the path to such a re-examination of mixing in CLaMS, we had taken the following steps:

- One of the greatest challenges for understanding of stratospheric trans-

port and chemistry is the modeling of the Sudden Stratospheric Warmings (SSWs). To reexamine transport, especially mixing as implemented in CLaMS, a remarkable major SSW in January 2009 was simulated with the standard version of CLaMS. The distribution of simulated mixing intensity manifests that mixing across the vortex edge and also across the subtropical barrier (above 700 K) was enhanced after the onset of the major SSW. Moreover, the evolution of the mixing intensity during the SSW is associated with enhanced wave forcing, quantified in terms of the EP flux divergence (for more details see *Tao et al.*, 2015a).

- The simulation of the full-chemistry CLaMS run shows a good agreement with O_3 and N_2O measured by MLS during the major SSW with a disturbed dynamical background. Analyzing the MLS- and CLaMS- based O_3-N_2O correlations, we found that although a general good agreement is achieved for the simulated and observed O_3-N_2O correlations, the O_3-N_2O correlations based on MLS satellite data have a limitation in interpretation of mixing due to the poor vertical spatial resolution. (for more details see *Tao et al.*, 2015a).

- The isentropic mixing is a key process to understand the drastic change of stratospheric composition triggered by the major SSW: the decay of the polar O_3–N_2O correlation and the strengthening of the mid-latitude correlation. One month after the major SSW, almost half of the polar vortex correlation dissolved due to isentropic mixing, whereas the other part constituted the germ for the formation of a new and relatively weak vortex. The dominant ozone chemistry during and after the major SSW was the extra-tropical ozone loss due to NO_x catalytic cycles mainly at 600–800 K and ozone production in the tropics (for more details see *Tao et al.*, 2015a).

- Motivated by the intensive subseasonal variability of stratospheric composition and dynamics during the major SSW case study, especially the accelerated polar descent and tropical upwelling, the impact of SSWs on the variability of the water vapor in the tropical lower stratosphere was studied based on a CLaMS 35-year run and MLS observation. A clear dehydration of air entering the tropical stratosphere was diagnosed after SSWs, which starts at the tropical tropopause and propagates upward during the following 2-3 months (for more details see *Tao et al.*, 2015b).

- The SSW-associated dehydration effect in the tropical lower stratosphere is modulated by the two QBO phases. In the eQBO phase, a distinct cooling and a subsequent drying at the tropical tropopause by $\sim$0.3 ppmv results from enhanced breaking of planetary waves in the subtropics. In the wQBO phase, this drying effect is also present, but smaller and more uniformly distributed over time. Moreover, the MW-induced tropical upwelling is stronger in the eQBO than in the wQBO phase and results in a faster upward transport of the dehydrated air masses (for more details see *Tao et al.*, 2015b).

- The 10-year differences of H_2O anomalies among 1980s, 1990s and 2000s imply that extra-dehydration due to SSWs as well as the decadal variations of SSW frequency has potentially contributed to the long-term variability of water vapor in the lower stratosphere. Moreover, although the MW itself is confined to boreal winter, the SSW-associated extra-dehydration effect can last longer than 4 months with less in-mixing from higher latitudes due to faster upwelling (for more details see *Tao et al.*, 2015a).

- The CLaMS transport scheme was improved by including the effects of instability and the related convection. Using the moist Brunt-Väisälä Frequency as a new parameter to identify the instabilities, an extension of the transport scheme of CLaMS is proposed. This extension includes tropospheric mixing in the atmospheric regions where instabilities are identified and a new parameterization of the unresolved (deep) convection.

- The proposed extension of the transport scheme was used for a first, one-year simulations. The results show a reasonable representation of convective patterns in the middle and upper troposphere. The extension of the mixing scheme increases mixing in the troposphere and at the same time enhances the STE in the UTLS region.

5.2 Future work

The results of this thesis put forward several open questions which call for further research. Some interesting topics to be explored in the future include:

- To quantify the contributions of SSW-associated dehydration to the variability of stratospheric H_2O.

- To investigate other sources of variability of stratospheric water vapor trends e.g. El Niño Southern Oscillation (ENSO).
- To optimize and to validate the extension of the transport scheme (tropospheric mixing and deep convection).

Appendix A

Appendix

A.1 MLS averaging kernels

As discussed in subsection 2.3.3, the MLS averaging kernels were applied for both the N_2O and O_3 CLaMS output before comparing these distributions with the satellite-based observations. Given a "true" atmospheric profile x_i on n pressure levels $i = 1, \ldots, n$, the averaging kernel can be understood as a smoothing procedure that determines mixing ratios at each level i by a weighted integration over all other levels with a strongest contribution of levels directly above or below the considered level i. The averaging kernel is a matrix A_{ij} with most significant terms around the diagonal and with all rows i fulfilling the normalization condition $\sum_{j=1,\ldots,n} A_{ij} = 1$. Thus, applying averaging kernels to model data with a high spatial resolution like CLaMS means smoothing or removing small-scale structure from the model.

In Fig. A.1, the PDFs of the N_2O-O_3 correlations are exemplary shown for February, 15th, 2009 as observed by the MLS instrument (top) and as derived from CLaMS simulations with and without smoothing by the averaging kernel (bottom). In contrast to MLS, original CLaMS output shows the polar correlation and that also disappears if the averaging kernel is applied to CLaMS output. This polar correlation can be attributed to some remnants of the polar vortex which are resolved by CLaMS. Within the model, the lifetime of the polar correlation is about three weeks longer compared to the last time this correlation was detected by the MLS instrument.

Thus, two question arise: are these small-scale structures resolved with CLaMS realistic and is the N_2O or rather the O_3-related coarse sampling of the MLS instrument that smoothes out the polar correlation of N_2O-O_3? To get an impression, how the averaging kernel smoothes out the modeled small scale filaments and tracer gradients, Fig. A.2 shows the spatial distribution of N_2O vortex remnants on February, 20th, 2009 before and after applying the MLS averaging kernel procedure (right and left column,

respectively). Here, N_2O distributions at two isentropic levels, 550 K (top row) and 650 K (bottom row) are shown, with black line denoting the strongly disturbed vortex edge.

Complementary, N_2O and O_3 profiles from the Atmospheric Chemistry Experiment (ACE) are used, which cross the potential surfaces $\theta = 550$ and 660 K at this day (red circles as the profile positions at noon on each isentrope), as well as the corresponding CLaMS profiles before and after applying the averaging kernel. The nearest CLaMS APs are selected according to the same procedure as for the MLS data (see subsection 2.3.3). Thus, the horizontal spatial distances of ACE profiles and corresponding CLaMS profiles are less than 50 km (1.5°). The vertical resolution of ACE profiles is about 3-4 km (*Bernath et al.*, 2005; *Boone et al.*, 2005).

It can be seen that the vertical variability of the untreated CLaMS simulation of N_2O is confirmed by the corresponding ACE profile (top panel in Fig. A.3). On the other hand, this variability is removed from the CLaMS simulation if the MLS averaging kernel is applied and, consequently, the comparison with the ACE observations becomes worse. However, the smoothing does not significantly change the O_3 profiles (bottom panel in Fig. A.3). This is mainly because the vertical variability of O_3 is much smaller if compared with the N_2O profile and not because of a higher vertical resolution of the MLS-based O_3 observations (i.e. 2.5-3 km for O_3 versus 5-6 km for N_2O).

This can also be inferred from the comparison of the horizontal and vertical gradients of both tracers. Within the vertical range between $\theta = 400$ and 800 K, the horizontal variability of N_2O across the vortex edge ($\sim$100 ppbv) is comparable with the vertical variability ($\sim$150 ppbv), whereas O_3 gradient across polar vortex edge (around 1$\sim$2 ppmv) is much smaller than its vertical gradient in stratosphere ($\sim$5 ppmv). Therefore, the filaments or vortex remnants which are not completely mixed, contribute to a more pronounced vertical variability of N_2O than of the O_3 profiles.

A.2 Monte Carlo difference test in composite analysis

In the composite analysis, we use Monte Carlo simulations to test whether two sample populations (winters with MWs and winter without MWs) have significant different mean. Due to the small number of samples (under 10 of each sample population), the distribution of each population stays unknown. Monte Carlo (MC) test can be applied without any assumption on the distribution of samples.

We hypothesize that the mean values of population A (winters with MWs) and population B (winter without MWs) have no significant difference (the null hypothesis: H_0). Following steps are done to do the MC test:

- Calculate the mean difference between population A (N samples) and population B (M samples);

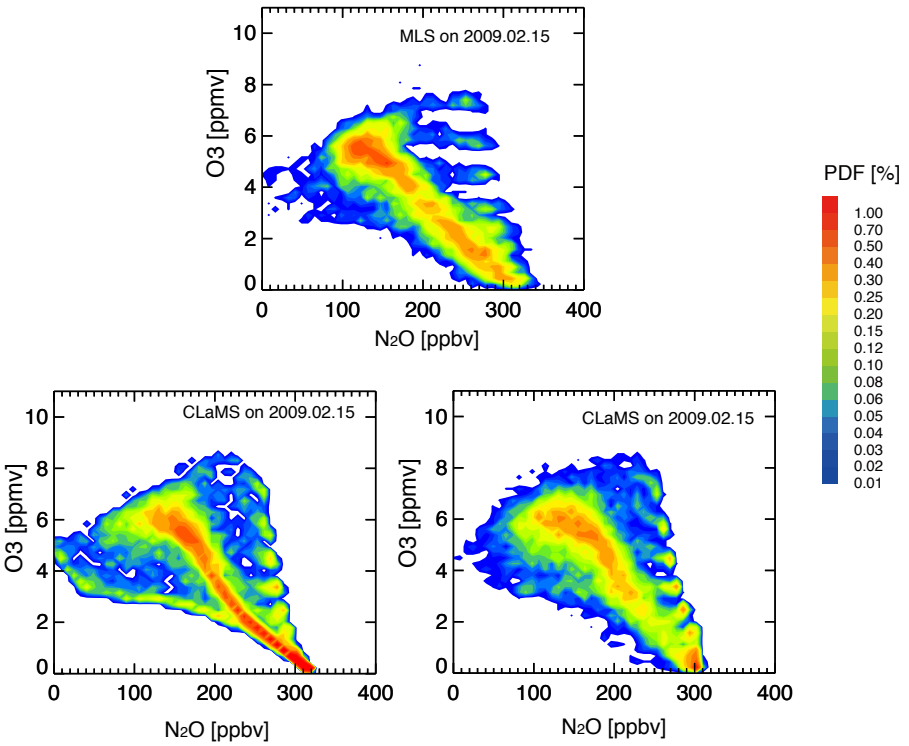

Figure A.1: PDFs of N_2O-O_3 correlations on February, 15th, 2009 from MLS observations (top); from the reference CLaMS simulation without applying the averaging kernel (bottom left) and after applying the averaging kernel (bottom right).

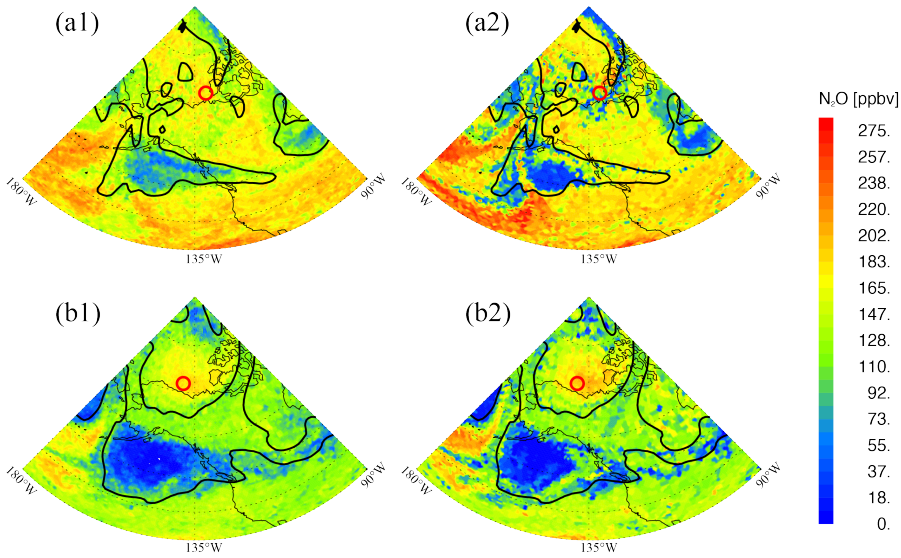

Figure A.2: Spatial distribution of N_2O on February, 20th, 2009, i.e., almost 1 month after the MW at $\theta = 550$ K (top row) and 650 K (bottom row). Here the results of the reference run with and without the averaging kernel are shown in the left and right column, respectively. Black line is vortex edge, the red circles are the noon-footprints calculated by the observed ACE profile through back and forward trajectory.

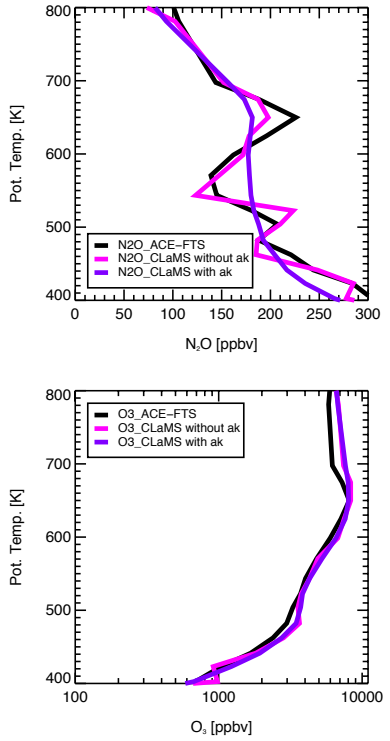

Figure A.3: N_2O (top) and O_3 (bottom) profiles of ACE observations (black) on Feb. 20th located at 73.05°N, 137.11°W at 30 km and of corresponding CLaMS simulation before (blue) and after (purple) applying the MLS averaging kernel.

- Mix all the samples of population A and population B to get one sample-pool (N+M samples);

- Randomly select N samples from the mixed sample-pool as a random population A_1 and then the remaining M samples form a random population B_1. Calculate the mean difference between population A_1 and B_1 to get one random mean difference.

- Repeat step 3 for a large number of times (10000 times in our study). Then we get a large number of random mean differences between two random populations.

- Rank the mean difference between population A and B in all the random mean differences. Given a significant level $n\%$, if it is ranked in the top $(100-n)\%$ or in the bottom $(100-n)\%$, we refuse H_0. Otherwise, we accept H_0.

We also tried classic Student's t-test for Figure 3 (c1/c2) in the paper. And Figure A.4 show the same plot as Figure 3 (c1/c2) using t-test with the statistical confidence above 0.95. We can see the area passed the significant test is very similar as the result using MC test. Moreover, it is easier to pass the t-test than to pass the MC test on the same confidence level. Therefore, we conclude that independent from the methodologies of significant test, the dehydration effect of MW based on our composite analysis is significant.

A.3 CLAUS dataset

The brightness temperature (T_b) used in the study is provided by Cloud Archive User Service (CLAUS) project. The CLAUS project was co-ordinated by Environmental Systems Science Centre (ESSC) and involved all of the major climate modeling groups in Europe. The project was supported by the European Union under the IVth Framework Programme (Environment and Climate) and ran from April 1997 to December 1999.

The CLAUS project produces a long-term global thermal infrared window (10.5-12.5μm) imagery of the Earth, which spans the period 1st July 1983 - 30th June 2009. The source data of CLAUS project are the ISCCP intermediate level B3 (reduced resolution radiance data) products from four operational meteorological geostationary and two polar orbiting meteorological satellites participating in the International Satellite Cloud Climatology Project (ISCCP). Table A.1 lists the information of the satellites involved.

Two steps are implemented to produce CLAUS T_b achieve from the ISCCP B3 source data: an initial spatial interpolation and a following temporal interpolation to fill in the voids of spatial interpolated images. The CLAUS achieve includes T_b, contributing satellites and interpolation quality, with a temporal resolution of 3 hour and two

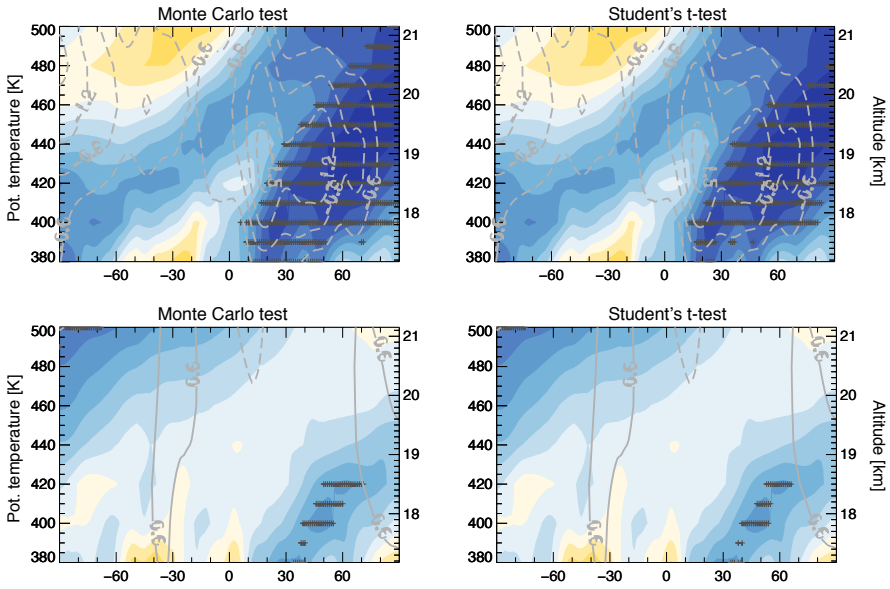

Figure A.4: The left panel is Figure 3 (c1/c2); the right panel is the same as the left panel but using student's t-test with statistical confidence level 0.05

Satellite	Series	Agency	Longtitude
NOAA Morning (AM)	8,10,12	NOAA	–
NOAA Afternoon (PM)	7,9,11,14	NOAA	–
GOES-EAST	5,7,8	NOAA	75°W
GOES-WEST	6,7,9	NOAA	135°W
GMS	1,2,3,4,5	JMA	140°E
METEOSAT	3,4,5	ESA	0°

Table A.1: The information of contributing satellites in CLAUS.

spatial resolutions of 1/2°and 1/3°respectively. The dataset with 1/3°resolution is used in our study. The accuracy of CLAUS T_b values are determined by many factors, which mainly refer to limb darkening, temporal mismatch, differential absorption by water vapor, calibration errors and sampling characteristics of satellites and interpolation errors. The overall averaged error is estimated to be $\sim$3-4 K.

Campaign	Date	Base Location	Platform	Instrument (O_3)	Instrument (CO)
TROCCINOX	Jan.-Mar. 2005	Aracatuba Brazil	Geophysica	FOZAN	COLD HAGAR
SCOUT	Nov.-Dec. 2005	Darwin Australia	Geophysica	FOZAN	COLD
AMMA	Jul.- Aug. 2006	Ouagadougou Burkina Faso	Geophysica	FOZAN	COLD
START08	Apr.- Jun. 2008	North America	Hiaper	Fast-O_3 NCAR	RAF NCAR

Table A.2: The information about the in-situ measurements of CO and O_3 during four campaigns from 2005 to 2008 used in chapter 4.

A.4 In-situ measurements

The in-situ measurements of CO and O_3 used in chapter 4 were sampled with the measurements from four campaigns. The information, including platforms and instruments measuring CO and O_3 are listed in Table A.2 as well as following.

- TROCCINOX

  The Tropical Convection, Cirrus and Nitrogen Oxides (TROCCINOX) experiment took place in early 2005 over southern Brazil (21.2°S, 50.4°W). Chemical species were measured on-board the high-altitude research aircraft Geophysica in the altitude range up to 20 km. CO was measured by COLD (*Viciani et al.*, 2008) and HAGAR (*Volk et al.*, 2000; *Homan et al.*, 2010) and O_3 was measured by FOZAN (*Yushkov et al.*, 1982). More details about the campaign can be found in *Konopka et al.* (2007).

- SCOUT

  The Stratospheric- Climate Links with Emphasis on the Upper Troposphere and Lower Stratosphere (SCOUT) campaign took place over Darwin, Australia (12.47°S, 130.85°E), from November 2005 to December 2005. More details about the campaign was overviewed in *Vaughan et al.* (2008).

- AMMA

  African Monsoon Multidisciplinary Analysis (AMMA) aircraft campaign took place in July/August 2006 and was based in Ouagadougou, Burkina Faso, measuring the chemical species from the boundary layer up to the stratosphere. More details about the campaign was documented by *Cairo et al.* (2010).

- START08

  The Stratosphere Troposphere Analyses of Regional Transport 2008 (START08) was conducted during April- June 2008, which covers the central North America (25°-65°N, 80°-120°W) and altitudes from the surface to ∼14.3 km. In this

work, we used the CO measurements by VUV resonance fluorescence and O_3 measurements by the NOAA Earth System Research Laboratory (ESRL) dual-beam UV-absorption ozone photometer (*Proffitt and McLaughlin*, 1983). More details about the campaign was overviewed by *Pan et al.* (2010).

A.5 Equivalent potential temperature

When an (unsaturated) air parcel moving vertically, its temperature will change along with pressure through expanding or compressing while its entropy s is constant during an adiabatic process (second law of thermodynamics). The concept of potential temperature arises from the demand of a conservation 'temperature like' property for adiabatic processes. Therefore, the potential temperature θ is derived from the definition of entropy s as:

$$\theta := \theta_0 exp(\frac{s}{c_p}) \tag{A.1}$$

where c_p denoting the specific heat capacity at a constant pressure and θ_0 being the temperature T_0 that the air parcel would acquire if adiabatically brought to a standard reference pressure p_0 (typically set to 1013.25 hPa that is the mean air pressure at sea level).

The (dry) potential temperature θ can also be written as the well-known textbook formula:

$$\theta = T(\frac{p_0}{p})^{R/c_p} \tag{A.2}$$

where R is the gas constant of air. Then under dry adiabatic assumption (with s =constant and no phase transition), the eq. A.1 can be rewritten as:

$$s = c_p ln(\frac{\theta}{\theta_0}) \tag{A.3}$$

and through differenctiation, we obtain:

$$ds = c_p \frac{d\theta}{\theta} \tag{A.4}$$

The total differential of the entropy density $s(T,P)$ with respect to T and p is given through

$$ds = (\frac{\partial s}{\partial T})_p dT + (\frac{\partial s}{\partial p})_T dp. \tag{A.5}$$

Using the definition of c_p i.e. $(\partial s/\partial T)_p = c_p/T$, Maxwell's relation $(\partial s/\partial p)_T = -(\partial v/\partial T)_p$ with v denoting the molar volume of the fluid and ideal gas equation $p =$

$(1/v)RT$, eq. A.5 can be rewritten as:

$$ds = c_p \frac{dT}{T} - R\frac{dp}{p}. \tag{A.6}$$

Combining eq.A.4 and A.6 yields

$$\frac{d\theta}{\theta} = \frac{dT}{T} - \frac{R}{c_p}\frac{dp}{p}. \tag{A.7}$$

By integrating eq A.7 from the state (T_0, p_0) to the state(T,p), i.e. from $\theta_0 = T_0$ to θ, we obtain:

$$ln\frac{\theta}{T_0} = ln\frac{T}{T_0} - \frac{R}{c_p}ln\frac{p}{p_0} = ln[\frac{T}{T_0}(\frac{p_0}{p})^{R/c_p}], \tag{A.8}$$

i.e. relation in eq. A.2. Note that our discussion is not confined to a dry atmosphere, i.e. the constants R and c_p depends on the amount of water vapor in the considered air parcel. In a dry atmosphere, we get $R = 287.1$ J/(kg· mol)and $c_p = 1004$J(kg· K) with $R/c_p = 0.286$.

The generalization of this concept to processes where phase transitions and contributions of latent heat are relevant, the equivalent potential temperature θ_e is used which is defined as:

$$\theta_e = T_e(\frac{p_0}{p})^{R/c_p} = \frac{T_e}{T}\theta \tag{A.9}$$

where equivalent temperature T_e is the temperature of an air parcel from which all the water vapor has been extracted by a reversible pseudoadiabatic process as:

$$T_e = T + \frac{L}{c_p}\mu_w. \tag{A.10}$$

L is the latent heat of evaporation and μ_w is the water vapor mixing ratio. Accordingly, the processes with

$$s_e = c_p ln(\frac{\theta_e}{\theta_0}) = const \tag{A.11}$$

are entropy- conserving transport and phase-transition processes. Such processes may occur both quasi-horizontally (e.g. warm conveyor belts with air masses sliding on almost horizontal surfaces with $\theta_e = $ const) or vertically (e.g. convections, also characterized by $\theta_e = $ const).

Bibliography

Andrews, D. G., J. R. Holton, and C. B. Leovy (1987), *Middle Atmosphere Dynamics*, Academic Press, San Diego, USA.

Arakawa, A. (2004), The cumulus parameterization problem: Past, present, and future, *Journal of Climate*, *17*(13), 2493–2525.

Ayarzagüena, B., U. Langematz, and E. Serrano (2011), Tropospheric forcing of the stratosphere: A comparative study of the two different major stratospheric warmings in 2009 and 2010, *J. Geophys. Res. A*, *116*.

Baldwin, M., L. Gray, T. Dunkerton, K. Hamilton, P. Haynes, W. Randel, J. Holton, M. Alexander, I. Hirota, T. Horinouchi, et al. (2001), The quasi-biennial oscillation, *Reviews of Geophysics*, *39*(2), 179–229.

Balluch, M. G., and P. H. Haynes (1997), Quantification of lower stratospheric mixing processes using aircraft data, *J. Geophys. Res.*, *102*, 23,487–23,504.

Batchelor, G. K. (1953), *The Theory of Homogeneous Turbulence*, Cambridge Science Classics, New York.

Bernath, P., C. McElroy, M. Abrams, C. Boone, M. Butler, C. Camy-Peyret, M. Carleer, C. Clerbaux, P. Coheur, R. Colin, P. DeCola, P. Bernath, C. McElroy, M. Abrams, C. Boone, M. Butler, C. Camy-Peyret, M. Carleer, C. Clerbaux, P. Coheur, R. Colin, P. DeCola, M. DeMaziere, J. Drummond, D. Dufour, W. Evans, H. Fast, D. Fussen, K. Gilbert, D. Jennings, E. Llewellyn, R. Lowe, E. Mahieu, J. McConnell, M. McHugh, S. McLeod, R. Michaud, C. Midwinter, R. Nassar, F. Nichitiu, C. Nowlan, C. Rinsland, Y. Rochon, N. Rowlands, K. Semeniuk, P. Simon, R. Skelton, J. Sloan, M. Soucy, K. Strong, P. Tremblay, D. Turnbull, K. Walker, I. Walkty, D. Wardle, V. Wehrle, R. Zander, and J. Zou (2005), Atmospheric Chemistry Experiment (ACE): Mission overview, *Geophys. Res. Lett.*, *32*(15), doi: 10.1029/2005GL022386.

Birner, T., D. Sankey, and T. G. Shepherd (2006), The tropopause inversion layer in models and analyses, *Geophys. Res. Lett.*, *33*(L14804).

Bönisch, H., A. Engel, T. Birner, P. Hoor, D. W. Tarasick, and E. A. Ray (2011), On the structural changes in the brewer-dobson circulation after 2000, *Atmos. Chem. Phys.*, *11*(8), 3937–3948.

Boone, C. D., R. Nassar, K. A. Walker, Y. Rochon, S. D. McLeod, C. P. Rinsland, and P. F. Bernath (2005), Retrievals for the atmospheric chemistry experiment fourier-transform spectrometer, *Applied optics*, *44*(33), 7218–7231.

Brewer, A. W. (1949), Evidence for a world circulation provided by the measurements of helium and water vapour distribution in the stratosphere, *Q. J. R. Meteorol. Soc.*, *75*, 351–363.

Butler, A. H., and L. M. Polvani (2011), El niño, la niña, and stratospheric sudden warmings: A reevaluation in light of the observational record, *Geophys. Res. Lett.*, *38*(13).

Butler, A. H., D. J. Seidel, S. C. Hardiman, N. Butchart, T. Birner, and A. Match (2015), Defining sudden stratospheric warmings, *Bull. Am. Meteorol. Soc.*, *96*(11), 1913–1928.

Cairo, F., J. P. Pommereau, K. S. Law, H. Schlager, A. Garnier, F. Fierli, M. Ern, M. Streibel, S. Arabas, S. Borrmann, J. J. Berthelier, C. Blom, T. Christensen, F. D'Amato, G. Di Donfrancesco, T. Deshler, A. Diedhiou, G. Durry, O. Engelsen, F. Goutail, N. R. P. Harris, E. R. T. Kerstel, S. Khaykin, P. Konopka, A. Kylling, N. Larsen, T. Lebel, X. Liu, A. R. MacKenzie, J. Nielsen, A. Oulanowski, D. J. Parker, J. Pelon, J. Polcher, J. A. Pyle, F. Ravegnani, E. D. Rivière, A. D. Robinson, T. Röckmann, C. Schiller, F. Simões, L. Stefanutti, F. Stroh, L. Some, P. Siegmund, N. Sitnikov, J. P. Vernier, C. M. Volk, C. Voigt, M. von Hobe, S. Viciani, and V. Yushkov (2010), An introduction to the scout-amma stratospheric aircraft, balloons and sondes campaign in west africa, august 2006: rationale and roadmap, *Atmos. Chem. Phys.*, *10*(5), 2237–2256, doi:10.5194/acp-10-2237-2010.

Calvo, N., R. Garcia, W. Randel, and D. Marsh (2010), Dynamical mechanism for the increase in tropical upwelling in the lowermost tropical stratosphere during warm enso events, *J. Atmos. Sci.*, *67*(7), 2331–2340.

Chaboureau, J.-P., J.-P. Cammas, J. Duron, P. Mascart, N. Sitnikov, and H.-J. Voessing (2007), A numerical study of tropical cross-tropopause transport by convective overshoots, *Atmos. Chem. Phys.*, *7*(7), 1731–1740.

Chan, S. C., and S. Nigam (2009), Residual diagnosis of diabatic heating from era-40 and ncep reanalyses: Intercomparisons with trmm, *J. Climate*, *22*(2), 414–428.

Charlton, A. J., and L. M. Polvani (2007), A new look at stratospheric sudden warmings. part i: Climatology and modeling benchmarks, *Journal of Climate*, *20*(3), 449–469.

Charney, J. G., and P. G. Drazin (1961), Propagation of planetary-scale disturbances from the lower into the upper atmosphere, *J. Geophys. Res.*, *66*(1), 83–109, doi:10.1029/JZ066i001p00083.

Chen, G., and L. Sun (2011), Mechanisms of the tropical upwelling branch of the brewer-dobson circulation: The role of extratropical waves, *J. Atmos. Sci.*, *68*(12), 2878–2892.

Collins, W., R. Derwent, C. Johnson, and D. Stevenson (2002), A comparison of two schemes for the convective transport of chemical species in a lagrangian global chemistry model, *Q. J. R. Meteorol. Soc.*, *128*(581), 991–1009.

Courant, R., K. Friedrichs, and H. Lewy (1928), Über die partiellen Differenzengleichungen der mathematischen Physik, *Mathematische Annalen*, *100*, 32–74.

Crutzen, P. J., J.-U. Grooß, C. Brühl, R. Müller, and J. M. Russell III (1995), A reevaluation of the ozone budget with HALOE UARS data: No evidence for the ozone deficit, *Science*, *268*, 705–708.

Danielsen, E. F. (1993), In situ evidence of rapid, vertical,irreversible transport of lower tropospheric air into the lower tropical stratosphere by convective cloud turrets and by larger-scale upwelling in tropical cyclones, *J. Geophys. Res.*, *98*, 8665–8681.

Dee, D. P., S. M. Uppala, A. J. Simmons, P. Berrisford, P. Poli, S. Kobayashi, U. Andrae, M. A. Balmaseda, G. Balsamo, P. Bauer, P. Bechtold, A. C. M. Beljaars, L. van de Berg, J. Bidlot, N. Bormann, C. Delsol, R. Dragani, M. Fuentes, A. J. Geer, L. Haimberger, S. B. Healy, H. Hersbach, E. V. Holm, L. Isaksen, P. Kallberg, M. Kohler, M. Matricardi, A. P. McNally, B. M. Monge-Sanz, J. J. Morcrette, B. K. Park, C. Peubey, P. de Rosnay, C. Tavolato, J. N. Thepaut, and F. Vitart (2011), The ERA-interim reanalysis: configuration and performance of the data assimilation system, *Q. J. R. Meteorol. Soc.*, *137*, 553–597, doi:10.1002/qj.828.

Dessler, A., M. Schoeberl, T. Wang, S. Davis, and K. Rosenlof (2013), Stratospheric water vapor feedback, *Proceedings of the National Academy of Sciences*, *110*(45), 18,087–18,091.

Dickerson, R., G. Huffman, W. Luke, L. Nunnermacker, K. Pickering, A. Leslie, C. Lindsey, W. Slinn, T. Kelly, P. Daum, et al. (1987), Thunderstorms: An important mechanism in the transport of air pollutants., *Science*, *235*(4787), 460–464.

Dickinson, R. E. (1968), On the exact and approximate linear theory of vertically propagating planetary rossby waves forced at a spherical lower boundary, *Monthly Weather Review*, *96*(7), 405–415.

Dickinson, R. E. (1969), Theory of planetary wave-zonal flow interaction, *J. Atmos. Sci.*, *26*(1), 73–81.

Dobson, G. M. B. (1956), Origin and distribution of polyatomic molecules in the atmosphere, *Proc R Soc London A*, *236*, 187–193.

Dobson, G. M. B., D. N. Harrison, and J. Lawrence (1929), Measurements of the amount of ozone in the Earth's atmosphere and its relation to other geophysical conditions. part iii, *Proc. R. Soc. London A*, *122*, 456–486.

Edouard, S., B. Legras, F. Lefèvre, and R. Eymard (1996), The effect of small-scale inhomogeneities on ozone depletion in the Arctic, *Nature*, *384*, 444–447.

Eliassen, A. (1951), Slow thermally or frictionally controlled meridional circulation in a circular vortex, *Astrophysica Norvegica*, *5*, 19.

Emanuel, K. A. (1991), A scheme for representing cumulus convection in large-scale models, *J. Atmos. Sci.*, *48*, 2313 – 2335.

Ertel, H. (1938), *Methoden und Probleme der Dynamischen Meteorologie*, *Ergebnisse der Mathematik und ihrer Grenzgebiete*, vol. 5, 122 pp., Verlag von Julius Springer, Berlin, (reprint published under doi:10.1007/978-3-642-65431-2).

Evan, S., K. Rosenlof, T. Thornberry, A. Rollins, and S. Khaykin (2015), Ttl cooling and drying during the january 2013 stratospheric sudden warming, *Q. J. R. Meteorol. Soc.*

Evans, S. J., R. Toumi, J. E. Harries, M. R. Chipperfield, and J. M. Russell (1998), Trends in stratospheric humidity and the sensitivity of ozone to these trends, *J. Geophys. Res. A*, *103*(D8), 8715–8725.

Fick, A. (1855), Über Diffusion, *Poggendorf's Annalen*, *94*, 59–81.

Forster, C., A. Stohl, and P. Seibert (2007), Parameterization of convective transport in a lagrangian particle dispersion model and its evaluation, *J. Appl. Meteor. Climatol.*, *46*(4), 403–422.

Forster, P., and K. P. Shine (1999), Stratospheric water vapour change as possible contributor to observed stratospheric cooling, *Geophys. Res. Lett.*, *26*(21), 3309 – 3312, doi:10.1029/1999GL010487.

Fueglistaler, S. (2012), Stepwise changes in stratospheric water vapor?, *J. Geophys. Res. A*, *117*(D13).

Fueglistaler, S., and P. H. Haynes (2005), Control of interannual and longer-term variability of stratospheric water vapor, *J. Geophys. Res.*, *110*, doi:10.1029/2005JD006019.

Fueglistaler, S., B. Legras, A. Beljaars, J.-J. Morcrette, A. Simmons, A. M. Tompkins, and S. Uppapla (2009), The diabatic heat budget of the upper troposphere and lower-/mid stratosphere in ECMWF reanalyses, *Q. J. R. Meteorol. Soc.*, *135*, 21–37, doi:10.1002/qj.361.

Fueglistaler, S., Y. Liu, T. Flannaghan, P. Haynes, D. Dee, W. Read, E. Remsberg, L. Thomason, D. Hurst, J. Lanzante, et al. (2013), The relation between atmospheric humidity and temperature trends for stratospheric water, *J. Geophys. Res. A*, *118*(2), 1052–1074.

Garcia, R. R., and W. J. Randel (2008), Acceleration of brewer-dobson circulation due to increase in greenhouse gases, *J. Atmos. Sci.*, accepted.

Garfinkel, C. I., S. B. Feldstein, D. W. Waugh, C. Yoo, and S. Lee (2012), Observed connection between stratospheric sudden warmings and the madden-julian oscillation, *Geophys. Res. Lett.*, *39*(18).

Garny, H., M. Dameris, W. Randel, G. E. Bodeker, and R. Deckert (2011), Dynamically forced increase of tropical upwelling in the lower stratosphere, *J. Atmos. Sci.*, *68*(6), 1214–1233.

Gettelman, A., and T. Birner (2007), Insights into tropical tropopause layer processes using global models, *J. Geophys. Res. A*, *112*(D23).

Gettelman, A., W. Randel, S. Massie, F. Wu, W. Read, and J. Russell III (2001), El nino as a natural experiment for studying the tropical tropopause region, *Journal of climate*, *14*(16), 3375–3392.

Gidel, L. T. (1983), Cumulus cloud transport of transient tracers, *J. Geophys. Res. O*, *88*(C11), 6587–6599.

Gómez-Escolar, M., N. Calvo, D. Barriopedro, and S. Fueglistaler (2014), Tropical response to stratospheric sudden warmings and its modulation by the QBO, *J. Geophys. Res. A*, *119*(12), 7382–7395, doi:10.1002/2013JD020560.

Gray, S. L. (2003), A case study of stratosphere to troposphere transport: The role of convective transport and the sensitivity to model resolution, *J. Geophys. Res. A*, *108*(D18).

Grise, K. M., D. W. Thompson, and T. Birner (2010), A global survey of static stability in the stratosphere and upper troposphere, *J. Climate*, *23*(9), 2275–2292.

Grooß, J.-U., G. Günther, R. Müller, P. Konopka, S. Bausch, H. Schlager, C. Voigt, C. M. Volk, and G. C. Toon (2005), Simulation of denitrification and ozone loss for the Arctic winter 2002/2003, *Atmos. Chem. Phys.*, *5*, 1437–1448.

Grooß, J.-U., I. Engel, S. Borrmann, W. Frey, G. Günther, C. Hoyle, R. Kivi, B. Luo, S. Molleker, T. Peter, M. C. Pitts, H. Schlager, G. Stiller, H. Vömel, K. A. Walker, and R. Müller (2014), Nitric acid trihydrate nucleation and denitrification in the arctic stratosphere, *Atmos. Chem. Phys.*, *14*(2), 1055–1073.

Hall, T. M., and R. A. Plumb (1994), Age as a diagnostic of stratospheric transport, *J. Geophys. Res.*, *99*(D1), 1059–1070.

Harada, Y., A. Goto, H. Hasegawa, N. Fujikawa, H. Naoe, and T. Hirooka (2010), A major stratospheric sudden warming event in january 2009, *J. Atmos. Sci.*, *67*(6), 2052–2069.

Harries, J. E., J. M. Russell III, A. F. Tuck, L. L. Gordley, P. Purcell, K. Stone, R. M. Bevilacqua, M. Gunson, G. Nedoluha, and W. A. Traub (1996), Validation of measurements of water vapour from the Halogen Occultation Experiment HALOE, *J. Geophys. Res.*, *101*(D6), 10,205–10,216.

Haynes, P., and J. Anglade (1997), The vertical scale cascade in atmospheric tracers due to large-scale differential advection, *J. Atmos. Sci.*, *54*, 1121–1136.

Haynes, P., and E. Shuckburgh (2000), Effective diffusivity as a diagnostic of atmospheric transport, 1, Stratosphere, *J. Geophys. Res.*, *105*, 22,777–22,794.

Hegglin, M., D. Plummer, T. Shepherd, J. Scinocca, J. Anderson, L. Froidevaux, B. Funke, D. Hurst, A. Rozanov, J. Urban, et al. (2014), Vertical structure of stratospheric water vapour trends derived from merged satellite data, *Nature Geoscience*, *7*(10), 768–776.

Hegglin, M. I., and T. G. Shepherd (2007), O_3-n_2o correlations from the Atmospheric Chemistry Experiment: Revisiting a diagnostic of transport and chemistry in the stratosphere, *J. Geophys. Res.*, *112*(D19), D19301, doi:10.1029/2006JD008281.

Hegglin, M. I., D. Brunner, H. Wernli, C. Schwierz, O. Martius, P. Hoor, H. Fischer, N. Spelten, C. Schiller, M. Krebsbach, U. Parchatka, U. Weers, J. Staehelin, and T. Peter (2004), Tracing troposphere-to-stratosphere transport above a mid-latitude deep convective system, *Atmos. Chem. Phys.*, *4*, 169–206.

Hitchcock, P., and T. G. Shepherd (2013), Zonal-mean dynamics of extended recoveries from stratospheric sudden warmings, *J. Atmos. Sci.*, *70*(2), 688–707.

Hobe, M. v., J.-U. Grooß, G. Günther, P. Konopka, I. Gensch, M. Krämer, N. Spelten, A. Afchine, C. Schiller, A. Ulanovsky, et al. (2011), Evidence for heterogeneous chlorine activation in the tropical utls, *Atmos. Chem. Phys.*, *11*(1), 241–256.

Hodges, K., D. Chappell, G. Robinson, and G. Yang (2000), An improved algorithm for generating global window brightness temperatures from multiple satellite infrared imagery, *J. Atmos. Ocean. Technol.*, *17*(10), 1296–1312.

Hoffmann, L., C. M. Hoppe, R. Müller, G. S. Dutton, J. C. Gille, S. Griessbach, A. Jones, C. I. Meyer, R. Spang, C. M. Volk, and K. A. Walker (2014), Stratospheric lifetime ratio of cfc-11 and cfc-12 from satellite and model climatologies, *Atmos. Chem. Phys.*, *14*(22), 12,479–12,497, doi:10.5194/acp-14-12479-2014.

Holton, J. R. (1992), *An Introduction to Dynamic Meteorology*, Academic Press, London.

Holton, J. R., P. Haynes, M. E. McIntyre, A. R. Douglass, R. B. Rood, and L. Pfister (1995), Stratosphere-troposphere exchange, *Rev. Geophys.*, *33*, 403–439.

Homan, C. D., C. M. Volk, A. C. Kuhn, A. Werner, J. Baehr, S. Viciani, A. Ulanovski, and F. Ravegnani (2010), Tracer measurements in the tropical tropopause layer during the AMMA/SCOUT-O3 aircraft campaign, *Atmos. Chem. Phys.*, *10*(8), 3615–3627.

Hoor, P., H. Fischer, L. Lange, J. Lelieveld, and D. Brunner (2002), Seasonal variations of a mixing layer in the lowermost stratosphere as identified by the CO-O_3 correlation from in situ measurements, *J. Geophys. Res.*, *107*(D5), 4044, doi: 10.1029/2000JD000289.

Hoppe, C. M., L. Hoffmann, P. Konopka, J.-U. Grooß, F. Ploeger, G. Günther, P. Jöckel, and R. Müller (2014), The implementation of the CLaMS lagrangian transport core into the chemistry climate model EMAC 2.40.1: application on age of air and transport of long-lived trace species, *Geoscientific Model Development*, *7*(6), 2639–2651.

Houze, R. A., D. C. Wilton, and B. F. Smull (2007), Monsoon convection in the himalayan region as seen by the trmm precipitation radar, *Q. J. R. Meteorol. Soc.*, *133*(627), 1389–1411.

Hurst, D. F., S. J. Oltmans, H. Vömel, K. H. Rosenlof, S. M. Davis, E. A. Ray, E. G. Hall, and A. F. Jordan (2011), Stratospheric water vapor trends over boulder, colorado: Analysis of the 30 year boulder record, *J. Geophys. Res. A*, *116*(D2).

James, R., and B. Legras (2009), Mixing processes and exchanges in the tropical and the subtropical UT/LS, *Atmos. Chem. Phys.*, *9*, 25–38.

Jones, A., D. Thomson, M. Hort, and B. Devenish (2007), The uk met office's next-generation atmospheric dispersion model, name iii, in *Air Pollution Modeling and its Application XVII*, pp. 580–589, Springer.

Kerr-Munslow, A., and W. Norton (2006), Tropical wave driving of the annual cycle in tropical tropopause temperatures. part i: Ecmwf analyses, *J. Atmos. Sci.*, *63*(5), 1410–1419.

Kiladis, G., K. Straub, G. Reid, and K. Gage (2001), Aspects of interannual and intraseasonal variability of the tropopause and lower stratosphere, *Q. J. R. Meteorol. Soc.*, *127*(576), 1961–1983.

Konopka, P. (1995), Analytical Gaussian solutions for anisotropic diffusion in a linear shear flow, *J. Non Equil. Thermodyn.*, *20*, 78–91.

Konopka, P., H.-M. Steinhorst, J.-U. Grooß, G. Günther, R. Müller, J. W. Elkins, H.-J. Jost, E. Richard, U. Schmidt, G. Toon, and D. S. McKenna (2004), Mixing and ozone loss in the 1999-2000 Arctic vortex: Simulations with the 3-dimensional Chemical Lagrangian Model of the Stratosphere (CLaMS), *J. Geophys. Res.*, *109*, D02315, doi: 10.1029/2003JD003792.

Konopka, P., G. Günther, D. S. McKenna, R. Müller, D. Offermann, R. Spang, and M. Riese (2005), How homogeneous and isotropic is stratospheric mixing? Comparison of CRISTA-1 observations with transport studies based on the Chemical Lagrangian Model of the Stratosphere (CLaMS), *Q. J. R. Meteorol. Soc.*, *131*(606), 565–579, doi:10.1256/qj.04.47.

Konopka, P., G. Günther, R. Müller, F. H. S. dos Santos, C. Schiller, F. Ravegnani, A. Ulanovsky, H. Schlager, C. M. Volk, S. Viciani, L. L. Pan, D.-S. McKenna, and M. Riese (2007), Contribution of mixing to upward transport across the tropical tropopause layer (TTL), *Atmos. Chem. Phys.*, *7*(12), 3285–3308.

Konopka, P., J.-U. Grooß, G. Günther, F. Ploeger, R. Pommrich, R. Müller, and N. Livesey (2010), Annual cycle of ozone at and above the tropical tropopause: observations versus simulations with the Chemical Lagrangian Model of the Stratosphere (CLaMS), *Atmos. Chem. Phys.*, *10*(1), 121–132, doi:10.5194/acp-10-121-2010.

Konopka, P., F. Ploeger, and R. Müller (2012), Entropy-based and static stability–based lagrangian model grids, *Lagrangian Modeling of the Atmosphere*, *200*, 99–110, doi: 10.1029/95GL00814.

Konopka, P., F. Ploeger, M. Tao, T. Birner, and M. Riese (2015), Hemispheric asymmetries and seasonality of mean age of air in the lower stratosphere: Deep versus shallow branch of the brewer-dobson circulation, *J. Geophys. Res. A*, *120*(5), 2053–2066.

Kunz, A., P. Konopka, R. Müller, L. L. Pan, C. Schiller, and F. Rohrer (2009), High static stability in the mixing layer above the extratropical tropopause, *J. Geophys. Res.*, *114*, D16,305.

Kunz, A., R. Müller, V. Homonnai, I. M Jánosi, D. Hurst, A. Rap, P. M Forster, F. Rohrer, N. Spelten, and M. Riese (2013), Extending water vapor trend observations over boulder into the tropopause region: trend uncertainties and resulting radiative forcing, *J. Geophys. Res. A*, *118*(19), 11–269.

Kunz, A., N. Spelten, P. Konopka, R. Müller, R. Forbes, and H. Wernli (2014), Comparison of fast in situ stratospheric hygrometer (fish) measurements of water vapor in the upper troposphere and lower stratosphere (utls) with ecmwf (re) analysis data, *Atmos. Chem. Phys.*, *14*(19), 10,803–10,822.

Kuttippurath, J., and G. Nikulin (2012), A comparative study of the major sudden stratospheric warmings in the arctic winters 2003/2004–2009/2010, *Atmos. Chem. Phys.*, *12*(17), 8115–8129.

Labitzke, K. (1977), Interannual variability of the winter stratosphere in the northern hemisphere, *Monthly Weather Review*, *105*(6), 762–770.

Labitzke, K., and M. Kunze (2009), On the remarkable arctic winter in 2008/2009, *J. Geophys. Res. A*, *114*(D1), D00I02, doi:10.1029/2009JD012273.

Lahoz, W., Q. Errera, S. Viscardy, and G. Manney (2011), The 2009 stratospheric major warming described from synergistic use of BASCOE water vapour analyses and MLS observations, *Atmos. Chem. Phys.*, *11*(10), 4689–4703.

Legras, B., I. Pisso, G. Berthet, and F. Lefevre (2005), Variability of the Lagrangian turbulent diffusion in the lower stratosphere, *Atmos. Chem. Phys.*, *5*, 1605–1622.

Lemmen, C., R. Müller, P. Konopka, and M. Dameris (2006), Critique of the tracer-tracer correlation technique and its potential to analyse polar ozone loss in chemistry-climate models, *J. Geophys. Res.*, *111*(D18), D18307, doi:10.1029/2006JD007298.

Limpasuvan, V., D. W. Thompson, and D. L. Hartmann (2004), The life cycle of the northern hemisphere sudden stratospheric warmings, *Journal of Climate*, *17*(13), 2584–2596.

Lin, S.-J., and R. B. Rood (1996), Multidimensional flux-form semi-Lagrangian transport schemes, *Mon. Wea. Rev.*, *124*, 2046–2070.

Liu, C., B. Tian, K.-F. Li, G. L. Manney, N. J. Livesey, Y. L. Yung, and D. E. Waliser (2014), Northern hemisphere mid-winter vortex-displacement and vortex-split stratospheric sudden warmings: Influence of the madden-julian oscillation and quasi-biennial oscillation, *J. Geophys. Res. A*, *119*(22), 12–599.

Livesey, N. J., W. G. Read, L. Froidevaux, A. Lambert, G. L. Manney, H. C. Pumphrey, M. L. Santee, M. J. Schwartz, S. Wang, R. E. Cofield, D. T. Cuddy, R. A. Fuller, R. F. Jarnot, J. H. Jiang, B. W. Knosp, P. C. Stek, P. A. Wagner, and D. L. Wu (2013), Version 3.3 and 3.4 level 2 data quality and description document, *JPL D-33509*.

Lorenz, E. N. (1963), Deterministic non-periodic flow, *J. Atmos. Sci.*, *20*, 130–141.

Lyubarski, G. Y. (1960), *The Application of Group Theory in Physics*, Pergamon Press, Oxford.

Madden, R. A., and P. R. Julian (1972), Description of global-scale circulation cells in the tropics with a 40-50 day period, *J. Atmos. Sci.*, *29*(6), 1109–1123.

Mahowald, N. M., R. A. Plumb, P. J. Rasch, J. del Corral, and F. Sassi (2002), Stratospheric transport in a three-dimensional isentropic coordinate model, *J. Geophys. Res.*, *107*(D15), 4254, doi:10.1029/2001JD001313.

Manney, G. L., K. Krüger, J. L. Sabutis, S. Amina Sena, and S. Pawson (2005), The remarkable 2003-2004 winter and other recent warm winters in the Arctic stratosphere in the late 1990s, *J. Geophys. Res.*, *110*, D04107, doi:10.1029/2004JD005367.

Manney, G. L., K. Krüger, S. Pawson, K. Minschwaner, M. J. Schwartz, W. H. Daffer, N. J. Livesey, M. G. Mlynczak, E. E. Remsberg, J. M. Russell, and J. W. Water (2008), The evolution of the stratopause during the 2006 major warming: Satellite data and assimilated meteorological analyses, *J. Geophys. Res. A*, *113*(D11115), doi:10.1029/2007JD009097.

Manney, G. L., R. S. Harwood, I. A. MacKenzie, K. Minschwaner, D. R. Allen, M. L. Santee, K. A. Walker, M. I. Hegglin, A. Lambert, H. C. Pumphrey, P. F. Bernath, C. D. Boone, M. J. Schwartz, N. J. Livesey, W. H. Daffer, and R. A. Fuller (2009a), Satellite observations and modeling of transport in the upper troposphere through the lower mesosphere during the 2006 major stratospheric sudden warming, *Atmos. Chem. Phys.*, *9*, 4775–4795, doi:10.5194/acp-9-4775-2009.

Manney, G. L., M. J. Schwartz, K. Krüger, M. L. Santee, S. Pawson, J. N. Lee, W. H. Daffer, R. A. Fuller, and N. J. Livesey (2009b), Aura microwave limb sounder observations of dynamics and transport during the record-breaking 2009 arctic stratospheric major warming, *Geophys. Res. Lett.*, *36*(12), L12,815, doi:10.1029/2009GL038586.

Manney, G. L., Z. Lawrence, M. Santee, N. Livesey, A. Lambert, and M. Pitts (2015), Polar processing in a split vortex: Arctic ozone loss in early winter 2012/2013, *Atmos. Chem. Phys.*, *15*(10), 5381–5403.

Matsuno, T. (1971), A dynamical model of the stratospheric sudden warming, *J. Atmos. Sci.*, *28*(8), 1479–1494.

McIntyre, M. E., and T. N. Palmer (1983), Breaking planetary waves in the stratosphere, *Nature*, *305*, 593–600.

McKenna, D. S., P. Konopka, J.-U. Grooß, G. Günther, R. Müller, R. Spang, D. Offermann, and Y. Orsolini (2002a), A new Chemical Lagrangian Model of the Stratosphere (CLaMS): 1. Formulation of advection and mixing, *J. Geophys. Res.*, *107*(D16), 4309, doi:10.1029/2000JD000114.

McKenna, D. S., J.-U. Grooß, G. Günther, P. Konopka, R. Müller, G. Carver, and Y. Sasano (2002b), A new Chemical Lagrangian Model of the Stratosphere (CLaMS): 2. Formulation of chemistry scheme and initialization, *J. Geophys. Res.*, *107*(D15), 4256, doi:10.1029/2000JD000113.

Meneguz, E., and D. J. Thomson (2014), Towards a new scheme for parametrisation of deep convection in name iii, *International Journal of Environment and Pollution 15*, *54*(2-4), 128–136.

Michelsen, H. A., G. L. Manney, M. R. Gunson, and R. Zander (1998), Correlations of stratospheric abundances of NO_y, O_3, N_2O, and CH_4 derived from ATMOS measurements, *J. Geophys. Res.*, *103*, 28,347–28,359.

Mlynczak, M. G., C. J. Mertens, R. R. Garcia, and R. W. Portmann (1999), A detailed evaluation of the stratospheric heat budget: 2. global radiation balance and diabatic circulations, *J. Geophys. Res.*, *104*(D6), 6039–6066.

Moncrieff, M., and M. Miller (1976), The dynamics and simulation of tropical cumulonimbus and squall lines, *Q. J. R. Meteorol. Soc.*, *102*(432), 373–394.

Mote, P. W., K. H. Rosenlof, M. E. McIntyre, E. S. Carr, J. G. Gille, J. R. Holton, J. S. Kinnersley, H. C. Pumphrey, J. M. Russell III, and J. W. Waters (1996), An atmospheric tape recorder: The imprint of tropical tropopause temperatures on stratospheric water vapor, *J. Geophys. Res.*, *101*, 3989 – 4006.

Mote, P. W., T. J. Dunkerton, M. E. McIntyre, E. A. Ray, P. H. Haynes, and J. M. Russell III (1998), Vertical velocity, vertical diffusion, and dilution by midlatitude air in the tropical lower stratosphere, *J. Geophys. Res.*, *103*, 8651 – 8666.

Müller, R., P. J. Crutzen, J.-U. Grooß, C. Brühl, J. M. Russell III, and A. F. Tuck (1996), Chlorine activation and ozone depletion in the Arctic vortex: Observations by the Halogen Occultation Experiment on the Upper Atmosphere Research Satellite, *J. Geophys. Res.*, *101*, 12,531–12,554.

Müller, R., U. Schmidt, A. Engel, D. S. McKenna, and M. H. Proffitt (2001), The O_3–N_2O relationship from balloon-borne observations as a measure of Arctic ozone loss in 1991/92, *Q. J. R. Meteorol. Soc.*, *127*, 1389–1412.

Müller, R., S. Tilmes, P. Konopka, J.-U. Grooß, and H.-J. Jost (2005), Impact of mixing and chemical change on ozone-tracer relations in the polar vortex, *Atmos. Chem. Phys.*, *5*, 3139–3151.

Nash, E. R., P. A. Newman, J. E. Rosenfield, and M. R. Schoeberl (1996), An objective determination of the polar vortex using Ertel's potential vorticity, *J. Geophys. Res.*, *101*, 9471–9478.

Newman, M., P. D. Sardeshmukh, and J. W. Bergman (2000), An assessment of the ncep, nasa, and ecmwf reanalyses over the tropical west pacific warm pool, *Bull. Am. Meteorol. Soc.*, *81*(1), 41.

Newman, P. A., E. R. Nash, and J. E. Rosenfield (2001), What controls the temperature of the Arctic stratosphere during the spring?, *J. Geophys. Res.*, *106*(D17), 19,999–20,010, doi:10.1029/2000JD000061.

Norton, W. (2006), Tropical wave driving of the annual cycle in tropical tropopause temperatures. part ii: Model results, *J. Atmos. Sci.*, *63*(5), 1420–1431.

Oltmans, S. J., H. Vömel, D. J. Hofmann, K. H. Rosenlof, and D. Kley (2000a), The increase in stratospheric water vapor from balloonborne, frostpoint hygrometer measurements at washington, dc, and boulder, colorado, *Geophys. Res. Lett.*, *27*(21), 3453–3456.

Oltmans, S. J., H. Vömel, D. J. Hofmann, K. H. Rosenlof, and D. Kley (2000b), Tropical convective outflow and near surface equivalent potential temperatures, *Geophys. Res. Lett.*, *27*(21), doi:10.1029/2000GL012133.

Onsager, L. (1931), Reciprocal Relations in Irreversible Processes. I, *Phys. Rev.*, *37*, 405–426.

Orsolini, Y. J., J. Urban, D. P. Murtagh, S. Lossow, and V. Limpasuvan (2010), Descent from the polar mesosphere and anomalously high stratopause observed in 8 years of water vapor and temperature satellite observations by the odin sub-millimeter radiometer, *J. Geophys. Res.*, *115*(D12), doi:10.1029/2009JD013501.

Pan, L. L., W. J. Randel, B. L. Gary, M. J. Mahoney, and E. J. Hintsa (2004), Definitions and sharpness of the extratropical tropopause: A trace gas perspective, *J. Geophys. Res.*, *109*(D23103), doi:10.1029/2004JD004982.

Pan, L. L., P. Konopka, and E. V. Browell (2006), Observations and model simulations of mixing near the extratropical tropopause, *J. Geophys. Res.*, *111*(D05106), doi: 10.1029/2005JD006480.

Pan, L. L., K. P. Bowman, M. Shapiro, W. J. Randel, R. S. Gao, T. Campos, C. Davis, S. Schauffler, B. A. Ridley, J. C. Wei, and C. Barnet (2007), Chemical behaviour of the tropopause observed during the (s)tratosphere-(t)roposphere (a)nalyses of (r)egion (t)ransport experiment, *J. Geophys. Res.*, *112*(D18110), doi:10.1029/2007JD008645.

Pan, L. L., K. P. Bowman, E. L. Atlas, S. C. Wofsy, F.Zhang, J. F. Bresch, B. A. Ridley, J. V. Pittman, C. R. Homeyer, P. Romashkin, and W. A. Cooper (2010), The Stratosphere-Troposphere Analyses of Regional Transport 2008 (START08) Experiment, *Bull. Am. Meteorol. Soc.*, *91*, 327–342.

Petzold, A., V. Thouret, C. Gerbig, A. Zahn, C. Brenninkmeijer, M. Gallagher, M. Hermann, M. Pontaud, H. Ziereis, D. Boulanger, J. Marshall, P. Nédélec, H. Smit, U. Friess, J.-M. Flaud, A. Wahner, J.-P. Cammas, and A. Volz-Thomas (2015), Global-scale atmosphere monitoring by in-service aircraft - current achievements and future prospects of the european research infrastructure iagos, *Tellus B*, *67*(0).

Pickering, K., R. Dickerson, G. Huffman, J. Boatman, and A. Schanot (1988), Trace gas transport in the vicinity of frontal convective clouds, *J. Geophys. Res. A*, *93*(D1), 759–773.

Pisso, I., and B. Legras (2008), Turbulent vertical diffusivity in the sub-tropical stratosphere, *Atmos. Chem. Phys.*, *8*, 697–707.

Ploeger, F., P. Konopka, G. Günther, J.-U-Grooß, and R. Müller (2010), Impact of the vertical velocity scheme on modeling transport across the tropical tropopause layer, *J. Geophys. Res.*, *115*(D03301), doi:10.1029/2009JD012023.

Ploeger, F., G. Günther, P. Konopka, S. Fueglistaler, R. Müller, C. Hoppe, A. Kunz, R. Spang, J.-U. Grooß, and M. Riese (2013), Horizontal water vapor transport in the lower stratosphere from subtropics to high latitudes during boreal summer, *J. Geophys. Res.*, *118*, 8111–8127, doi:10.1002/jgrd.50636.

Plumb, R. A. (1996), A “tropical pipe” model of stratospheric transport, *J. Geophys. Res.*, *101*, 3957–3972.

Plumb, R. A. (2007), Tracer interrelationships in the stratosphere, *Rev. Geophys.*, *45*, RG4005, doi:10.1029/2005RG000179.

Plumb, R. A., and R. C. Bell (1982), A model of the quasi-biennial oscillation on an equatorial beta-plane, *Q. J. R. Meteorol. Soc.*, *108*(456), 335–352.

Plumb, R. A., D. W. Waugh, and M. P. Chipperfield (2000), The effect of mixing on tracer relationships in the polar vortices, *J. Geophys. Res.*, *105*, 10,047–10,062.

Polvani, L. M., D. Waugh, and R. A. Plumb (1995), On the subtropical edge of the stratospheric surf zone, *J. Atmos. Sci.*, *52*(9), 1288–1309.

Pommrich, R., R. Müller, J.-U. Grooß, P. Konopka, F. Ploeger, B. Vogel, M. Tao, C. Hoppe, G. Günther, N. Spelten, et al. (2014), Tropical troposphere to stratosphere transport of carbon monoxide and long-lived trace species in the chemical lagrangian model of the stratosphere (clams), *Geoscientific Model Development*, *7*(6), 2895–2916.

Proffitt, M. H., and R. J. McLaughlin (1983), Fast-response dual-beam UV absorption ozone photometer suitable for use on stratospheric balloons, *Radio Sci.*, *54*, 1719–1728.

Proffitt, M. H., J. J. Margitan, K. K. Kelly, M. Loewenstein, J. R. Podolske, and K. R. Chan (1990), Ozone loss in the Arctic polar vortex inferred from high altitude aircraft measurements, *Nature*, *347*, 31–36.

Punge, H. J., P. Konopka, M. A. Giorgetta, and R. Müller (2009), Effects of the quasi-biennial oscillation on low-latitude transport in the stratosphere derived from trajectory calculations, *J. Geophys. Res.*, *114*, D03102, doi:10.1029/2008JD010518.

Quiroz, R. (1975), The stratospheric evolution of sudden warmings in 1969-74 determined from measured infrared radiation fields, *J. Atmos. Sci.*, *32*(1), 211–224.

Randall, C., V. L. Harvey, D. Siskind, J. France, P. Bernath, C. Boone, and K. Walker (2009), Nox descent in the arctic middle atmosphere in early 2009, *Geophys. Res. Lett.*, *36*(L18811), doi:10.1029/2009GL039706.

Randel, W., P. Udelhofen, E. Fleming, M. Geller, M. Gelman, K. Hamilton, D. Karoly, D. Ortland, S. Pawson, R. Swinbank, F. Wu, M. Baldwin, M.-L. Chanin, P. Keckhut, K. Labitzke, E. Remsberg, A. Simmons, and D. Wu (2004a), The SPARC intercomparison of middle-atmosphere climatologies, *J. Climate*, *17*, 986–1003.

Randel, W. J., and F. Wu (2005), Kelvin wave variability near the equatorial tropopause observed in gps radio occultation measurements, *J. Geophys. Res. A*, *110*(D3).

Randel, W. J., R. R. Garcia, and F. Wu (2002), Time-dependent upwelling in the tropical lower stratosphere estimated from the zonal-mean momentum budget, *J. Atmos. Sci.*, *59*, 2141–2152.

Randel, W. J., F. Wu, S. J. Oltmans, K. Rosenlof, and G. E. Nodoluha (2004b), Interannual changes of stratospheric water vapor and correlations with tropical tropopause temperatures, *J. Atmos. Sci.*, *61*, 2133–2148.

Randel, W. J., F. Wu, H. Vömel, G. E. Nedoluha, and P. Forster (2006), Decreases in stratospheric water vapor after 2001: Links to changes in the tropical tropopause and the Brewer-Dobson circulation, *J. Geophys. Res.*, *111*, D12312, doi: 10.1029/2005JD006744.

Randel, W. J., R. R. Garcia, N. Calvo, and D. Marsh (2009), Enso influence on zonal mean temperature and ozone in the tropical lower stratosphere, *Geophys. Res. Lett.*, *36*(15).

Ray, E. A., F. L. Moore, J. W. Elkins, D. F. Hurst, P. A. Romashkin, G. S. Dutton, and D. W. Fahey (2002), Descent and mixing in the 1999-2000 northern polar vortex inferred from in situ tracer measurements, *J. Geophys. Res.*, *107*, 8285, doi:10.1029/2001JD000961.

Read, W. G., A. Lambert, J. Bacmeister, R. E. Cofield, L. E. Christensen, D. T. Cuddy, W. H. Daffer, B. J. Drouin, E. Fetzer, L. Froidevaux, R. Fuller, R. Herman, R. F. Jarnot, J. H. Jiang, Y. Jiang, K. Kelly, B. W. Knosp, L. J.Kovalenko, N. J. Livesey, H.-C. Liu, G. L. Manney, H. M. Pickett, H. C. Pumphrey, K. H. Rosenlof, X. Sabounchi, M. L. Santee, M. J. Schwartz, W. V. Snyder, P. Stek, H. Su, L. L. Takacs, R. P. Thurstans, H. Voemel, P. A. Wagner, J. W. Waters, C. R. Webster, E. M. Weinstock, and D. L. Wu (2007), Aura Microwave Limb Sounder upper tropospheric and lower stratospheric H_2O and relative humidity with respect to ice validation, *J. Geophys. Res.*, *112*(D24S35), doi:10.1029/2007JD008752.

Richard, E. C., K. C. Aikin, A. E. Andrews, B. C. Daube, C. Gerbig, S. C. Wofsy, P. A. Romashkin, D. F. Hurst, E. A. Ray, F. L. Moore, J. W. Elkins, T. Deshler, and G. C. Toon (2001), Severe chemical ozone loss in the Arctic polar vortex during winter 1999-2000 inferred from in-situ airborne measurements, *Geophys. Res. Lett.*, *28*(11), 2197–2000.

Riese, M., J.-U. Grooß, T. Feck, and S. Rohs (2006), Long-term changes of hydrogen-containing species in the stratosphere, *J. Atmos. Solar Terr. Phys.*, *68*(17), 1973–1979.

Riese, M., F. Ploeger, A. Rap, B. Vogel, P. Konopka, M. Dameris, and P. M. Forster (2012), Impact of uncertainties in atmospheric mixing on simulated UTLS composition and related radiative effects, *J. Geophys. Res.*, *117*, D16, doi:doi:10.1029/2012JD017751.

Rind, D., and P. Lonergan (1995), Modeled impacts of stratospheric ozone and water-vapor perturbations with implications for high-speed civil transport aircraft, *J. Geophys. Res.*, *100*(D4), 7381–7396.

Röckmann, T., J.-U. Grooß, and R. Müller (2004), The impact of anthropogenic chlorine emissions, stratospheric ozone change and chemical feedbacks on stratospheric water, *Atmos. Chem. Phys.*, *4*, 693–699.

Rohs, S., C. Schiller, M. Riese, A. Engel, U. Schmidt, T. Wetter, I. Levin, T. Nakazawa, and S. Aoki (2006), Long-term changes of methane and hydrogen in the stratosphere in the period 1978–2003 and their impact on the abundance of stratospheric water vapor, *J. Geophys. Res. A*, *111*(D14).

Rosenlof, K., S. Oltmans, D. Kley, J. Russell, E.-W. Chiou, W. Chu, D. Johnson, K. Kelly, H. Michelsen, G. Nedoluha, et al. (2001), Stratospheric water vapor increases over the past half-century, *grl*, *28*(7), 1195–1198.

Rosenlof, K. H. (1995), Seasonal cycle of the residual mean meridional circulation in the stratosphere, *J. Geophys. Res.*, *100*, 5173 – 5191.

Rosenlof, K. H., and G. C. Reid (2008), Trends in the temperature and water vapor content of the tropical lower stratosphere: Sea surface connection, *J. Geophys. Res.*, *113*(D6).

Ross, D. E., J. A. Pyle, N. R. P. Harris, J. D. McIntyre, G. A. Millard, A. D. Robinson, and R. Busen (2004), Investigation of Arctic ozone depletion sampled over midlatitudes during the Egrett campaign of spring/summer 2000, *Atmos. Chem. Phys.*, *4*, 1407–1417.

Rybka, H., and H. Tost (2014), Uncertainties in future climate predictions due to convection parameterisations, *Atmos. Chem. Phys.*, *14*(11), 5561–5576.

Sankey, D., and T. G. Shepherd (2003), Correlations of long-lived chemical species in a middle atmosphere general circulation model, *J. Geophys. Res.*, *108*(D16), 4494, doi:10.1029/2002JD002799.

Scherhag, R. (1952), Die explosionsartigen stratosphärenerwärmungen des spätwinters 1951/52, *Berichte des deutschen Wetterdienstes in der US-Zone*, *6*(38), 51–63.

Schoeberl, M. R. (1978), Stratospheric warmings- observations and theory, *Reviews of Geophysics and Space Physics*, *16*(4), 521–538.

Searle, K. R., M. P. Chipperfield, S. Bekki, and J. A. Pyle (1998a), The impact of spatial averaging on calculated polar ozone loss: I. Model experiments, *J. Geophys. Res.*, *103*, 25,397–25,408.

Searle, K. R., M. P. Chipperfield, S. Bekki, and J. A. Pyle (1998b), The impact of spatial averaging on calculated polar ozone loss: II. Theoretical analysis, *J. Geophys. Res.*, *103*, 25,409–25,416.

Shuckburgh, E., W. Norton, A. Iwi, and P. Haynes (2001), Influence of the quasi-biennial oscillation on isentropic transport and mixing in the tropics and subtropics, *J. Geophys. Res.*, *106*(D13), 14,327–14,337.

Solomon, S. (1999), Stratospheric ozone depletion: A review of concepts and history, *Rev. Geophys.*, *37*(3), 275–316, doi:10.1029/1999RG900008.

Solomon, S., K. Rosenlof, R. Portmann, J. Daniel, S. Davis, T. Sanford, and G.-K. Plattner (2010), Contributions of stratospheric water vapor to decadal changes in the rate of global warming, *Science*, *327*, 1219–1222, doi:10.1126/science.1182488.

Stenke, A., and V. Grewe (2005), Simulation of stratospheric water vapor trends: impact on stratospheric ozone chemistry, *Atmos. Chem. Phys.*, *5*, 1257–1272.

Stohl, A., C. Forster, A. Frank, P. Seibert, and G. Wotawa (2005), Technical note: The Lagrangian particle dispersion model FLEXPART version 6.2, *Atmos. Chem. Phys.*, *5*, 2461–2474.

Stull, R. B. (1988), *An introduction to boundary layer meteorology*, vol. 13, Springer Science & Business Media.

Taguchi, M. (2011), Latitudinal extension of cooling and upwelling signals associated with stratospheric sudden warmings, *J. Meteorol. Soc. Jpn.*, *89*(5), 571–580.

Tan, D. G. H., P. H. Haynes, A. R. MacKenzie, and J. A. Pyle (1998), Effects of fluid-dynamical stirring and mixing on the deactivation of stratospheric chlorine, *J. Geophys. Res.*, *103*, 1585–1605.

Tao, M., P. Konopka, F. Ploeger, J.-U. Grooß, R. Müller, C. M. Volk, K. A. Walker, and M. Riese (2015a), Impact of the 2009 major sudden stratospheric warming on the composition of the stratosphere, *Atmos. Chem. Phys.*, *15*(15), 8695–8715, doi: 10.5194/acp-15-8695-2015.

Tao, M., P. Konopka, F. Ploeger, M. Riese, R. Müller, and C. M. Volk (2015b), Impact of stratospheric major warmings and the quasi-biennial oscillation on the variability of stratospheric water vapor, *Geophys. Res. Lett.*, *42*(11), 4599–4607, doi:10.1002/2015GL064443, 2015GL064443.

Tilmes, S. (2004), Chemical ozone loss in the Arctic polar stratosphere, *Tech. rep.*, Institute of Chemistry and Dynamics of the Geosphere, Forschungszentrum Jülich, Germany.

Tilmes, S., R. Müller, A. Engel, M. Rex, and J. Russell III (2006), Chemical ozone loss in the Arctic and Antarctic stratosphere between 1992 and 2005, *Geophys. Res. Lett.*, *33*, L20812, doi:10.1029/2006GL026925.

Turner, J. S. (1973), *Buoyancy Effects in Fluids*, Cambridge University Press.

Urban, J., S. Lossow, G. Stiller, and W. Read (2014), Another drop in water vapor, *Eos, Transactions American Geophysical Union*, *95*(27), 245–246.

Vallis, G. K. (2006), *Atmospheric and oceanic fluid dynamics: fundamentals and large-scale circulation*, Cambridge University Press.

Vaughan, G., K. Bower, C. Schiller, A. MacKenzie, T. Peter, H. Schlager, N. Harris, and P. May (2008), Scout-o3/active: High-altitude aircraft measurements around deep tropical convection, *Bull. Am. Meteorol. Soc.*, *89*(5), 647–662.

Viciani, S., F. D'Amato, P. Mazzinghi, F. Castagnoli, G. Toci, and P. Werle (2008), A cryogenically operated laser diode spectrometer for airborne measurement of stratospheric trace gases, *Appl. Phys. B*, *90*, 581–592, doi:10.1007/s00340-007-2885-2.

Virts, K. S., and J. M. Wallace (2014), Observations of temperature, wind, cirrus, and trace gases in the tropical tropopause transition layer during the mjo, *J. Atmos. Sci.*, *71*(3), 1143–1157.

Vogel, B., R. Müller, T. Deshler, J.-U. Grooß, J. Karhu, D. S. McKenna, M. Müller, D. Toohey, G. C. Toon, and F. Stroh (2003), Vertical profiles of activated ClO and ozone loss in the Arctic vortex in January and March 2000: In situ observations and model simulations, *J. Geophys. Res.*, *108*(D22), 8334, doi:10.1029/2002JD002564.

Vogel, B., L. L. Pan, P. Konopka, G. Günther, R. Müller, T. Campos, W. Hall, I. Pollack, A. Weinheimer, J. Wei, E. L. Atlas, and K. P. Bowman (2011), Transport pathways and signatures of mixing in the extratropical tropopause region derived from Lagrangian model simulations, *J. Geophys. Res.*, *116*, doi:10.1029/2010JD014876.

Volk, C., O. Riediger, M. Strunk, U. Schmidt, F. Ravegnani, A. Ulanovsky, and V. Rudakov (2000), In situ tracer measurements in the tropical tropopause region during ape-theseo, eur, *Comm. Air Pollut. Res. Report*, *73*, 661–664.

Volk, C. M., J. W. Elkins, D. W. Fahey, R. J. Salawitch, G. S. Dutton, J. M. Gilligan, M. H. Proffitt, M. Loewenstein, J. R. Podolske, K. Minschwaner, J. J. Margitan, and K. R. Chan (1996), Quantifying transport between the tropical and mid-latitude lower stratosphere, *Science*, *272*, 1763–1768.

Volk, C. M., J. W. Elkins, D. W. Fahey, G. S. Dutton, J. M. Gilligan, M. Loewenstein, J. R. Podolske, and K. R. Chan (1997), On the evaluation of source gas lifetimes from stratospheric observations, *J. Geophys. Res.*, *102*, 25,543–25,564.

Wallace, J. M., and P. V. Hobbs (1977), *Atmospheric Science, An Introductory Survey*, Academic Press. Inc., San Diego.

Waugh, D. W., R. A. Plumb, J. W. Elkins, D. W. Fahey, K. A. Boering, G. S. Dutton, C. M. Volk, E. Keim, R.-S. Gao, B. C. Daube, S. C. Wofsy, M. Loewenstein, J. R. Podolske, K. R. Chan, M. H. Proffitt, K. K. Kelly, P. A. Newman, and L. R. Lait (1997), Mixing of polar vortex air into middle latitudes as revealed by tracer-tracer scatterplots, *J. Geophys. Res.*, *102*, 13,119–13,134.

Wheeler, M. C., and H. H. Hendon (2004), An all-season real-time multivariate mjo index: Development of an index for monitoring and prediction, *Monthly Weather Review*, *132*(8), 1917–1932.

WMO (2014), *Scientific Assessment of Ozone Depletion: 2014*, Global Ozone Research and Monitoring Project–Report No. 56, Geneva, Switzerland.

Wohltmann, I., and M. Rex (2009), The Lagrangian chemistry and transport model ATLAS: validation of transport and mixing, *Geosci. Model Dev.*, *2*, 153–173.

Woodman, R. F., and P. K. Rastogi (1984), Evaluation of effective eddy diffusivity coefficients using radar observations of turbulence in the stratosphere, *Geophys. Res. Lett.*, *211*, 243–246.

Wright, J., and S. Fueglistaler (2013), Large differences in reanalyses of diabatic heating in the tropical upper troposphere and lower stratosphere, *Atmos. Chem. Phys.*, *13*(18), 9565–9576.

Yushkov, V., A. Oulanovsky, N. Lechenuk, I. Roudakov, K. Arshinov, F. Tikhonov, L. Stefanutti, F. Ravegnani, U. Bonafï¿½ï¿½, and T. Georgiadis (1982), A Chemiluminescent Analyzer for Stratospheric Measurements of the Ozone Concentration (FOZAN), *Journal Atmospheric Oceanic Technology*, *16*, 1345 – 1350.

Zahn, A., E. Christner, P. Velthoven, A. Rauthe-Schöch, and C. Brenninkmeijer (2014), Processes controlling water vapor in the upper troposphere/lowermost stratosphere: An analysis of 8 years of monthly measurements by the iagos-caribic observatory, *J. Geophys. Res. A*, *119*(19).

Acknowledgements

Firstly, I would like to address my sincere gratitude to Prof. Dr. C. Michael Volk for trusting me with this interesting topic and for his excellent scientific advice. His example of rigorous cessation of scientific work deeply influenced me. I am also very grateful to Prof. Dr. Martin Riese for offering me the opportunity to work at IEK-7 and to PD. Dr. Rolf Müller for continuously supporting my research and his helpful comments on my work and publications during the last three and a half years.

Furthermore, I would like to convey my special thanks to Dr. Paul Konopka. To me, he is not only my scientific advisor, who taught me the details of CLaMS, patiently discussed with me about our research, and inspired me with creative ideas. He also became an important friend, introduced me to German culture and gave me generous help. This means a lot to me and facilitated my stay as a foreigner.

I am also very grateful to Prof. Dr. Yi Liu who introduced me to the PhD project in Forschungszentrum Jülich and supported me to apply the position in IEK-7. During my study in Germany, he gave me many great ideas and suggestions as my external mentor.

Also, my thanks go to the colleagues at IEK-7, especially to my colleagues in the theory group: Felix Plöger, Nicole Thomas, Bärbel Vogel, Jens-Uwe Grooß, Gebhard Günther, Reinhold Spang, and Verena Alishahi. All of them contributed to a very pleasurable working environment. Their support made this work possible. I would like to emphasize my thanks to Dr. Felix Plöger. His fresh ideas, programming experiences, and practical comments helped me through some of the difficulties of this work.

I also would like to address my thanks to the Post-Docs and students I met during the last three and a half years. I would like to warmly mention Charlotte Hoppe, Silvio Kalisch, Ines Engel, Anja Costa, Thai Trinh, Yajun Zhu, Shicheng Yu, Qianli Ma, Zhujun Yu and Yanli Zhang. It is a great pleasure to know you and share our scientific and non-scientific experiences during the course of our study.

Last, but not least, I would like to give my sincere gratitude to my beloved parents in China. I am very thankful for their support with the decisions I made and their continuous effort in understanding my scientific work.

Band / Volume 308
Emissions of Biogenic Volatile Organic Compounds and Ozone Balance under Future Climate Conditions
C. Wu (2016), VI, 105 pp
ISBN: 978-3-95806-121-7

Band / Volume 309
Computerunterstützte Auslegung eines Brennstoffzellen-Batterie-Hybridsystems für die Bordstromversorgung
C. Krupp (2016), iii, 207 pp
ISBN: 978-3-95806-124-8

Band / Volume 310
Influence of H_2O, HCl and H_2S on the Release and Condensation of Trace Metals in Gasification
M. Benito Abascal (2016), XIX, 172 pp
ISBN: 978-3-95806-125-5

Band / Volume 311
Mechanical and Thermochemical Properties of Nano-structured Membranes for Gas Separation in Fossil-fired Power Plants
J. Zhang (2016), II, 134 pp
ISBN: 978-3-95806-126-2

Band / Volume 312
Development of Embedded Thermocouple Sensors for Thermal Barrier Coatings (TBCs) by a Laser Cladding Process
Y. Zhang (2016), II, 108 pp
ISBN: 978-3-95806-129-3

Band / Volume 313
Streamwater transit time distributions at the catchment scale: constraining uncertainties through identification of spatio-temporal controls
M. Stockinger (2016), XIX, 161 pp
ISBN: 978-3-95806-131-6

Band / Volume 314
Entwicklung eines metallbasierten Substratkonzepts für energieeffiziente Gastrennmembranen
J. A. Kot (2016), xi, 201 pp
ISBN: 978-3-95806-134-7

Band / Volume 315
Langzeitbeobachtung der Dosisbelastung der Bevölkerung in radioaktiv kontaminierten Gebieten Weißrusslands – Korma-Studie II (1998 – 2015)
P. Zoriy, H. Dederichs, J. Pillath, B. Heuel-Fabianek, P. Hill, R. Lennartz (2016), ca 104 pp
ISBN: 978-3-95806-137-8

Band / Volume 316
Oxidation Mechanisms of Metallic Carrier Materials for Gas Separation Membranes
M. Schiek (2016), 148 pp
ISBN: 978-3-95806-138-5

Band / Volume 317
Thermoschockverhalten und temperaturabhängige Eigenschaften kohlenstoffarmer und -freier Feuerfestwerkstoffe
A. Böhm (2016), VI, 153 pp
ISBN: 978-3-95806-139-2

Band / Volume 318
Theoretical and experimental studies of runaway electrons in the TEXTOR tokamak
S.S. Abdullaev, K.H. Finken, K. Wongrach, O. Willi (2016), X, 109 pp
ISBN: 978-3-95806-140-8

Band / Volume 319
Modelling Thermodynamic Properties of Intercalation Compounds for Lithium Ion Batteries
S. O. Dang (2016), x, 133 pp
ISBN: 978-3-95806-141-5

Band / Volume 320
Atmospheric Mixing in a Lagrangian Framework
M. Tao (2016), 146 pp
ISBN: 978-3-95806-142-2